**UNIVERSITY OF SOUTHAMPTON**

FACULTY OF SCIENCE, ENGINEERING AND MATHEMATICS

School of Chemistry

# Synthesis of nanocrystalline nitride materials

by

**Pietro Chirico**

Thesis for the degree of Doctor of Philosophy

April 2011

# ABSTRACT

The work described in this thesis is largely concerned with the preparation of nanocrystalline nitrides materials under solvothermal conditions. Colloidal GaN nanocrystals were also grown in solution through decomposition of molecular precursors.

GaN and InN were investigated under solvothermal conditions from the reactions of $GaCl_3$, $InCl_3$ or $InI_3$ with lithium amide in benzene at various reaction temperatures. A mixture of wurtzite (hexagonal) and zinc blende (cubic)-type GaN was formed at temperatures between 450 and 300 ºC, whereas at 250 ºC GaN resembled the zinc blende type structure. The addition of surfactants such as (hexadecylamine or N-cetyltrimethylammonium bromide) was explored with the aim of preventing aggregation of the particles and controlling their size. Wurtzite type InN was also prepared in the same way, but the material contained In metal even at low temperature.

Group 5 and 6 nitrides were prepared from the reactions of transition metal chlorides ($VCl_3$, $NbCl_5$, $TaCl_5$, $CrCl_3$, $MoCl_5$ and $WCl_4$) with lithium amide or ammonia as nitrogen sources. Most of the nitrides obtained (VN, NbN, CrN, $Mo_2N$ and WN) adopted rocksalt-type structures. The only exception was $Ta_3N_5$ which crystallized in an orthorhombic structure. Carbon content was found in the nitrides due to benzene decomposition and usually it was higher when ammonia was used than with $LiNH_2$. Aggregation of the crystallites was found in most samples, though elongated particles (nanorods) were formed in $Ta_3N_5$ and $Mo_2N$ prepared using $NH_3$ and $LiNH_2$ respectively. Molybdenum nitride nanotubes were also formed from the reaction of $MoCl_5$ with $NH_3$ at 550 ºC. This was surprising since this morphology is not common in transition metal nitrides.

Colloidal preparation of nanocrystalline GaN was carried out from pyrolysis reactions of $[Ga(NMe_2)_3]_2$ employing stabilizing agents such as trioctylamine, hexadecylamine-trioctylamine mixture or trioctylphosphine. This method was used to investigate if it was possible reduce the aggregation of nanoparticles (compared with the solvothermal route) and take better control of their size during the synthesis.
Pyrolysis of $[Ga(NMe_2)_3]_2$ at 330 ºC in HDA-TOA yielded zinc blende (cubic) type-GaN at 330 ºC. A mixture of wurtzite and zinc-blende GaN was formed in the samples prepared in TOA under the same reaction conditions.

.

# Contents. Page

# List of figures.

# List of tables Page

# DECLARATION OF AUTHORSHIP

I, Pietro Chirico

declare that the thesis entitled

Synthesis of nanocrystalline nitride materials

and the work presented in the thesis are both my own, and have been generated by me as the result of my own original research. I confirm that:

- this work was done wholly or mainly while in candidature for a research degree at this University;
- where any part of this thesis has previously been submitted for a degree or any other qualification at this University or any other institution, this has been clearly stated;
- where I have consulted the published work of others, this is always clearly attributed;
- where I have quoted from the work of others, the source is always given. With the exception of such quotations, this thesis is entirely my own work;
- I have acknowledged all main sources of help;
- where the thesis is based on work done by myself jointly with others, I have made clear exactly what was done by others and what I have contributed myself;
- none of this work has been published before submission, or [delete as appropriate] parts of this work have been published as: [please list references]

Signed: ……..

Date:……

# Acknowledgements

First of all, I wish to express my sincere gratitude to my supervisor, Dr. Andrew L. Hector, for his continued encouragement and invaluable suggestions during this work. Also thanks to the other members of the group: Baishakhi, Shereen, Imran and Ben. I would like to thank Professor John Evans who has supported me and given new ideas.

I would like to thank all the member of University of Southampton for stimulating working environment. Thanks to the EUPF6 and Marie Curie for an early stage training fellowship.

I would like to express my heartiest thanks to Peppe, Maria, Rosa, Gerardo, and Salvo for their kindness and affection, and for never letting me feel that I was away from my family and country.

I am especially grateful to all my friends: Michael, Magda, Peter, Sarah and Rowena.

My special appreciation goes to my family. Unfortunately, my Mum is not here to share this with me, but I am sure she keeps an eye on me from heaven. And most of all, thanks to Sara for her understanding, endless patience, encouragement and love necessary to get this done.

# Publications

The following papers have been published during the course of this study:

1) "Direct Solvothermal Synthesis of Early Transition Metal Nitrides".
B. Mazumder, P. Chirico and A. L. Hector, Inorg. Chem., 2008, **47**, 9684.

2) "Solvothermal Synthesis of Gallium and Indium Nitrides Using Lithium Amide".
P. Chirico and A. L. Hector. Z. Naturforsch., 2010, **65b**, 1051.

3) "Solvothermal synthesis of group 5 and 6 nitrides via reactions using $LiNH_2$ and ammonia nitrogen sources".
P. Chirico, A. L. Hector and B. Mazumder, Dalton Trans., 2010, **39**, 6092.

# Definitions and abbreviations

| | |
|---|---|
| PXD | powder X-ray diffraction |
| GSAS | general structure analysis system |
| JCPDS | joint committee on powder diffraction standards |
| TEM | transmission electron microscopy |
| SEM | scanning electron microscopy |
| EDXA | energy dispersive X-ray analysis |
| IR | infrared spectroscopy |
| UV-Vis | ultraviolet-visible |
| TGA | termogravimetric analysis |
| HDA | hexadecylamine |
| CTAB | N-cetyltrimethylammonium bromide |
| TOA | trioctylamine |
| TOP | trioctylphosphine |
| TOPO | trioctylphosphine oxide |
| DR | duffuse reflectance |

# 1.1 Introduction

Nitride materials were first investigated at the beginning of the 20th century and significant progress in this field was made over several decades largely by Juza and co-workers.[1-4] Progress in nitrides has been rapid over recent years, due to improvements in synthetic methods and analytical techniques. Most binary nitrides are well characterized, while only relatively little (compared with ternary oxides and sulfides) is known about ternary nitrides. The rarity of nitrides is due to the larger energy required for the formation of the $N^{3-}$ anion compared with $O^{2-}$. Several reviews of nitride chemistry have appeared in recent years[5-11]. Each review describes different aspects of their chemistry such as structure[12, 13], high pressure phases[14], nitrides of the s-block elements[15], silicon nitrides ceramics[16], formation of ternary nitrides[13] etc. Other reviews of their applications in catalysis[17], phosphors[18], etc have been also reported.
Group 13 nitrides (AlN, GaN, InN) and their solid solutions such as InGaN, AlInGaN etc. in thin film form, have been widely investigated because of their applications in blue-UV optoelectronic and microelectronic devices.[19-21]
Silicon-based oxynitride and nitride phosphors have recently received attention because of their properties like luminescence, high stability and potential use for white light-emitting diodes (LEDs).[18] These systems activated by doping with rare-earth ions (e.g. $Eu^{2+}$ and $Ce^{3+}$) yielded high performance white LEDs.
Most applications of nitride materials are based on films deposited from the vapour phase. Properties such as hardness, catalytic activity and high conductivity have led these materials to several realised and potential uses described in the following sections. The growing interest in nitride materials in other relevant forms has led to new synthesis methods.

The work described in this thesis is concerned with materials in which nanocrystallinity is a major driver of their properties. The first part of this chapter describes the bonding and the structures of the most studied metal nitrides. Properties and applications will be then explored together with the different methods of preparation. The second part is focused on semiconductor nanocrystals, with particular attention to the preparation of colloidal gallium nitride.

## 1.2 Bonding and structures in nitride materials

Nitride materials are formed by combining nitrogen with less electronegative elements. Depending on the chemical characteristics of the bonds between nitrogen and other elements, they can be divided in three groups of compounds:

- ionic
- metallic
- covalent

Metals of groups 1,2,11 and 12 form ionic compounds with nitrogen by incorporation of $N^{3-}$ anions in their crystal lattice. $Li_3N$ was the compound most studied in the past[22-24], due to its easy preparation. Its structure was solved by Zintl and Brauer[24] in 1935. Nitrides of the heavier alkali metals of group 1 form unstable compounds (Table 1). An interesting trend was observed in the group 2 metals[15]. Descending the group, the structures become less ionic with increasing metal electropositivity. This behavior may be attributed to the incomplete coordination of the metal by the $N^{3-}$ anions. As a consequence the bonding in these compounds was not considered exclusively ionic and a metallic contribution was significant. The formation of sub-nitrides was evidenced in less electropositive alkaline earth metals, for example with strontium and calcium. Some of them such as $Sr_2N$[25], $Ca_2N$[26] have been structurally investigated. The subnitrides are usually structurally related to the alkali metal suboxides[27]. In both cases the structure contains anion-centered metal octahedra.

Metallic nitrides such as TiN, ZrN, VN, CrN, $Fe_2N$ etc. are usually formed by combining nitrogen with transition metals. Many of the transition metal nitrides (in particular those of the groups 4, 5 and 6) are interstitial compounds and possess metallic character. The nitrogen atoms enter into the interstitial sites between metallic lattice points and non-stoichiometry is common. The sites occupied are usually the largest available for example octahedral in fcc (face-centered cubic) and hcp (hexagonal close packed), and trigonal prismatic in hex (hexagonal).

**Table 1.** Classification of metal nitrides. Nitrides of groups 5, 6 and 13 marked in red and blue respectively have been investigated in this work. The empty boxes in the periodic table represent no known nitride phases according to ICSD[28].

| 1 | 2 | 3 | 4 | 5 | 6 | 7 | 8 | 9 | 10 | 11 | 12 | 13 | 14 | 15 |
|---|---|---|---|---|---|---|---|---|---|---|---|---|---|---|
| $Li_3N$ | $Be_3N_2$ | | | | | | | | | | | BN | $C_3N_4$ | |
| $Na_3N$ | $Mg_3N_2$ | | | | | | | | | | | AlN | $Si_3N_4$ | $P_3N_5$ PN |
| | $Ca_3N_2$ $Ca_2N$ | ScN | TiN $Ti_4N_3$ $Ti_3N_2$ $Ti_2N$ $Ti_3N_4$ | VN $V_2N$ | CrN $Cr_2N$ | MnN $Mn_3N_2$ $Mn_2N$ $Mn_4N$ | $Fe_2N$ $Fe_3N$ $Fe_4N$ | CoN $Co_2N$ $Co_3N$ $Co_4N$ | NiN $Ni_3N$ $Ni_4N$ | CuN $Cu_3N$ | $Zn_3N_2$ | GaN | $Ge_3N_4$ | |
| | SrN $Sr_2N$ $Sr_3N_2$ $Sr_4N_3$ | YN | $Zr_3N_4$ ZrN | NbN $Nb_4N_3$ $Nb_2N$ | MoN $Mo_2N$ $Mo_3N_2$ $Mo_5N_6$ | TcN $Tc_4N_3$ | $RuN_2$ | $RhN_2$ $RhN_3$ | $Pd_2N$ | $Ag_3N$ | $Cd_3N_2$ | InN | $Sn_3N_4$ $Sn_3N_2$ | |
| | $Ba_2N$ $Ba_3N$ $Ba_3N_2$ $BaN_2$ | LaN | HfN $Hf_3N_4$ $Hf_4N_3$ $Hf_3N_2$ | TaN $Ta_3N_5$ $Ta_2N$ $Ta_4N$ | WN $WN_2$ $W_2N$ $W_3N_4$ $W_5N_4$ | $Re_2N$ | $OsN_2$ | $IrN_2$ | PtN $PtN_2$ | $Au_3N$ $AuN_2$ | $Hg_3N_2$ | TlN | $Pb_3N_4$ $Pb_3N_2$ | |

| | | | | | | | | | | | | | |
|---|---|---|---|---|---|---|---|---|---|---|---|---|---|
| CeN | PrN | NdN | | SmN | EuN | GdN | TbN | DyN | HoN | ErN | TmN | YbN | LuN |
| $Th_2N_3$ $Th_3N_4$ ThN | $PaN_2$ PaN | $UN_2$ $U_2N_3$ UN | NpN | PuN | AmN | CmN | BkN | | | | | | |

Covalent nitrides are formed by combining nitrogen with elements of groups 13, 14 and 15 (e.g. BN, AlN, GaN, $Si_3N_4$, $P_3N_5$ etc.). Boron nitride is isoelectronic with carbon and occurs in two forms: resembling graphite (hexagonal wurtzite) and diamond (cubic zinc-blende). Similarly to carbon, it also forms nanotubes[29]. AlN normally has the hexagonal wurtzite type structure,[30] but unlike cubic BN which is normally achieved at high pressure, AlN has been prepared in both forms using different methods at ambient pressure[31]. GaN and InN also exist in the same hexagonal and cubic forms, though a third polymorph (NaCl-type) also forms under high pressure[32, 33]. Both the common structures have tetrahedral coordination with each atom bonded to four other atoms of opposite species. The bonding is predominately covalent with some ionic character.

$Si_3N_4$ and $Ge_3N_4$ possess two stable phases α-trigonal[34] and β-hexagonal[35] under ambient pressure, with the β-phase more stable than α-phase. The α ⟶ β phase transition was observed upon heating while the β ⟶ α transition has not been yet observed. The spinel type γ phases of both were obtained at high pressure[36, 37].The high stability in these structures is due to the formation of covalent bonding. β-$C_3N_4$ is metastable and has been formed as nitrogen deficient thin film. It has been predicted in computational studies to be harder than diamond[38].

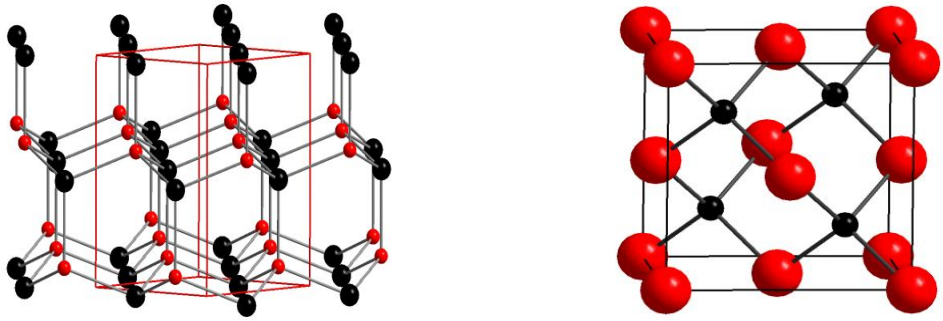

**(a)** **(b)**

**Figure 1** (a) Hexagonal (wurtzite) and (b) cubic (zinc blende) structures adopted by BN, AlN, GaN and InN.

# 1.3 Properties and applications

## 1.3.1 Film formation

Thin films of group 13 nitrides (AlN, GaN, InN) are typically produced using MOVPE (Metal-Organic Vapor Phase Epitaxy) or MOCVD (Metal-Organic Chemical Vapor Deposition) techniques[39-43]. Growth of epitaxial devices has been hindered by a lack of suitable substrates and group III nitride films have been most commonly prepared by MOCVD. The choice of the precursors plays an important role in the preparation of high quality films using MOCVD at high temperature. The issues of high temperature are associated to the presence of defects and thermal stresses in the films. However the formation of InN films and its alloys are difficult because of low dissociation temperature (~ 550 °C). Ideal precursors would be non pyrophoric, non toxic, water and oxygen insensitive and have good volatility, stability and reactivity. Many of these aspirations are not met by the precursors that are used. The growth of the group 13

nitrides was achieved from the reactions of $R_3M$ (R = $CH_3$, $C_2H_5$; M = Al, Ga, In) with $NH_3$[44]. Although these precursors were sufficiently volatile and reactive, different difficulties were associated with their use. The trialkyl-compounds are pyrophoric and water and oxygen sensitive while the ammonia is corrosive. Precursors such as triisopropyl compounds have been also investigated for the production of group III nitride films. These sources are an important alternative due to their lower pyrolysis temperature (below 250 ºC) and a lower carbon content was expected in the resulting films due to their efficient decomposition[45-47]. The preparation of films using non pyrophoric precursors such as $(CH_3)_3In{\cdot}N\text{-}(CH_3)_3$,[48] $(C_2H_5)_2InN(CH_3)_2$,[49] etc. have been also reported.

## 1.3.2 Electronic devices

Films of TiN, NbN and TaN have found applications as diffusion barriers in microelectronics[50-54]. Nitrogen-rich phases like $Zr_3N_4$, $Hf_3N_4$ and $Ta_3N_5$ exhibit different properties compared with those of the mononitrides. For example $Ta_3N_5$ (band gap 2.08 eV) is a red pigment and an active photocatalyst[55-57]. Zirconium and hafnium nitrides change from conducting to insulating as the composition changes from MN to $M_3N_4$.[58] The latter have applications in cryogenic thermistors and in Josephson junctions[59].

Group 13 nitrides have attracted interest in optoelectronic applications due to their highly attractive properties such as direct band gaps (ranging from 0.7 eV in InN to 3.4 eV in GaN and 6.2 eV in AlN), low compressibility and high thermal conductivity. BN and AlN are refractory and electrically insulating, while GaN and InN are semiconductors. These materials and their solid solutions (e.g. $Ga_{1-x}In_xN$) have been used to fabricate devices such as LEDs, lasers, flat panel displays[60-62] and transistors[63, 64], UV photodetectors[65-67] and surface acoustic wave devices[68, 69]. LEDs containing GaN as the active component are brighter than either conventional light bulbs or organic phoshide-based devices[70]. GaN has applications in high-speed/power devices that can operate at high temperature and are radiation resistant. Solid solutions of GaN and InN can tune the band gap to any value throughout the visible spectrum and into the ultraviolet region. Indium nitride has been less well studied than other nitrides, probably as result of its low thermal stability (425-550 °C).[39, 71]

### 1.3.3 Catalysis

Metal nitrides of group 5 and 6 have attracted a lot of interest in catalysis because of their excellent catalytic activity. The use of methods such as temperature-programmed reaction has led to the production of nitrides with high surface area. Early transition metals are electron deficient in their elemental state, and present high reactivity towards hydrocarbons[72]. The formation of interstitial compounds by incorporation of nitrogen increases the electron count and the reactivity can be controlled. For example in ammonia synthesis the replacement of ruthenium with $Mo_2N$ resulted in higher activity [73]. Ammonia synthesis has also been effective with $W_2N$, VN and vanadium oxynitride[74-76]. $Mo_2N$ was used in dehydrogenation, hydrogenolysis and isomerisation of butane[77]. Selectivities for different reactions varied widely within the nitride studied. $Mo_2N$ can also behave as a base catalyst in the conversation of acetone to isophorone and mesityl oxide[78]. Ternary nitrides such as $Co_3Mo_3N$, $Fe_3Mo_3N$ and $Ni_2Mo_3N$ were employed for the catalytic synthesis of ammonia at 400 ºC and ambient pressure. $Co_3Mo_3N$ prepared from cobalt molybdate hydrate ($CoMoO_4 \cdot nH_2O$) was stable under ammonia synthesis conditions and exhibited the highest activity in relation with molybdenum nitrides, $Fe_3Mo_3N$ and $Ni_2Mo_3N$[76]. The catalytic activity of $Co_3Mo_3N$ in $NH_3$ synthesis was further improved by the addition of alkali promoter (e.g. $CsNO_3$). Although the promoter decreased the surface area and retarded the formation of $Co_3Mo_3N$, $NH_3$ synthesis was more efficient than a doubly promoted iron catalyst (e.g. $Fe\text{-}K_2O\text{-}Al_2O_3$).

Nanocrystalline TiN has showed also catalytic properties. It has been used for example to accelerate hydrogen transfer in the reaction of diphenylethyne (DPE) with $NaAlH_4$.[79] The uncatalyzed reduction of DPE was slow at 328 K and produced two isomers (E- and Z-stilbene) in ratio 70:30. The activation of the reaction with TiN was faster and highly stereroselectivity towards the formation of Z-stilbene (~90 %). An almost complete conversion (~ 99 %) in isomers E-(10 %) and Z-stilbene (90 %) was produced after 5 h. In the hydrogenation of DPE, TiN decomposes the alanate ($NaAlH_4$) into NaH and $AlH_3$, Then $AlH_3$ is responsible for the reduction and the selectivity of Z-stilbene[79]. Nitrides used in catalysis have been usually prepared from oxide precursors and a lot interest is addressed toward the production of nitride phases by other routes (for example solvothermal method).

### 1.3.4 Photocatalysis

$Ta_3N_5$ has a band gap of 2.08 eV[55] and is an active photocatalyst which absorbs in the visible region. It is more efficient than $TiO_2$ which absorbs mostly under UV irradiation. $TiO_2$ has a wide band gap ranging from 3 eV for rutile to 3.2 eV for anatase and this represents a limitation in its use because the most intense region in the solar spectrum is around 2.6 eV.[80] Different works have been addressed towards the improving of the photocatalytic properties of $TiO_2$ with the aim to extend its absorption into the visible region. The photocatalytic activity of $Ta_3N_5$ and nanocrystalline $TiO_{2-x}N_x$ were investigated in mesitylene blue degradation.[81] In that work $Ta_3N_5$ showed higher activity than $TiO_{2-x}N_x$ of the same size. The use of carbon nanotube composite (CNTs/$Ta_3N_5$) photocatalysts presented higher photocatalytic activity than pure $Ta_3N_5$ in the degradation of mesytilene blue.[82] $Hf_3N_4$ can be also used as a photocatalyst.[83]

### 1.3.5 Hard coatings

Hard protective coatings have applications in machine tools, suspension components, drilling, cutting, milling etc. Ideal materials for such applications must be hard, resistant against oxidation and have low coefficient of friction[84].
Metal nitrides of group 4 (TiN, ZrN and HfN) and 5 (VN, NbN and TaN) have been used as hard protective coatings for cutting tools[85, 86] and UHV system components[87].
Although different materials possess a high hardness the choice of good candidates is often difficult. For example amorphous carbide has a high hardness but its use is limited because of the easy oxidation at low temperature while polycrystalline diamond films forms alloys at high temperature with materials like steel or iron.
The increasing requirements in superhard coatings have led to development of composite nanocrystalline/amorphous materials. Composite materials of TiN, $W_2N$ and VN were prepared by embedding in an amorphous $Si_3N_4$ matrix.[84, 88-90] The resulting films exhibited high hardness and stability to oxidation up to more 800 °C.
In TiN/$Si_3N_4$ it was found that the hardness enhanced by adding $Si_3N_4$ and this was accompanied by a decrease of the TiN particle size.[91] The maximum value of hardness (35 GPa) was obtained using a silicon content of ~ 10 atomic percent. Films deposited on steel exhibited hardness of 50 GPa. $W_2N/Si_3N_4$ was also investigated in a similar way and it showed similar hardness.[89]

## 1.3.6 Electrochemical capacitors.

Electrochemical capacitors are unique devices because of their 20-200 times greater capacitance than conventional capacitors[92]. They are high power storage devices with applications for example in electric vehicles, cellular phones, pacemakers, air bags, etc. There two types of supercapacitors, the electrochemical double-layer capacitors (EDLC) and pseudocapacitors[93]. The first store the energy within the double layer at the electrode/electrolyte interface through reversible ion adsorption onto the electrode surface. High surface area activated carbon is typically used as electrode material. Other carbon materials such as carbon nanotubes or fibers have been employed as electrode materials. These materials exhibit interesting properties like high surface area, good electrical conductivity and chemical stability. Pseudocapacitors store electrochemical charge by battery-type redox reactions at the surface of the electrodes. Several metal oxides like $RuO_2$[94], $MnO_2$[95], $TiO_2$[96], $IrO_2$[97] have been used as electrode materials in pseudocapacitors. Crystalline $RuO_2$[98] and amorphous $RuO_2 \cdot nH_2O$[94, 99] exhibited high capacitance of 350 and 720 F/g, respectively[100]. They are good electrode materials but their expensive nature has led towards the investigation of different materials.

Metal nitrides such as VN, TiN WN and $MoN_x$ represent good alternative pseudocapacitor electrode materials because of their high conductivity and chemical resistance. VN nanocrystals were prepared reacting $VCl_4$ with ammonia using chloroform as solvent and fired at temperatures of 400 and 1000 ºC.[100] Rock-salt VN with particle size of about 6 nm was obtained at 400 ºC with a specific area of 38.8 $m^2 g^{-1}$, while crystallites of 58 nm were prepared at 1000 ºC with a specific area of 2.4 $m^2 g^{-1}$. The specific capacitance measured from VN prepared at 400 ºC was 1340 F/g at a scan rate of 2 mV $s^{-1}$, 554 F/g at 1000 mV $s^{-1}$ and 190 F/g at a scan rate of 2 V $s^{-1}$. VN formed at 1000 ºC showed a capacitance of ~ 58 F/g at a scan rate of 2 mV $s^{-1}$. These high values of specific capacitance evidence the potential use of metal nitrides in electrochemical devices. The formation of oxide and oxynitride on the surface was shown to be responsible for the high specific capacitance. Nanocrystalline TiN[101] was prepared by ammonolysis of titanium chloride at 400 ºC, high surface area of ~ 129 $m^2 g^{-1}$ and specific capacitance of 238 F/g were measured at a scan rate of 2 mV $s^{-1}$. $\gamma$ $Mo_2N/Co_3Mo_3N$ was investigated as a composite electrode material.[102] Compared with $RuO_2$, the composite material has low cost. The starting material $CoMoO_4$ was prepared with different mole ratios $n_{Co}$ = Co/Co+Mn by mixing cobalt nitrate ($Co(NO_3) \cdot 6H_2O$) and ammonium heptamolybdate ($(NH_4)_6Mo_7O_{24} \cdot 4H_2O$). The resulting material was then reacted with ammonia. The specific capacitance was measured by changing $n_{Co}$. The maximum value of ~ 210 F/g was obtained with $n_{Co}$ = 0.25. For $n_{Co}$ = 0.5 the specific

capacitance decreased to about 70 F/g. The addition of amorphous $Ta_2O_5$ into $Mo_2N$ was also studied.[92] The specific capacitance was increased from 30 to ~ 105 F/g by increasing the amount of Ta from $n_{Ta} = 0$ to $n_{Ta} = 0.25$.

# 1.4 Synthesis of metal nitrides

Metal nitrides have been prepared using many different methods. The most common synthesis routes traditionally were high temperature reactions of metal powder with an $N_2$ or $NH_3$ flow, or ammonolysis of metal chlorides, oxides, or sulfides[103-107]. Carbothermal reduction and nitridation of metal oxides in a nitrogen or ammonia atmosphere was also reported[108-111]. Milling, solid-state metathesis and precursor decomposition represent some of the other routes recently used to synthesize them. Some of these methods required rigorous reaction conditions such as high temperature and air sensitive or expensive reagents, which was not economically profitable. In this section a general discussion on some of these will be presented. Special attention will be given to those methods (solvothermal and colloidal) which have been further developed in this work to prepare nanocrystalline nitrides.

## 1.4.1 Milling

Mechanical milling has attracted a lot interest for the synthesis of amorphous and metastable phases, intermetallic compounds and ceramic materials[112-117]. The method involves a direct reaction of metal powder with $N_2$ or $NH_3$ using ball milling. The milling process generates new clean metal surfaces which can absorb nitrogen. The shearing action of the balls is a key factor in the formation of new surfaces. Although the absorption of nitrogen into the surface is not clear, the collisions between the balls improve the rate of absorption. This can be due to faster nitrogen diffusion because of the high local temperature generated during milling action[118].
The nitridation process can be improved by increasing the nitrogen pressure. In this way more collisions between the balls and the powder can be produced. For example, pure nanocrystalline CrN, with particle size of 6 nm, was prepared through milling from chromium metal under a nitrogen pressure[119]. The milling time was of 50 h and no heating treatment was necessary to crystallize the material. The preparation of metastable phases such as NbN[120], $Ta_2N$[121], $\beta$-$C_3N_4$[122] and h-BN[123] nanorods were also reported. TiN was achieved by ball milling a mixture of titanium metal powder with pyrazine ($C_4H_4N_2$) in a benzene solution[124]. The reaction rate was expected to be faster than that under dry milling because the solvent improved the contact between the reagents. This wet milling led to an intermediate $Ti_2N$ which was not obtained using

dry milling. After increasing milling time (336 h) and heating up to 1200 ºC for 5 min,$Ti_2N$ was transformed to TiN. Ball milling has been also used to prepare $Fe_3Mo_3N$ and $Co_3Mo_3N$[125].
The method has the advantage of a low cost and offers an easy way to prepare materials in large quantities. The main disadvantages are long reaction times (several days), large pressures ($N_2$ or $NH_3$) to obtain appreciable reaction rate, contamination of the end products and inhomogeneous products due to incomplete reactions.

### 1.4.2 Solid-state metathesis

Solid-state metathesis reactions have been effective in the preparation of nitrides and other materials that were difficult to make by traditional methods[126]. The initiation of the reaction can be realized in different ways such as grinding reagents together at room temperature, heating in a furnace or igniting with a filament. Reactions are usually highly exothermic and rapid (reaction time of a few seconds). As a consequence of the short reaction time, the reaction products usually have a small particle size. Metal nitrides have been achieved by the reaction of metal halides with different nitrogen sources such as $Li_3N$[127], $Mg_3N_2$[128], $Ca_3N_2$[128] and $NaN_3$[129]. The preparation of some nitrides such as GaN (dec. temp. 877 ºC), InN (dec. temp. 427-500 ºC), $Zn_3N_2$ (~500 ºC) or $Ta_3N_5$ (900 ºC) was difficult because of the high temperature generated during the reactions. However the reaction temperature can be controlled by adding inert diluents which absorb part of the heat produced during the reaction. Diluents decreasing the temperature of reaction can lead to the formation of phases which would otherwise thermally decompose. This method has the advantages of rapidity and sometimes formation of different phases to more conventional conditions. In the mean time the particle aggregation is still a problem though it can be improved by dilution of the reaction e.g. with excess alkali halides.

### 1.4.3 Molecular precursors

Nanocrystalline solids can be also prepared using molecular precursors. The preparation of nitride material can be achieved using single-source precursors which contain pre-formed M-N bonds or using a dual nitrogen source. In the latter case the nitrogen can be added from a second reagent (e.g. $NH_3$). The method has some advantages compared with solid state synthesis, in that the reactions occur at lower temperature and that reduced contamination from other species (e.g. carbon) can sometimes be achieved and in some cases (e.g. cubic GaN) unusual phases can be formed[130-132]. The compounds prepared are usually amorphous and an annealing step is

required to crystallize the products[130-132]. Crystallite size can be controlled by changing reaction conditions such as time and temperature. The preparation of nanocrystalline GaN by precursor decomposition has been reported using for example $[H_2GaNH_2]_3$,[130-132] $[Ga(NH_{3/2})]_n$[133], $[Ga(NMe_2)_3]_2$[134], $NR_3[Ga(N_3)_3]$[135] etc. GaN colloidal nanoparticles were also produced from precursor decomposition, such as using $[Ga(NMe_2)_3]_2$ in the presence of a capping agent. This route to GaN will be widely discussed in chapter 6.
The reactions of transition metal dialkylamides with ammonia in hydrocarbon solvents followed by pyrolysis were also used to prepare transition metal nitrides[136].

## 1.4.4 Solvothermal method

Solvothermal processes can be defined as reactions occurring in a closed system in the presence of a solvent above its boiling temperature[137]. As a consequence the system generates high pressure. It can be autogeneous or imposed at the start of the experiment. When it is autogeneous its value depends on the filling of the reaction vessel. Depending on pressure and temperature, the solvothermal system can be heterogeneous or homogeneous and in subcritical or supercritical conditions. Initially these reactions were developed in aqueous solution for the preparation of minerals[138]-zeolites[139], novel materials[140], deposition of thin films[141], particle with defined size and morphology[142] and for the crystal growth of functional materials[143, 144]. However the growing interest in non-oxide material such as nitrides, phosphides, selenides, etc. has led to the development of new processes involving non aqueous solvents.

### 1.4.4.1 Important factors in a solvothermal process

In order to understand these processes two different factors involved in these reactions will be briefly discussed. They can be divided into two types:

- chemical (concentration of precursors, solvent)
- thermodynamic (temperature, pressure)

**Chemical factors** are dependent on the nature of reagents and on the physico-chemical properties of the solvent. The concentration of the precursors is important to control the shape of the crystallites prepared. This dependence was previously shown by Wang and co-workers in the solvothermal preparation of CdSe and CeTe nanocrystals.[145]. They prepared nanocrystals of different shapes such as dot, rod, etc. by changing only the initial precursor concentrations.
In the solvothermal reactions the interaction between reagents and solvent is important because the solvent controls the chemical mechanism leading to the final

material. An important example of the role played by the solvent in a solvothermal process was reported by Li et al[146]. They synthesized nanocrystalline $Cu_7Te_4$ by the reaction of $CuCl_2 \cdot 2H_2O$ and tellurium in different solvents. When ethylenediamine was used as solvent, hexagonal $Cu_7Te_4$ with particle size of about 15 nm was prepared, while in the presence of other solvents such as benzene or diethylamine the tellurium did not react with copper chloride. This result was due to the strong polarity and to the presence of bidentate ligands of ethylenediamine. The physico-chemical properties of the solvent are also important in the formation of particular phases. Another example of the different behavior of the solvent was investigated by Lu et al[147] on the synthesis of MnS.

MnS was prepared from the reaction of $MnCl_2 \cdot 4\ H_2O$ with $SC(NH_2)_2$ using different solvents at temperature in the range 190-200 ºC. When water or ethylenediamine were used as solvent, $\alpha$-MnS with rock-salt structure was achieved. The same reaction in benzene as solvent yielded the wurtzite-type structure $\gamma$-MnS, while with tetrahydrofuran only the zinc-blende structure $\beta$-MnS was observed. The formation of Mn complex [$Mn(H_2O)_6^{2+}$ and $Mn(en)_3^{2+}$] when water or ethylenediamine were used, was responsible for the formation of stable form, $\alpha$-MnS. Metastable forms ($\beta$, $\gamma$) were favorable using benzene or THF. It is worth noticing that the solubility of the precursors in different solvents is different and it can leads to the formation of particular phases.

**Thermodynamic factors** are correlated with temperature and pressure. Usually the reaction temperature in a solvothermal process is less than 400 ºC. Pressure and temperature play a key role because they are involved in the solubility mechanism of the starting materials. Increasing of these parameters can be an advantage because of the major interaction between precursors and solvent. In a solvothermal process a change in temperature can lead to the modification of different factors such as: solubility and stability of the reactants, the chemical composition of the solvent, the kinetics of reaction and, in transition metal nitrides, their formal oxidation state.

# 1.5 Semiconductor nanocrystals

## 1.5.1 Theorical considerations

This section begins with a general discussion on the theoretical aspects involved in the preparation of semiconductor nanocrystals. The concepts of quantum confinement and growth of nanoparticles in solution will be examined. Previous research on II-VI and III-V semiconductors will be reviewed and addressed to the synthesis of GaN produced in this work.

## 1.5.2 Quantum confinement

Quantum confinement is an important feature of semiconductor nanocrystals. They represent a system lying between the semiconductors and molecules. In the bulk the overlapping of the orbitals leads to the formation of bands separated by a band gap (Figure 2). $E_g$ represents the minimum energy necessary to excite an electron from the valence band to the semiconductor band. When an electron absorbs a photon of energy greater than $E_g$, it is excited to the conduction band leaving a positive charge (hole). The electron and the hole are attracted by Coulomb forces and can form an exciton[148]. The size of the exciton within the crystals can be described using the equation 1.1:

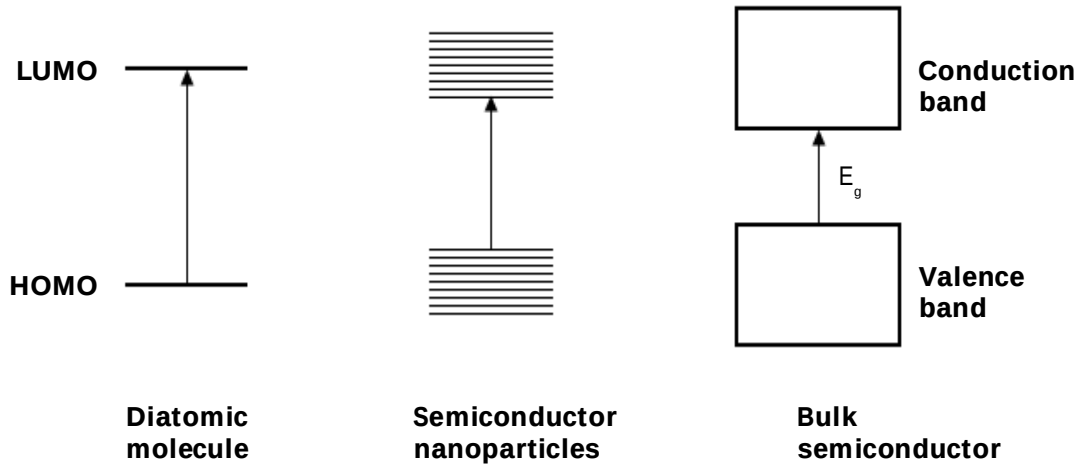


**Figure 2**. Band structure diagrams showing the intermediate properties of semiconductor nanoparticles between molecules and bulk materials.

$$a_B = \frac{h^2 \varepsilon}{4\pi^2 e^2}\left[\frac{1}{m_e^*} + \frac{1}{m_h^*}\right] \qquad \text{Eq.1.1}$$

From the equation $a_B$ (Bohr radius of the bulk exciton) depends on $m_e^*$ and $m_h^*$ (effective masses of the electron and holes) and on $\varepsilon$ (the dielectric constant of the material), h is Planck`s constant, $e$ is the charge on the electron in C. $a_B$ can vary from 1 nm to more than 100 nm depending on the material. Semiconductor nanocrystals with size smaller than $a_B$ lead the charge carrier to be spatially confined. In the presence of quantum confinement the continuous bands split into discrete levels and the electronic excitation moves to higher energy. Only a few transitions are allowed and the properties of the nanocrystals depend on their size. As a consequence the optical absorption will be shifted to higher energy according to the Brus equation[149, 150]:

$$E_{np} = E_g + \frac{h^2}{8\,r^2}\left[\frac{1}{m_e^*} + \frac{1}{m_h^*}\right] - \frac{1.8\,e^2}{4\pi\varepsilon\varepsilon_0 r} - 0.248\,E_{Ry}^* \qquad \text{Eq.1.2}$$

where $E_{np}$ is calculated from the exciton absorption peak of the nanoparticle in J, the bulk band gap, $E_g$ is calculated from the bulk semiconductor band gap in J, r is the radius of the particle in meters, $\varepsilon_0$ is the vacuum permittivity constant in $C^2\,J^2\,m^{-1}$ and $0.248\,E_{Ry}^*$ is the effective Rydberg energy ($e^2/2\varepsilon^2h^2\,(m_e^{-1} + m_h^{-1})$), which is generally small.

Eq. 1.2 shows the dependence of the particle size on the energy of the band gap. By decreasing the particle size the band gap increases. This changing has an important effect on the optical properties of the semiconductors. For this reason new methods of synthesis have been focused on the preparation of nanocrystals of particular sizes.

## 1.6 Nanocrystals growth in solution

The preparation of nanocrystals can be achieved through thermal decomposition of a precursor in hot solvent at high temperature. The following steps are typically involved in the synthesis of nanocrystals:

- Nucleation
- Growth
- Size-selective precipitation

In order to obtain nonocrystallites of uniform size the nucleation of the particles must be fast (order of seconds) and separated in time from the growth. Previous work on the preparation of II-VI nanocrystals has showed that polydispersities in size and shape yielded issues in the interpretation on their optical properties[151]. The production of particles of a controlled size is fundamental for taking advantage of quantum confinement effects. This can be done through the preparation of particles in the presence of capping agents or surfactants. The role of the surfactant is to coordinate or bond to the nanocrystal surface. It helps to control the size of the particles inhibiting aggregation. The choice of the surfactant determines the solubility of the nanocrystal by giving them a hydrophilic or hydrophobic surface[148].
The surfactant usually contains an electron-rich donating group such as phosphine oxides, phosphines, amines, etc. that behave as a Lewis bases and coordinate to the electron-poor Lewis acid-like metal sites of the semiconductor[148]. The weak coordination bonds of most surface-surfactant systems allow these molecules to be exchanged in order to improve some properties as for example the luminescence[148].
Size-selective precipitation often represents the last stage of the synthesis. It is usually used to improve the size distribution. In order to destabilize the dispersion of the large particles a non-solvent can be added to the solution leading to precipitation of the large nanocrystals. The complete separation is then achieved by centrifugation.

## 1.6.1Previous research in solution phase nanocrystal growth

The preparation of colloidal nanocrystalline particles has attracted a lot of interest because of their unique properties. Although a lot progress has been made in the interpretation of II-VI compounds such as CdSe, CdS, CdTe, and ZnSe, the preparation of optical experiments sometimes was difficult[151]. The main problems were due to the preparation of semiconductor polydispersities in size and shape, that often had high concentrations of defects on the surface and frequently also had poor crystallinity. The preparation of III-V semiconductors was more difficult because the compounds required high temperature and the solution chemistry is not well developed[152]. Moreover at high temperature the crystallization of the compounds was improved but the particles tended to aggregate. An important consequence was that the particle precipited could be not in a regime of quantum confinement. An important step forward in the preparation of III-V semiconductor was made by Mićić and co-workers who prepared and characterised InP[152-158] and GaP[154]. InP was synthesised by the reaction of chloroindium oxalate complex with $P(SiMe_3)_3$ in $CH_3CN$ as solvent at room temperature. The orange solution of InP prepared was heated at 270 ºC for 3-6 days in the presence of TOPO-TOP as agent capping. Crystalline zinc-blende InP with particle size of 25 Å was produced. The use of TOPO/TOP as colloidal stabilizer was previously reported in the preparation of CdSe nanocrystallites[151]. They showed that the coordinating solvent was important in controlling the growth process, stabilizing the resulting colloidal dispersion and electronically passivating the semiconductor surface. GaP was also prepared by the reaction of $P(SiMe_3)_3$ with gallium chloride or chlorogallium oxalate complex. The precursor was the heated in TOPO/TOP at 270-400 ºC yielding a zinc-blende GaP. The particle size was 30 nm. The preparation of InAs[159, 160] was achieved by the reaction of $InCl_3$ with $As(SiMe_3)_3$ at temperature ranging from 240-265 ºC. The synthesis was effective only in the presence of TOP which has been used as solvent and capping agent. Isolated nanocrystals in the range from 25 to 60 Å in diameter were prepared. Alivasatos and co-workers prepared GaAs nanocrystals[161-166] by the reaction of $GaCl_3$ and $As(SiMe_3)_3$ in quinoline. The reaction mixture was heated at 240 ºC for 3 days. Zinc-blende type GaAs with particle size of 45 Å was produced.The absorption spectrum showed quantum confinement effects (the exciton diameter in GaAs is 190 Å).

### 1.6.2 Colloidal GaN and InN nanocrystals

GaN is an important III-V semiconductor; its band gap is wide ranging from 3.1 eV in the wurtizite-type structure to 3.4 eV in the zinc-blende. Since the exciton Bohr radius is about 25 Å, GaN nanocrystals equal or smaller than 50 Å in diameter, show quantum confinement. An important consequence of this is visible from the optical absorption spectrum of the materials prepared. As discussed before there is a dependence between band gap and particle size. From equation 1.2 it is expected that the optical absorption will be shifted at higher energy by reducing the particle size. The growth of the particles can be monitored taking aliquots of the reaction solution at different instant of time by recording the absorption spectrum. In this way particles of specific size may be isolated. In order to study the optical properties of the nanoparticles the samples should be monodisperse in size and shape. GaN nanocrystals have been prepared using different methods. These offered minimal control on the particle size and the nanocrystals prepared could not be dispersed in solution. Hence the investigation of optical properties was difficult. Although GaN is an important material, due to its difficulties in the preparation only a few studies have been reported. In this work the synthesis of gallium nitride was studied using gallium amides as precursors in the presence of capping agents such as HDA/TOA. Colloidal group 13 nitrides were also achieved from the reaction of $MCl_3$ (M = Al, In and Ga) with urea in trioctylamine (TOA)[167].

## 1.7 Thesis organization

This thesis is organized in the following way. Chapter 2 describes the techniques used for synthesis and characterization of materials produced in this work. Chapter 3 deals with solvothermal reactions of gallium and indium halides with lithium amide in benzene as solvent. Chapters 4 and 5 focus on the preparation of group 5 and 6 nitrides via reactions using $LiNH_2$ and $NH_3$ (used as nitrogen sources) respectively. Chapter 6 is concerned with the synthesis of GaN by pyrolysis of gallium amides in the presence of hot coordinating solvents. Finally, chapter 7 provides a review of the main conclusions that can be drawn from the work described in this thesis and provides recommendations for future research.

# 1.8 References


1. R. Juza, K. Langer and K. V. Benda, *Angew. Chem. , Int. Ed. Engl.*, 1968, **7**, 360.
2. R. Juza and H. Hahn, *Z. Anorg. Allg. Chem.*, 1938, **239**, 282.
3. R. Juza and W. Sachsze, *Z. Anorg. Allg. Chem.*, 1945, **253**, 95.
4. R. Juza, A. Gabel, H. Rabenau and W. Klose, *Z. Anorg. Allg. Chem.*, 1964, **329**, 136.
5. R. Niewa and H. Jacobs, *Chem. Rev.*, 1996, **96**, 2053.
6. F. J. Di Salvo and S. J. Clarke, *Curr. Opin. Solid State Mater. Sci.*, 1996, **1**, 241.
7. R. Kniep, *Pure Appl. Chem.*, 1997, **69**, 185.
8. C. Rohr, *Angew. Chem. , Int. Ed. Engl.*, 1996, **35**, 1199.
9. T. Schleid, *Eur. J. Solid State Inorg. Chem.*, 1996, **33**, 227.
10. A. Simon, *Coord. Chem. Rev.*, 1997, **163**, 253.
11. W. Schnick and H. Huppertz, *Chem. Eur. J.*, 1997, **3**, 679.
12. D. H. Gregory, *J. Chem. Soc., Dalton Trans.*, 1999, 259.
13. R. Niewa and F. J. Di Salvo, *Chem. Mater.*, 1998, **10**, 2733.
14. E. Horvath-Berdon, R. Riedel, A. Zerr, P. F. McMillan, G. Auffermann, Y. Prots, W. Bronger, R. Kniep and P. Kroll, *Chem. Soc. Rev.*, 2006, **35**, 987.
15. D. H. Gregory, *Coord. Chem. Rev.*, 2001, **215**, 301.
16. R. L. Riley, *J. Am. Ceram. Soc.*, 2000, **83**, 245.
17. J. S. J. Hargreaves and D. Mckay, *Catalysis*, 2006, **19**, 84.
18. R. J. Xie and N. Hirosaki, *Sci. Technol. Adv. Mater.*, 2007, **8**, 588.
19. A. J. Steckl and R. Birkhahn, *Appl. Phys. Lett.*, 1998, **73**, 1700.
20. A. A. Andreev, *Phys. Solid State*, 2003, **45**, 419.
21. K. P. O. Donnell and B. Hourahine, *Eur. Phys. J. Apply. Phys.*, 2006, **36**, 91.
22. L. Ouvrard, *C. R. Acad. Sci. Paris*, 1892, **114**, 120.
23. R. Brill, *Z. Kristallogr.*, 1927, **65**, 94.
24. E. Zintl and G. Brauer, *Z. Elektrochem.*, 1935, **41**, 102.
25. N. E. Brese and M. O. Keeffe, *J. Solid State Chem.*, 1990, **87**, 134.
26. E. Keve and A. Skapski, *Inorg. Chem.*, 1968, **7**, 1757.
27. A. Simon, *Struct. Bond.* , 1979, **36**, 81.
28. *Inorganic Crystal Structure Database accessed via "The United Kingdom Chemical Database Service" D. A. Fletcher, R. F. McMeeking and D. Parkin, J. Chem. Inf. Comput. Sci.*, 1996, **36**, 746.
29. N. G. Chopra, R. J. Luyken, K. Cherrey, V. H. Crespi, M. L. Cohen, S. G. Louie and A. Zettl, *Science*, 1995, **269**, 966.
30. H. Schultz and H. H. Thiemann, *Solid State Commun.*, 1977, **23**, 815.
31. A. W. Weimer, *Carbide, Nitride and Boride Mater., Chapman & Hall, London, 1997.*

32. D. Elwell and M. M. Elwell, *Prog. Cryst. Growth Charact.*, 1988, **17**, 53.
33. C. Falter, M. Klenner and Q. Chen, *Phys. Rev. B*, 1993, **48**, 16690.
34. M. Billy, J. C. Labbe, A. Selvaraj and G. Roult, *Mater. Res. Bull.*, 1983, **18**, 921.
35. R. Grün, *Acta Crystallogr. Sect. B*, 1979, **35**, 800.
36. A. Zerr, G. Miehe, G. Serghiou, M. Schwartz, E. Kroke, R. Riedel, H. Fuess, P. Kroll and R. Boehler, *Nature* 1999, **400**, 340.
37. K. Leinenweber, M. O`Keeffe, M. Somayazulu, H. Hubert, P. F. McMillan and G. H. Wolf, *Chem.-Eur, J.*, 1999, **5**, 3076.
38. A. Y. Liu and M. L. Cohen, *Phys. Rev. B*, 1990, **41**, 10727.
39. D. A. Neumayer and J. G. Ekerdt, *Chem. Mater*, 1996, **8**, 9.
40. H. Monkoc, S. Strilé, G. B. Gao, M. E. Lin, B. Sverdlov and M. Burns, *J. Appl. Phys.*, 1994, **76**, 1363.
41. B. Garni, J. Ma, N. Perkins, J. Liu, T. F. Kuech and M. G. Lagally, *Appl. Phys. Lett.*, 1996, **68**, 1380.
42. S. D. Lester, F. A. Ponce, M. G. Craford and D. A. Steigerwald, *Appl. Phys. Lett.*, 1995, **66**, 1249.
43. F. A. Ponce, D. A. Bour, W. Götz and P. J. Wright, *Appl. Phys. Lett.*, 1996, **68**, 57.
44. J. Karpinski, J. Jun and S. Porowski, *J. Cryst. Growth*, 1984, **66**, 1.
45. T. F. Kuech, E. Veuhoff, T. S. Kuan, V. Deline and R. Potemski, *J. Cryst. Growth*, 1986, **77**, 257.
46. S. K. Shastry, S. Zemon, D. G. Kenneson and G. Lambert, *Appl. Phys. Lett.*, 1988, **52**, 150.
47. D. A. Bohling, C. R. Abernathy and K. F. Jensen, *J. Cryst. Growth*, 1994, **136**, 118.
48. V. Souliére, P. Abraham, J. Bouix, M. P. Berthet, Y. Monteil, A. M. Pougnet, R. Mellet, A. Ougazzaden and A. Mircea, *J. Cryst. Growth*, 1992, **124**, 93.
49. G. Rossetto, R. Franzheld, A. Camporese, M. L. Favaro, G. Torzo, D. Ajo and P. Zanella, *J. Cryst. Growth*, 1995, **146**, 511.
50. C. H. Winter, *Aldrichim. Acta*, 2000, **33**, 3.
51. L. McElwee-White, *Dalton Trans.*, 2006, 5327.
52. H. Tiznado, M. Bouman, B. C. Kang, K. Lee and F. Zaera, *J. Mol. Catal. A*, 2008, **281**, 35.
53. X. Q. Wang and A. Yoshikawa, *Prog. Cryst. Growth Charact. Mater.*, 2004, **48-9**, 42.
54. R. Oliver, *Mater. Sci. Tech.*, 2002, **18**, 1257.
55. C. M. Fang, E. Orhan, G. A. de-Wijs, H. T. Hintzen, R. A. de-Groot, R. Marchand, J.-Y. Saillard and G. de-With, *J. Mater. Chem.*, 2001, **11**, 1248.
56. M. Jansen, E. Guenther and H. P. Letschert, *German patent 199 07 618.9*, 1999.
57. S. J. Henderson and A. L. Hector, *J. Solid State Chem.*, 2006, **179**, 3518.

58. R. A. Andrievski, *J. Mater. Sci.*, 1997, **32**, 4463.
59. K. Schwarz, A. R. Williams, J. J. Cuomo, J. K. E. Harper and H. T. G. Hentzell, *Phys. Rev. B: Condens. Matter Mater. Phys.*, 1985, **32**, 8312.
60. S. Nakamura, *Blue Laser Light Emitting Diodes [Int. Symp.]*, 1996, 119.
61. F. A. Ponce and D. A. Bour, *Nature (London)*, 1997, **386**, 351.
62. M. A. Khan, Q. Chen, J. W. Yang, C. J. Sun, B. Lim, M. Z. Anwar, M. Blasingame, M. S. Shur and H. Temkin, *Blue Laser Light Emitting Diodes [Int. Symp.]*, 1996, 283.
63. S. Strite and H. Morkoç, *J. Vac. Sci. Technol. B*, 1992, **10**, 1237.
64. S. Strite, M. E. Lin and H. Morkoç, *Thin Solid Films*, 1993, **231**, 197.
65. M. A. Khan, J. N. Kuznia, D. T. Olson, J. M. V. Hove, M. Blasingame and L. F. Reitz, *Appl. Phys. Lett.*, 1992, **60**, 2917.
66. M. A. Khan, J. N. Kuznia, D. T. Olson, M. Blasingame and A. R. Bhattarai, *Appl. Phys. Lett.*, 1993, **63**, 2455.
67. K. S. Stevens, M. Kinniburgh and M. Beresford, *Appl. Phys. Lett.*, 1995, **66**, 3519.
68. H. Okano, N. Tanaka, Y. Takahashi, T. Tanaka, K. Shibata and S. Nakano, *Appl. Phys. Lett.*, 1994, **64**, 166.
69. H. Okano, N. Tanaka, K. Shibata and S. Nakano, *Jpn. J. Appl. Phys.*, 1993, **32**, 4052.
70. G. Fasol, *Science (Washington, DC)*, 1996, **272**, 1751.
71. I. Akasaki and H. Amano, *J. Cryst. Growth*, 1995, **146**, 455.
72. S. T. Oyama, *Catal. Today*, 1992, **15**, 179.
73. M. Boudart, S. T. Oyama and L. Leclecq, *Proc. 7th Int. Cong. Catal., Tokyo 1980, T. Seiyama and K. Tanabe (Eds.), Vol. 1, p. 587, Kodansha, 1980.*
74. S. T. Oyama, *J. Catal.*, 1992, **133**, 358.
75. M. R. Hillis, C. Kemball and M. W. Roberts, *Trans. Faraday Soc.*, 1966, **62**, 3570.
76. R. Komija and K. I. Aika, *Appl. Catal. A: Gen.*, 2001, **215**, 149.
77. M. K. Neylon, S. Choi, H. Kwon, K. E. Curry and L. T. Thompson, *Appl. Catal. A: Gen.*, 1999, **183**, 253.
78. S. K. Bej and L. T. Thompson, *Appl. Catal. A: Gen.*, 2004, **264**, 141.
79. S. Kaskel, K. Schlichte and T. Kratzke, *J. Mol. Catal. A: Chem.*, 2004, **208**, 291.
80. C. G. Granqvist, *Adv. Mater.*, 2003, **15**, 1789.
81. Q. Zhang and L. Gao, *Langmuir*, 2004, **20**, 9821.
82. B. Fu, L. Gao and S. Yang, *J. Am. Ceram. Soc.*, 2007, **90**, 1309.
83. J. Li, D. Dzinvenko, A. Zerr, C. Fasel, Y. Zhou and R. Riedel, *Z. Anorg. Allg. Chem.*, 2005, **631**, 1449.
84. S. Vepřek and S. Reiprich, *Thin Solid Films*, 1995, **268**, 64.

85. R. Buhl, H. K. Pulker and E. Moll, *Thin Solid Films*, 1981, **80**, 265.
86. J. E. Sundgren, *Thin Solid Films*, 1985, **128**, 21.
87. K. Moriyama, *Mat. Res. Soc. Bull.*, 1990, **15**, 32.
88. S. Vepřek, S. Reiprich and L. Shizhi, *Appl. Phys. Lett.*, 1995, **66**, 2540.
89. S. Vepřek, M. Haussmann and S. Reiprich, *J. Vac. Sci. Technol. A*, 1996, **14**, 46.
90. S. Vepřek, M. Haussmann and L. Shizhi, *Electrochem. Soc. Proc.*, 1996, **96 (5)**, 619.
91. S. Vepřek, P. Neslădek, A. Niederhofer, F. Glatz, M. Jílek and M. Šima, *Surf. Coat. Technol.*, 1998, **108-109**, 138.
92. C. Chen, D. Zhao and X. Wang, *Mater. Chem. Phys.*, 2006, **97**, 156.
93. Y. T. Kim, K. Tadai and T. Mitani, *J. Mater. Chem.*, 2005, **15**, 4914.
94. J. P. Zheng and T. R. Jow, *J. Eletrochem. Soc.*, 1995, **142**, L6.
95. Y. U. Jeong and A. Manthiram, *J. Electrochem. Soc.*, 2002, **149**, A1419.
96. H. Liang, F. Chen, R. Li, L. Wang and Z. Deng, *Electrochim. Acta*, 2004, **49**, 3463.
97. B. Aurian-Blajeni, X. Beebe, R. D. Rauh and T. L. Rose, *Electrochim. Acta*, 1989, **34**, 795.
98. C.-C. Hu, W.-C. Chen and K.-H. Chang, *J. Electrochem. Soc.*, 2004, **151**, A281.
99. J. P. Zheng, *Electrochem. Solid. State*, 1999, **2**, 359.
100. D. Choi, G. E. Blomgren and P. N. Kumta, *Adv. Mater.*, 2006, **18**, 1178.
101. D. Choi and P. N. Kumta, *J. Electrochem. Soc.*, 2006, **153**, A2298.
102. C. Chen, D. Zhao, D. Xu and X. Wang, *Mater. Chem. Phys.*, 2006, **95**, 84.
103. Y. Xiaogang, L. Cun, Y. Baojun, W. Wei and Q. Yitai, *Mater. Res. Bull.*, 2004, **39**, 957.
104. Z. Zude, L. Renmao and Q. Yitai, *Mater. Res. Bull.*, 2002, **37**, 1005.
105. P. Subrammaya, M. S. Hedge, N. Y. Vasathacharya, S. Philip, M. V. Rama-Rao and T. Sripathi, *J. Solid State Chem.*, 1997, **134**, 120.
106. R. Marchand, F. Tessier and F. J. DiSalvo, *J. Mater. Chem.*, 1999, **9**, 297.
107. F. Tessier and R. Marchand, *J. All. and Cmpds.*, 1997, **262-3**, 410.
108. L. E. Toth, *Transition Metal Carbides and Nitrides, Academic Press, New York*, 1971.
109. A. W. Weimer, *Carbides, Nitrides, and Boride Materials Synthesis and Processing. Chapman & Hall, London, 1997*.
110. N. Schonberg, *Acta Chem. Scand.*, 1954, **8**, 204.
111. G. Hägg, *Z. Phys. Chem.*, 1930, **B7**, 339.
112. M. Senna, *Colloids Surf. A*, 1997, **127**, 257.
113. P. Ferrer, J. E. Iglesias and A. Castro, *Chem. Mater.*, 2004, **16**, 1323.
114. J. G. Lisoni, P. Millan, E. Vila, J. L. MartindeVidales, T. Hoffmann and A. Castro, *Chem. Mater.*, 2001, **13**, 2084.

115. J. Xue, D. Wan and J. Wang, *Mater. Lett.*, 1999, **39**, 364.
116. A. Castro, P. Millan, L. Pardo and B. Jimenez, *J. Mater. Chem.*, 1999, **9**, 1313.
117. S. E. Lee, D. M. XueWan and J. Wang, *Acta Mater.*, 1999, **47**, 2633.
118. A. Calka, *Appl. Phys. Lett.*, 1991, **59**, 1568.
119. C. Real, M. A. Roldán, M. D. Alcalá and A. Ortega, *J. Am. Ceram. Soc.*, 2007, **90**, 3085.
120. E. E. M. Sherif, K. Sumiyama, K. Aoki, T. Masumoto and K. Suzuki, *J. Mater. Res.*, 1994, **9**, 2891.
121. Y. Qin, L. Liu and L. Chen, *J. Alloys and Cmpds.*, 1998, **269**, 238.
122. L. W. Yin, M. S. Li, G. Luo, J. L. Sui and J. M. Wang, *Chem. Phys. Lett.*, 2003, **369**, 483.
123. H. Zhang, J. Yu, Y. Chen and J. Fitz Gerald, *J. Amer. Ceram. Soc.*, 2006, **89**, 675.
124. A. Mosbah, A. Calka and D. Wexler, *J. Alloys and Cmpds*, 2006, **424**, 279.
125. C. J. H. Jacobsen, J. Zhu, H. Lindeløv and J. Jiang, *J. Mater. Chem.*, 2002, **12**, 3113.
126. E. G. Gillan and R. B. Kaner, *Chem. Mater*, 1996, **8**, 333.
127. J. C. Fitzmaurice, A. L. Hector and I. P. Parkin, *J. Chem. Soc. Dalton Trans.*, 1993, 2435.
128. A. L. Hector and I. P. Parkin, *Chem. Mater.*, 1995, **7**, 1728.
129. A. L. Hector and I. P. Parkin, *Polyhedron*, 1995, **14**, 913.
130. J. A. Jegier, S. McKernan, A. P. Purdy and W. L. Gladfelter, *Chem. Mater.*, 2000, **12**, 1003.
131. J. W. Hwang, S. A. Hanson, D. Britton, J. F. Evans, K. F. Jensen and W. L. Gladfelter, *Chem. Mater.*, 1990, **2**, 342.
132. J.-W. Hwang, J. P. Campbell, J. Kozubowski, S. A. Hanson, J. F. Evans and W. L. Gladfelter, *Chem. Mater.*, 1995, **7**, 517.
133. J. F. Janik and R. L. Wells, *Chem. Mater.*, 1996, **8**, 2708.
134. K. E. Gonsalves, G. Carlson, S. P. Rangarajan, M. Benaissa and M. J. Jose`-Yacaman, *J. Mater. Chem.*, 1996, **6**, 1451.
135. A. C. Frank, F. Stowasser, H. Sussek, H. Pritzkow, C. R. Ambacher, M. Giersig and R. A. Fischer, *J. Amer. Chem. Soc.*, 1998, **120**, 3512.
136. D. V. Baxter, M. H. Chisholm, G. J. Gama, V. F. Distasi, A. L. Hector and I. P. Parkin, *Chem. Mater.*, 1996, **8**, 1222.
137. G. Demazeau, *J. Mater. Sci.*, 2008, **43**, 2104.
138. R. M. Barrer and E. A. D. White, *J. Chem. Soc. (London)*, 1951, **1267.**
139. I. Kumakiri, T. Yamaguchi and S. Nakao, *Ind. & Eng. Chem. Res.*, 1999, **38**, 4682.
140. R. Roy and O. F. Tuttle, *Phys. and Chem. Earth*, 1956, **1**, 138.

141. M. Takeshi, *Electromagn. Symp. Proc.*, 2004, **16**, 1.
142. K. Byrappa and T. Adschiri, *Prog. Cryst. Growth Charact. Mater.*, 2007, **53**, 117.
143. K. F. E. Schafhautl, *Gelehrte Anzeigen Bayer Akad.*, 1845, **20**, 557.
144. G. Spezia, *Atti. Acad. Sci. (Torino)*, 1898, **33**, 157.
145. Q. Wang, D. Pan, S. Jiang, X. Ji, L. An and B. Jiang, *J. Cryst. Growth*, 2006, **286**, 83.
146. B. Li, Y. Xie, J. Huang, H. Su and Y. Qian, *J. Solid State Chem.*, 1999, **146**, 47.
147. J. Lu, P. Qi, Y. Peng, Z. Meng, Z. Yang, W. Yu and Y. Qian, *Chem. Mater*, 2001, **13**, 2169.
148. F. Caruso, *Colloids & Colloid Assemblies Ed. Wiley, 2004*.
149. L. E. Brus, *J. Chem. Phys.*, 1984, **80**, 4403.
150. W. E. Lynch, D. A. Nivens, B. C. Helmly, M. Richardson and R. R. Williams, *Chem. Edu.* , 2004, **9**, 159.
151. C. B. Murray, D. J. Norris and M. G. Bawendi, *J. Am. Chem. Soc.*, 1993, **115**, 8706.
152. O. I. Mićić, J. Sprague, C. Curtis, K. Jones, J. Machol, A. Nozik, H. Giessen, B. Fluegel, G. Mohs and N. Peyghambarian, *J. Phys. Chem.*, 1995, **99**, 7754.
153. O. I. Mićić, C. J. Curtis, K. M. Jones, J. R. Sprague and A. J. Nozik, *J. Phys. Chem.*, 1994, **98**, 4966.
154. A. Guzelian, J. Katari, A. Kadavanich, U. Banin, K. Hamad, E. Juban, A. Alivisatos, R. Wolters, C. Arnold and J. Heath, *J. Phys. Chem.*, 1996, **100**, 7212.
155. O. I. Mićić, H. Cheong, H. Fu, A. Zunger, J. Sprague, A. Mascarenhas and A. Nozik, *J. Phys. Chem. B*, 1997, **101**, 4904.
156. O. I. Mićić, K. M. Jones, A. Cahill and A. J. Nozik, *J. Phys. Chem. B*, 1998, **102**, 9791.
157. O. I. Mićić, B. B. Smith and A. J. Nozik, *J. Phys. Chem. B*, 2000, **104**, 12149.
158. O. I. Mićić, S. Ahrenkiel and A. J. Nozik, *Appl. Phys. Lett.*, 2001, **78**, 4022.
159. A. Guzelian, U. Banin, A. Kadavanich, X. Peng and A. Alivisatos, *Appl. Phys. Lett.*, 1996, **69**, 1432.
160. U. Banin, C. Lee, A. Guzelian, A. Kadavanich, A. Alivisatos, W. Jaskolski, G. Bryant, A. L. Efros and M. Rosen, *J. Chem. Phys.*, 1998, **109**, 2306.
161. M. Olshavsky, A. Goldstein and A. Alivisatos, *J. Am. Chem. Soc.*, 1990, **112**, 9438.
162. H. Uchida, C. J. Curtis, P. V. Kamat, K. M. Jones and A. J. Nozik, *J. Phys Chem.*, 1992, **96**, 1156.
163. H. Uchida, C. J. Curtis and A. J. Nozik, *J. Phys. Chem.*, 1991, **95**, 5382.
164. K. Brunner, U. Bockelmann, G. Abstreiter, M. Walther, G. Böhm, G. Tränkle and G. Weimann, *Phys. Rev. Lett.*, 1992, **69**, 3216.

165. P. C. Sercel, W. A. Saunders, H. A. Atwater, K. J. Vahala and R. C. Flagan, *Appl. Phys. Lett.*, 1992, **61**, 696.

166. E. K. Byrne, L. Pankanyi and K. H. Theopold, *Science*, 1998, **241**, 332.

167. K. Sardar, M. Dan, B. Schwenzer and C. N. R. Rao, *J. Mater. Chem.*, 2005, **15**, 2175.

# 2.1 Introduction

The following chapter describes the techniques used for synthesis and characterisation of metal nitrides which were produced throughout the study resulting in this thesis. The main techniques used in this work for characterisation of chemical composition and structure were PXD (powder X-ray diffraction), TEM (transmission electron microscopy), SEM (scanning electron microscopy), EDXA (energy dispersive X-ray analysis), IR (infrared spectroscopy), TGA (thermogravimetric analysis), UV-Vis (ultraviolet visible) and DR (diffuse reflectance) spectroscopy and microanalysis.

# 2.2 Synthetic techniques

## 2.2.1 Solvothermal method

Solvothermal methods were used to prepare transition metal nitrides of group 5 (VN, NbN, $Ta_3N_5$) and 6 (CrN, MoN, WN). They were obtained by reacting metal halides ($VCl_3$, $NbCl_5$, $TaCl_5$, $CrCl_3$, $MoCl_5$ and $WCl_4$) with lithium amide or ammonia in benzene. Direct comparisons between the products obtained with these two nitrogen sources were made. GaN and InN were also achieved under solvothermal conditions from $MX_3$ (M = Ga, In; and X = Cl, I) and $LiNH_2$. In this case variations in reagents were also investigated as for example the addition of surfactants such as hexadecylamine (HDA) or N-cetyltrimethylammonium bromide (CTAB), (see Chapter four). A schematic representation of the solvothermal method is shown in Figure 2.1.

All synthesis was performed in a 75 $cm^3$ autoclave (Parr 4740 CH). It can reach a maximum pressure of 420 bar, while the furnace, which contains the autoclave, can be heated up to 550 °C. The reagents were placed in the silica liner in the glove box and covered with benzene. The autoclave was sealed with a graphoil gasket and then heated at various temperatures typically for 24 h. After cooling to room temperature the autoclave was opened inside the glove box. The solid was collected by filtration, washed with an appropriate solvent and dried under vacuum.

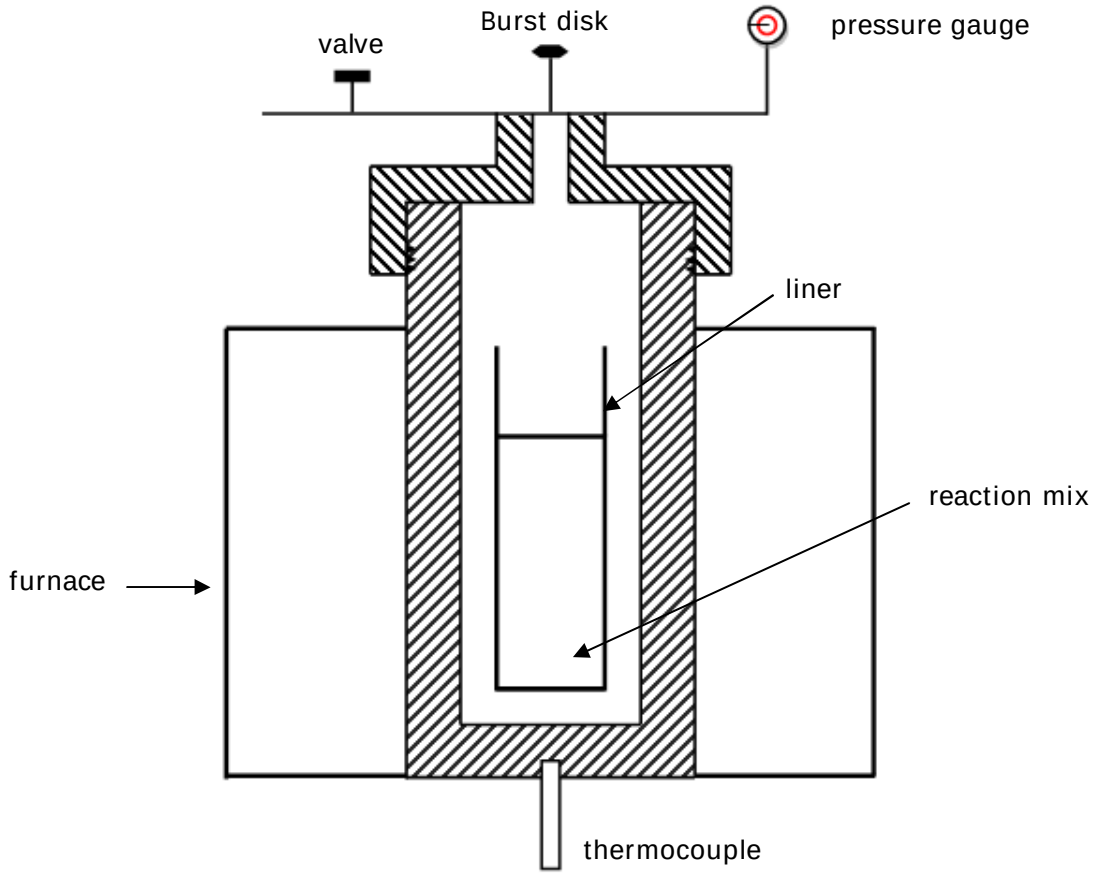


**Figure 2.1** Cross-section of the setup used in a solvothermal experiment.

## 2.2.2 The hot injection technique

This method consists of the injection of precursors into a hot solvent. It leads to a decomposition of the starting materials in contact with the hot solution. The decomposed precursor forms of reactive species which origin the nucleation process. The solvent in these reactions plays a key factor. It must be stable at high temperature and provide the energy required to decompose the initial precursor. This necessary energy is provided by higher thermal collisions reached at high temperature between precursor and solvent. Besides, the solvent can be involved in chemical reactions with the precursor to promote its decomposition. The growth of the species formed must be separated from the nucleation stage in time in order to produce a homogeneous distribution of the nanocrystals produced. Then the addition of a capping agent, usually a surfactant, provides a better control over the size and morphology of the nanocrystals. The capping agent also helps to avoid the aggregation of nanocrystals.

The hot injection technique was employed in this work for the preparation of colloidal GaN nanocrystals. The pyrolysis reactions of a gallium amide were carried out in $N_2$ or $NH_3$ in a mixture of coordinating solvents (trioctylamine, TOA and hexadecylamine, HDA). The reactions of pyrolysis in the precence of only TOA or trioctylphospine TOP were also investigated. A schematic representation of the setup used in these experiments is shown in Figure 2.2.

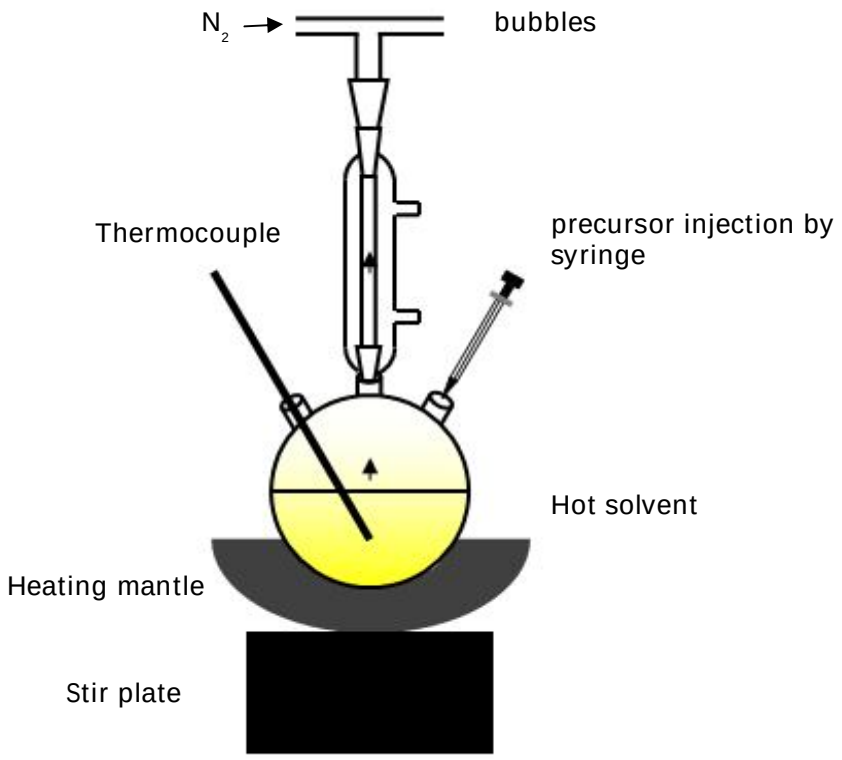


**Figure 2.2** Schematic representation of the setup used to prepare GaN nanocrystals.

# 2.3 Powder X-Ray Diffraction

## 2.3.1 Theory

Crystalline solids have characteristic powder X-ray diffraction patterns (PXD) and hence PXD is one of the most used analytical methods in solid state chemistry.
When a incident beam of X-rays interacts with crystalline matter, all the atoms in the path of the beam will scatter simultaneously. In general the scattered waves cancel each other out in a destructive interference phenomenon; the opposite happens in certain specific directions, the scattered photons undergo constructive interference and an intense beam of photons can be detected, the process is called diffraction (Figure 2.3).

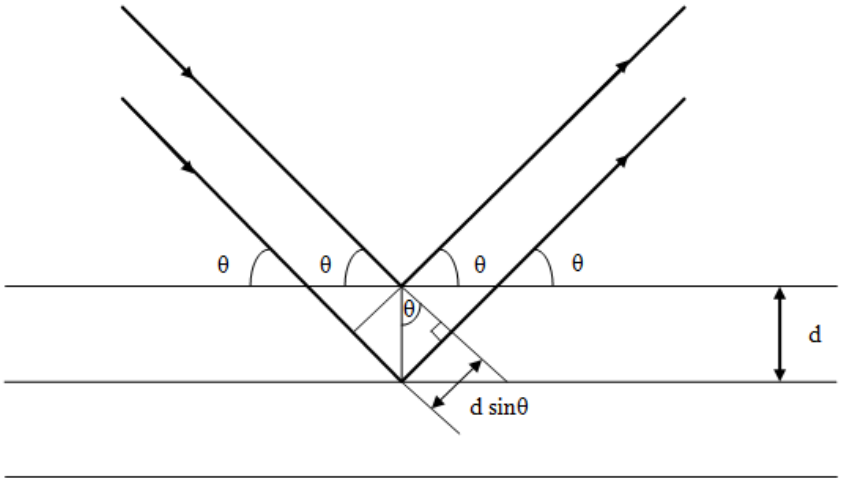


**Figure 2.3** Schematic representation of scattering from parallel planes.

For monochromatic radiation, diffraction can be described using Bragg`s law, which treats the diffraction in simple terms:

$$n\lambda = 2d \sin\theta$$

where $\lambda$ is the X-ray wavelength
n is an integer (1, 2, 3..)
d is the inter-planar separation in the crystalline material
$\theta$ is the angle of incidence (Bragg angle)

By this equation the angle of diffraction, usually measured as $2\theta$, is related to the inter-planar spacing d, and as consequence to the size and shape of a particular unit cell.

The intensities of the diffracted waves will depend on the type and arrangement of atoms in the crystal structure.

### 2.3.2 PXD Instrumentation

The majority of PXD data collection for this study was carried out using a Siemens D5000 diffractometer. X-ray photons for diffraction experiments are produced by bombarding a copper target with a beam of electrons emitted from a heated filament. X-rays of wavelength, $\lambda$ = 1.5406 Å (copper $K_{\alpha_1}$) are selected using a germanium single crystal monochromator. The monochromated beam is collimated by aperture slits and directed onto the sample. The diffracted beam passes through a second set of slits before reaching a NaI scintillating detector (Figure 2.4).

The relative position of incident beam, sample and detector is described as Bragg-Brentano geometry. In order to keep a fixed relationship between the incident angle $\theta$ and the diffraction angle $2\theta$ during the experiment, the sample is rotated at constant angular velocity whereas the detector is rotated at double this velocity. The diffractometer is controlled by a PC and the software collects and stores the diffraction data. The data collected was analysed using the Diffrac Plus Evaluation program (Eva)[1]. Moreover structural analysis of the data was performed using the General Structure Analysis System (GSAS)[2].

Samples were prepared inside a nitrogen filled glovebox and the powder was mounted in an air sensitive sample holder and sealed in order to avoid any oxidation. The sample holder was attached to the diffractometer and data collected over a range of 20-80° ($2\theta$). The phases present were identified by comparison with the JCPDS[3] database using the Eva software package.

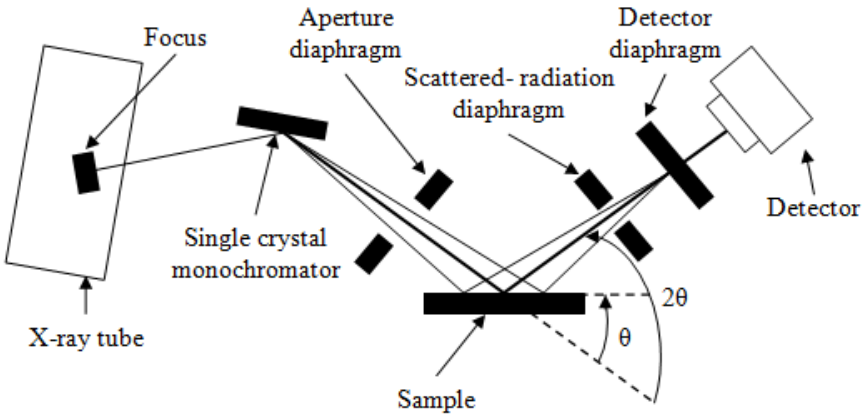


**Figure 2.4** Schematic representation of the D5000 diffractometer.

Some PXD data shown in chapter 6 were collected using a Bruker D8 Discover with General Area Detector Diffraction System (GADDS), also known as C2. The main component and the geometry are the same as for the D5000 instrument except that different types of detector and samples environments can be fitted. The instrument uses Cu Kα radiation (λ= 1.5418 Å). The C2 is also fitted with an XYZ stage and laser video sample alignment system allowing to sample to be accurately positioned in the beam. However multiple samples can be analysed sequentially. In Figure 2.5 is shown the configuration of the diffractometer.

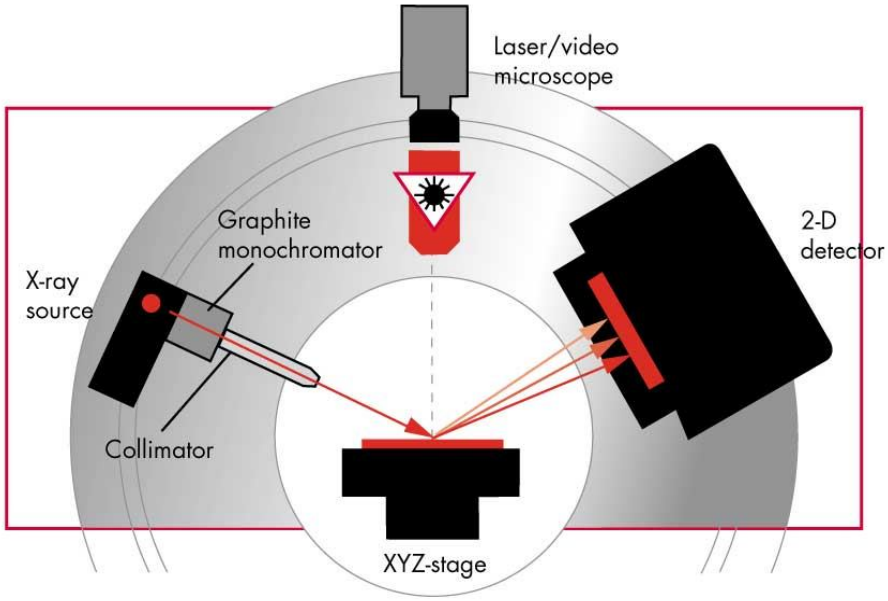


**Figure 2.5** Configuration of the C2 instrument.

This instrument has been used to analyse the crystallinity of GaN produced by colloidal synthesis. Samples prepared in small amount can be better characterised using the C2. This kind of detector facilitates a more rapid collection of data.

### 2.3.3 The Rietveld Method

Powder diffraction data often contains many overlapping peaks and structure factor extraction from the pattern is often difficult and sometimes impossible. In order to increase the amount of the information that could be extracted from powder data, H.M. Rietveld realised that although many reflections did overlap and thus could not be modelled as single entities, the total intensity and the peak shape of a cluster of reflections could be determined by using simple peak shape parameter[4, 5].
Many parameters can be varied while performing a powder data refinement using the Rietveld method. The typical procedure for the refinement of a structural model with PXD data involved:

Determination of an approximate model of the structure by comparison with reference materials.
Refinement of the lattice parameters and zero point.
Refinement of the atom positions in the structure.
Refinement of the isotropic thermal parameters.
Full refinement of peak shape parameters, in addition to any asymmetry or preferred orientation parameters which might be necessary.

Structures were refined to convergence, and all parameters (profile and structural) were refined simultaneously where possible to obtain correct estimated standard deviations on the refined values. The refinement is a least squares best fit process which aims to minimise the function M.

$$M = \sum_k w_i \, (y_i^{obs} - y_i^{calc})^2 \qquad \text{eq 2.3.1}$$

where
$w_i$ a weighting factor given by $1/y_i^{obs}$
$y_i^{obs}$ is the observed intensity
$y_i^{calc}$ is the calculated intensity

The calculate profile derived, $y_i^{calc}$, is determined from the structural model adding together the calculated contributions from neighbouring Bragg reflections (k) and the background $b_i$ :

$$y_i^{calc} = s \sum_i L_k \; |F_k|^2 \, \Phi(2\theta_i - 2\theta_k) \, P_k \, A + y_{bi} \qquad \text{eq. 2.3.2}$$

where
$s$ is the scale factor
$L_k$ contains Lorentz, polarisation and multiplicity factors

$\Phi$ is the reflection profile function

$F_k$ is the structure factor for the $k^{th}$ Bragg reflection

$P_k$ is the preferred orientation function

A is an absorption factor

$y_{bi}$ is the background intensity at the $i^{th}$ step

A comparison of intensities is performed at every point, consequently it is essential to accurately describe the peak shape in the calculated profile. The peak shape of the D5000 diffractometer is pseudo-Voigt made by Lorentzian and Gaussian contributions. The Gaussian (G) and Lorentzian (L) contributions to the peak shape are described by the equations:

$$G = \frac{(4\ln 2)^{1/2}}{H_k\sqrt{\pi}} \exp\left[\frac{-4\ln 2(2\theta_i - 2\theta_k)^2}{H_k^2}\right] \qquad \text{eq. 2.3.3}$$

and

$$L = \frac{2}{\pi H_k} \Big/ \left[1 + 4\,\frac{(2\theta_i - 2\theta_k)^2}{H_k^2}\right] \qquad \text{eq. 2.3.4}$$

Where $2\theta_k$ is the calculated position for the $k^{th}$ Bragg reflections corrected for the counter zero point,

$H_k$ is the full-width-at-half-maximum (FWHM) of the $k^{th}$ Bragg reflection.

In order to make a quantitative assessment of the agreement between the observed and calculated profile a number of reliability factors are defined.

$$R_{profile} = R_p = 100\left[\frac{\sum_i |y_i^{obs} - y_i^{calc}|}{\sum_i y_i^{obs}}\right] \qquad \text{eq. 2.3.5}$$

$$R_{expected} = R_{exp} = 100\left[\frac{(N - P + C)^2}{\sum_i w_i\,(y_i^{obs})^2}\right]^{\frac{1}{2}} \qquad \text{eq. 2.3.6}$$

where $R_{exp}$ is defined from the statistics of the refinement

N is the number of observations

P is the number of refineable parameters

C is the number of constraints

From a mathematical view point, $R_{weighted\ profile}$ ($R_{wp}$) is the most significant of the R factors. This is so because the numerator is the residual being minimised. For identical reasoning it is the factor that best reflects the progress of a refinement and is given by:

$$R_{wp} = 100 \left[\frac{\sum_i (y_i^{obs} - y_i^{calc})^2}{\sum_i w_i (y_i^{obs})^2}\right]^{\frac{1}{2}} \quad \text{eq. 2.3.7}$$

Another parameter minimised during the refinement is chi-squared defined by:

$$\chi^2 = \left[\frac{R_{wp}}{R_{exp}}\right]^2 \quad \text{eq. 2.3.8}$$

For a good fit, the $R_{wp}$ should approach the statistically expected $R_{exp}$. The goodness of fit can be observed by examining a plot of the profile fit. The difference between calculated and observed patterns should be as flat as possible for a good fit.

### 2.3.4 Particle size estimation from GSAS Refinement

Particle size can be related to peak shape for a diffraction pattern. Information on particle size can be extrapolated from the complex expressions derived to model the Gaussian (mainly instrumental broadening) and Lorentzian (mainly sample-related broadening) of the peak shape. For PXD the particle size broadening can be obtained from the expression:

$$\frac{\Delta d}{d^2} = \frac{\Delta 2\theta\ cot\theta}{d} = \text{constant} \quad \text{eq. 2.3.9}$$

From Bragg`s law this becomes:

$$\frac{\Delta d}{d^2} = \frac{2\Delta 2\theta \cot\theta \sin\theta}{\lambda} \quad \text{eq. 2.3.10}$$

The broadening is then:

$$\Delta 2\theta = \frac{\lambda \Delta d / d}{2 \cos\theta} \quad \text{eq. 2.3.11}$$

For PXD the Lorentzian coefficient, $\gamma$, of the peak shape is composed of two functions, X (particle size) and Y (strain), (denoted LX and LY in the GSAS program) in the expression[6]:

$$\gamma = \frac{X + X_s \cos\Phi}{\cos\theta} + (Y + Y_e \cos\Phi)\tan\theta \qquad \text{eq. 2.3.12}$$

where: $X_s$ and $Y_e$ are anisotropic coefficients.

The first term in the expression for the Lorentzian broadening, X, is of the form:

$$X = \frac{\Delta d}{d^2} \qquad \text{eq. 2.3.13}$$

Rearranging this expression and converting from centideg to radians gives the particle size, p:

$$p = \frac{1800K\lambda}{\pi X} \qquad \text{eq. 2.3.14}$$

where K is the Scherrer constant, $\lambda$ is the X-ray wavelength (1.54 Å) and X is the value of the Lorentzian component extracted from GSAS refinement.

The equation 2.3.14 has been used to calculate the particle size of all materials prepared in this work. In order to increase the signal:noise ratio of the diffraction pattern a wider slit (1 mm) was placed before the detector (Fig. 2.4). In fact most of the products obtained had low crystallinity, due to the gentle conditions used in these reactions. In particular this approach was very useful in the case of the preparation of gallium nitrides (discussed in chapter 4). The Gaussian components of the peak shape, e.g. the diffractometer contributions, were obtained by refining an $\alpha$-quartz ($SiO_2$) standard. This material was selected primarily because of its availability in pure form and also because the crystal structure is well characterized. Only Lx and Ly were then refined for samples.

# 2.4 Electron Microscopy

Electron Microscopy has been used to provide information regarding the shape and size of particles including their size distribution and the degree of aggregation.

## 2.4.1 Transmission Electron Microscopy

Transmission electron microscopy (TEM) is one of the most important tools for characterizing nanoscale materials, it can help to confirm information from other techniques such as PXD, and has the advantage of requiring only small amounts of sample.
Samples were prepared by ultrasound dispersal in toluene, followed by deposition on carbon-coated Cu grids, using a Pasteur pipette. The technique was used to obtain visual information on the nanocrystalline materials produced throughout the research, approximate particle size and also to utilise electron diffraction to obtain structural information. TEM was carried out with a Hitachi 7000 (75 KV), microscope at the Biomedical Imaging Unit, Southampton General Hospital.

### 2.4.1.1 TEM Instrumentation

The main parts of a TEM are assembled into a vertical column. At the top of the instrument is the electron gun[7]. TEM usually uses thermionic guns capable of accelerating the electrons in the range 40-300 KV. The right electron energy depends upon the nature of the specimen and the information required. The use of higher electron energies represents an advantage in case of thick samples or high resolution requirements. The illumination provided by an electron gun is focussed onto the specimen by two condenser lenses (Figure 2.6). One of the most important parts of the microscope is the specimen chamber which is placed below the second condenser lens C2. The specimen rod enters the column through an airlock, and can usually be moved in the x, y and z directions to find the region of interest.

The TEM can provide two separate kinds of information about a specimen- a diffraction pattern and a magnified image. In the case of powders, the specimens contain several crystals of different orientations and the final diffraction pattern is the sum of each individual pattern. All the electrons diffracted at a particular angle ($2\theta$) by the crystal planes are measured at a point distant r from the undiffracted beam. The electrons diffracted at different angles result in the formation of several spots distributed in

rings of different r. Meanwhile all the electrons emitted from a point contribute to the formation of an image.

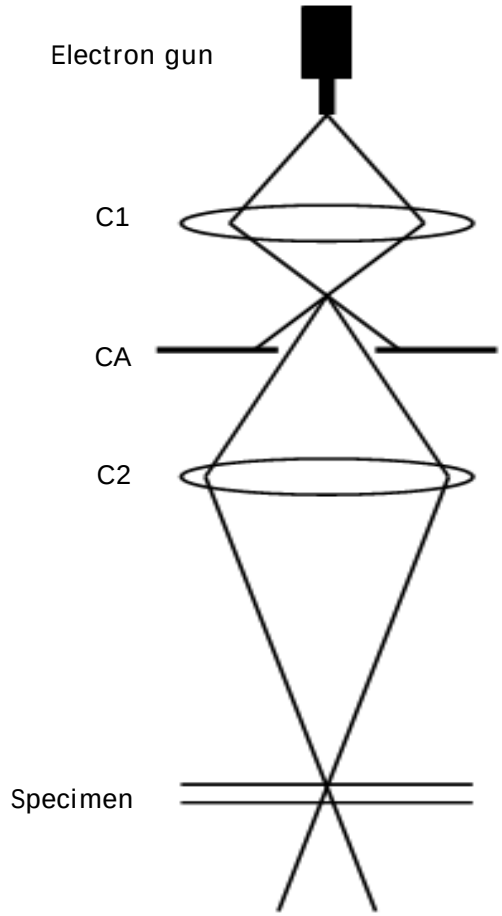


**Figure 2.6** Main components of a transmission electron microscope (C1 and C2 are the condenser lens while CA is the condenser aperture).

## 2.4.2 Scanning Electron Microscopy

The scanning electron microscope (SEM) is similar to the transmission electron microscope (TEM) in that they both employ a beam of electrons directed at the specimen. Electron gun, condenser lenses and vacuum system are similar in both instruments. TEM provides information about the internal structure of thin specimens whereas SEM is usually used to study the surface, or near surface, structure of bulk specimens.

Scanning electron microscopy was performed using a Jeol 5910 scanning electron microscope. The main components of a SEM are shown in Figure. 2.7. The microscope consists of an electron gun that generates an electron beam via thermionic emission from a heated tungsten filament. The electrons are accelerated to an energy which is

usually between 1 KeV and 30 KeV which is lower than the energy typical of the TEM (40-300 KeV). The tungsten acts as the cathode and the electrons emitted from the filament are accelerated towards the anode producing a beam of high energy electrons. In this way the electrons are free to travel into an evacuated column. It must be evacuated to avoid the scattering of electrons by gas molecules.

The electron beam travels down the SEM and before hitting the sample is demagnified by two electromagnetic condenser lenses. This controls the convergence angle and diameter (2-10 nm). Below the condenser lenses lie four or five electromagnetic objective lenses. These lenses form the first intermediate image and diffraction pattern, which can be enlarged by the subsequent projector lenses and then displayed on screen. These projection lenses determine the overall magnification of the final image. Scan coils are used to scan the beam across the sample and a scintillator-photomultiplier system was employed as a detector to count the number of low energy secondary electrons or other radiation emitted from each region of the sample.

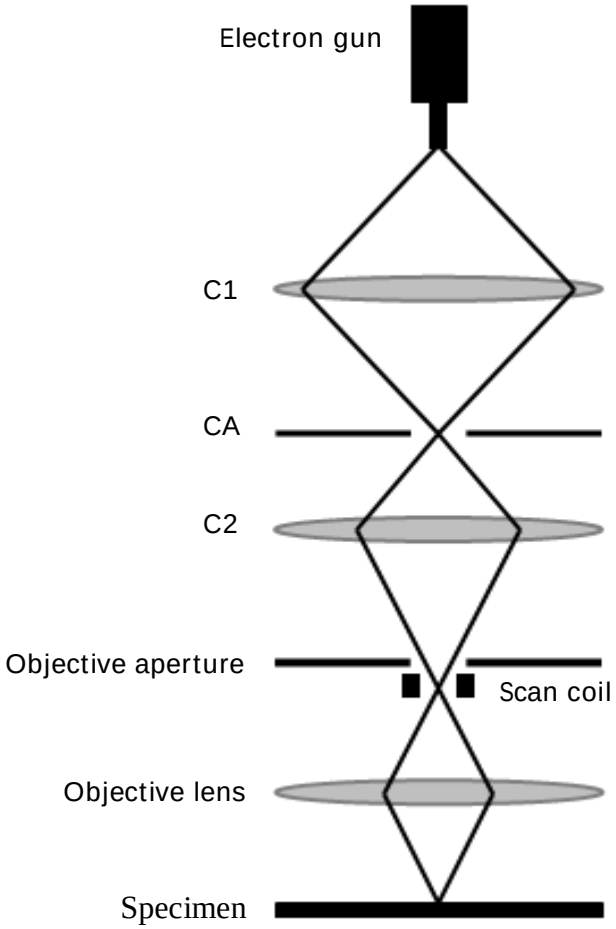


**Figure 2.7** Main components of a scanning electron microscope. (C1 and C2 are the condenser lens while CA is the condenser aperture).

### 2.4.3 Energy Dispersive X-ray analysis

Energy dispersive X-ray analysis (EDXA) is an analytical technique used to identify the elemental composition of a specimen. This technique is used in conjunction with SEM and TEM instruments where the image capability of the microscope is used to select the region of interest.

When the electron beam impinges on the sample surface an electron in an inner shell of one of the constituent atoms may be excited by the incident beam. Ejection from its shell creates an electron hole and an electron from an outer, higher energy shell will fill that hole. The difference in energy between the higher -energy shell and the lower one is released in the form of an X-ray photon. The energy of these photons is measured in the EDX detector. Since these energies are characteristic of the atomic structure of the element from which they were emitted, the elemental composition of the sample can be analysed.
EDX has a typical penetration depth of around 1-2 μm. A lithium drifted silicon (SiLi) detector is used in EDX and operated at liquid nitrogen temperature. The X-ray photon strikes the detector and will generate a photoelectron within the body of the Si. Electron-hole pairs are generated through the photoelectron travelling through the Si and are attracted to opposite ends of the detector with the aid of a strong electric field. Hence a current pulse is generated and its size depends on the number of electron-hole pairs created, which in turn depends on the energy of the incoming X-ray photon.

The SiLi detector was protected by a boron nitride window so N was difficult to detect and any nitrogen contained within the samples was rendered invisible. Furthermore, the ability to quantify the presence of any carbon in the sample itself is also removed since carbon coating is required to enhance the conductivity of the sample under examination prior to analysis so that the surface does not charge in the electron beam.

## 2.5 Infrared Spectroscopy

Infrared (IR) spectroscopy was performed using a PerkinElmer Spectrum One FT-IR spectrometer in conjunction with PerkinElmer's analytical software Spectrum v3.05.

Infrared spectroscopy is one of the most common spectroscopy techniques. It is used to determine groups in the sample. IR radiation does not have enough energy to induce electron transition as in UV spectroscopy. Absorption of IR is restricted to compounds with small energy differences in the possible vibrational and rotational states.

For a molecule to adsorb IR, the vibrations or rotations within a molecule must cause a net change in the dipole of the molecule. The infra-red region is usually divided into sections: near (14000-4000 $cm^{-1}$), middle (4000-400 $cm^{-1}$) and far (400-10 $cm^{-1}$). Different types of bonds, and thus different groups, adsorb infrared radiation of different wavelengths. These wavelengths appear as a series of peaks and are referenced by comparison with tables of known compounds.

Solid samples were prepared by incorporating them into a pressed pellet of cesium iodide for analysis. Due to the sensitivity of the precursor, the samples had to be prepared inside a nitrogen filled glovebox. A weighed portion of sample, approximately 3 mg, was mixed with 300 mg, of highly purified CsI using a pestle and mortar. The sample and CsI were ground well to reduce the particle size; otherwise the large particles would scatter the infrared beam causing a sloping profile in the baseline of the spectrum. Cesium iodide does not absorb in the region studied so will not interfere with the spectrum. The mixture was placed in an evacuable die and subjected to a pressure of 10 MPa for two minutes. Then the sample was placed between CsI disks in an IR cell with a Teflon spacer to protect it air whilst the data were collected.

# 2.6 Ultraviolet-visible Spectroscopy

Optical properties of the materials prepared in this work were investigated through ulteaviolet visible (UV-Vis) absorption and diffuse reflectance spectroscopy. The experimental data were recorded in the visible range (380-780 nm) using a Perkin Elmer UV-Vis Lambda 35 Spectrometer.

The instrument contains two different radiation sources. A halogen lamp is used to cover the visible region, whereas a deuterium lamp is used for the ultraviolet region. These two lamps are alternately blocked. The other components are a monochromator and a series of mirrors within the instrument that allow the radiation to be aligned on the sample. After interaction with the sample the radiation passes through a convex lens onto a photodiode detector.

In most nitride materials studied in this work, the absorption spectrum was difficult to obtain. The particle size of the samples was often not small enough and their precipitation was often the outcome. Moreover the samples prepared were often black in colour due to the presence of carbon. The radiation was completely absorbed from the solution and was not possible obtain information about the absorption spectrum. When the products were of terracotta colour (e.g. $Ta_3N_5$) diffuse reflectance spectroscopy showed semiconducting properties. $Ta_3N_5$ samples were mounted in an

aluminium holder with a quartz window. Barium sulphate block was used as a reference to obtain a background correction. The bad gaps were calculated from the maximum of the first derivative of the absorption edges.

## 2.7 Thermogravimetric Analysis

Thermogravimetric analysis (TGA) is a thermal analysis technique used to measure changes in the mass of a sample as a function of temperature and/or time. It was used to measure the thermal stability and the compositions of materials. TGA was performed using a Mettler Toledo `TGA 851e` thermogravimetric analyser. The equipment was mounted inside a nitrogen atmosphere glove box, due to the highly air-sensitive nature of the samples. Samples were loaded into a dry alumina crucible and then placed onto the balance arm within the analyser.

The sample was gradually heated to 900 °C at a heating rate of 10 °/minute under a flow of high purity nitrogen gas (50 mL/min.) for the whole procedure. At 900 °C the sample was then held for 20 minutes before allowing it to cool back to 25 °C. The balance assembly measures the initial sample weight and then continuously monitors any change in weight, either losses or gains, as a function of temperature and time.

Oxygen gas was also used as a reactive gas in order to oxidise the sample, this enables the metal content to be quantified by measuring the amount of oxidation that occurred when the sample was heated to temperatures of 900 °C.

Whilst TGA was able to ascertain the metal content of any of the precursors analysed it was limited in offering any other quantitative information. A mass spectrometer connected to the TGA would enable the analysis and characterisation of the volatilised fragments released from the sample during pyrolysis.

# 2.8 Microanalysis

Microanalysis was performed by Medac Ltd, Egham, Surrey. Precursor materials and annealed nitrides were sent for analysis; information on the quantities of carbon, hydrogen, nitrogen and chloride were collected. C, H and N contents were analysed by combustion. Samples were loaded into the tin capsules with a $WO_3$ oxidising agent and flush combusted in an oxygen atmosphere in an argon filled glove box. Gaseous products were analysed on one of several analysers.
Chlorine content was analysed by means of Schöniger flask combustion followed by titration or ion chromatography.

This information was used to establish carbon content within the analytes and the nitrogen content of each sample could be used as a guide to its stoichiometry compared to calculated percentages from “ideal” materials.

Microanalysis was used to compare the C, H and N concentration of the precursors thermolysed under ammonia or nitrogen as well as the annealed product of the various different precursors produced via the preliminary work undertaken for the investigation of nanocrystalline.

# 2.9 References

1. *Eva, V10.1, Bruker Advanced X-Ray Solutions*, 2004.
2. A. C. Larson and R. B. Von-Dreele, *GSAS Manual, LANSCE MS-H805, Los Alamos National Laboratory, Los Alamos NM, NM 87545, 2000*.
3. *International Centre for Diffraction Data, 12 Campus Boulevard, Newton Square, Pennsylvania 19073-3273, U.S.A.*
4. H. M. Rietveld, *Acta Cryst.*, 1967, **22**, 151.
5. H. M. Rietveld, *J. Appl. Cryst.*, 1969, **2**, 65.
6. A. C. Larson and R. B. Von-Dreele, *General Structure Analysis System (GSAS), Los Alamos National Laboratory Report LAUR*, 2004, **86-748.**
7. P. J. Goodhew, J. H. Humphreys and R. Beanland, *Electron Microscopy and Analysis*, 2001, **3rd Ed.**

# 3.1 Introduction

Gallium and indium nitrides are important optoelectronic materials with band gaps ranging from 0.7 eV in InN to 3.4 eV in GaN. Gallium nitride is especially relevant as, with the introduction of suitable dopants or in solid solution with InN, its band gap can be varied to emit light from the UV to the IR region. When used in electronic devices, these nitrides are typically produced using MOVPE (Metal-Organic Vapour Phase Epitaxy) or MOCVD (Metal Organic Chemical Vapour Deposition) techniques[1-5]. They have also been prepared in powdered form by high-temperature ammonolysis[6-8] or metal amide decomposition[9, 10], and as nanoparticle colloids by decomposition of molecular precursors in hot solvents[11].

As discussed in the introduction, the preparation of GaN films is typically achieved by MOCVD from $Ga(CH_3)_3$ and $Ga(C_2H_5)_3$ in ammonia[12] using sapphire as substrates. The resulting films contain large number of defects because of the large mismatch and difference of the thermal expansion coefficient between GaN and substrate. Although silicon carbide (SiC) has similar lattice parameter to GaN and it is a good substrate its use is limited because of the formation of $SiN_x$ at the interface[8]. An important route to reduce the defects in the GaN films is the use of GaN single crystals as substrate on which GaN films can be deposited. The major challenges associated with growing single crystals are due to the fact that traditional method like melt growth cannot be used because of high melting point of GaN (~2900 K) and high decomposition $N_2$ pressure. Only few routes are available and one of the most important is the solvothermal growth using ammonothermal conditions. GaN single crystals up to 0.5 mm were grown in supercritical ammonia at 400 ºC and 2.4 Kbars[13]. The quality of GaN crystals was found to vary depending on the choice of mineralizes. The use of $KNH_2$ and KI as mineralizer has been successful for the preparation of GaN single crystals in supercritical ammonia[13].

While the preparation of group III nitrides in single crystal form is often difficult, their preparation as powders is relatively easy. Solvothermal synthesis is gradually developing into a useful technique to produce metal nitrides in nanocrystalline form, including anisotropic particles[14, 15]. Typically the reagents are those that have previously been used in solid state metathesis, especially metal chlorides and $Li_3N$ or $NaN_3$[16-22]. Nanocrystalline GaN has been produced from $Li_3N$ and $GaCl_3$ in benzene at 280 ºC as nanocrystals of ~ 30 nm diameter[23]. Under these conditions a mixture of hexagonal and rocksalt-type GaN was produced. This was surprising as rocksalt-type GaN is normally only found at high pressure[24]. $GaCl_3$ and $NaN_3$ react in toluene or THF at 260 ºC, producing a poorly crystalline product[25], but on annealing to 750 ºC hexagonal GaN

crystals of ~ 8 nm size were produced. Hexagonal GaN with diameter of ~ 4-15 nm has also been prepared using solvothermal reactions between Ga cupferron [$(Ga(C_6H_5N_2O_3)_3]$ or $GaCl_3$ and $(Me_3Si)_2NH$ in toluene at ~240 ºC. In this work[26] the authors also added a surfactant (*N*-cetyltrimethylammonium bromide) and obtained capped nanoparticles of ~ 2.5 nm in diameter. Solvothermal synthesis of InN has been achieved *via* reactions of $InCl_3$ with $Li_3N$ in xylene[27] or of $InI_3$ with $NaNH_2$ in benzene[28], both at around 250 ºC. Another report showed the reactions between $InBr_3$ and $NaN_3$ in toluene or hexadecane at ~280 ºC to produce 10 nm hexagonal InN crystallites, with some evidence of cubic InN at lower temperature[29].

The main aim of this work was the preparation of GaN and InN nanocrystals from gallium and indium halides with lithium amide under solvothermal conditions. Compared with solid state routes these conditions are relatively gentle due to the lower temperatures as the heat produced during the reactions can be absorbed by the solvent. As a consequence a better control of the growth of small crystallites can be achieved. However solvothermal reactions can be employed to form metastable phases that cannot be prepared by solid-state reactions (e.g. zinc-blende GaN). The successful preparation of GaN from $[Ga(NMe_2)_3]_2$ and $NH_3$[11] suggested that the use of amide precursors could be an alternative solvothermal route to the preparation of GaN and InN. $LiNH_2$ is a stable solid at room temperature and should deliver milder reaction conditions than for example $NaN_3$, which is thermally unstable, shock sensitive and potentially explosive[30].
Another key factor in the solvothermal reactions was the choice of solvent. All the reactions in this study were carried out in benzene. Despite its toxicity it was the preferred solvent because previous work in the group showed that benzene underwent less decomposition under solvothermal conditions than mesytilene. The effect of the addition of surfactants to solvothermal preparations of GaN and InN was also investigated.

## 3.2 Reactions of $GaCl_3$ with $LiNH_2$

The preparation of nanocrystalline GaN was carried out from the reaction of $GaCl_3$ with $LiNH_2$ in benzene. The reactants were weighed out in the glove box in a nitrogen atmosphere and dissolved in a silica liner using benzene. The autoclave was then sealed and heated typically for 24 h. After reaction it was cooled to room temperature and depressurised to remove the ammonia produced. The solid was then washed with methanol and filtered to remove LiCl from the final product. The solvothermal route to GaN nanocrystals in benzene using $LiNH_2$ as the nitrogen source was envisaged to proceed as follows:

$$GaCl_3 + 3\ LiNH_2 \xrightarrow{\text{benzene}} GaN + 3\ LiCl + 2\ NH_3$$

At 250 ºC zinc blende-type (cubic) GaN was obtained, whereas at higher temperatures a mixture of the zinc blende and the wurtzite-type (hexagonal) phases formed (Fig. 3.1). Broads peaks were observed because of the formation of small crystallites. Reflections at 2θ =33º, 35º, 37º, 48º, 58º, 64º and 70º are assigned to the (100), (002), (101), (102), (110), (103) and (112) planes of wurtzite (hexagonal) GaN. While at 250 °C reflections at 2θ = 35.5°, 58 ° and 69° of the (111), (220) and (311) planes are characteristic of zinc blende (cubic) GaN. The 200 peak at 2θ ~ 40 ° is not directly observed on the pattern recorded at 250 °C. Nevertheless its presence is reflected in the asymmetry of the 111 peak.

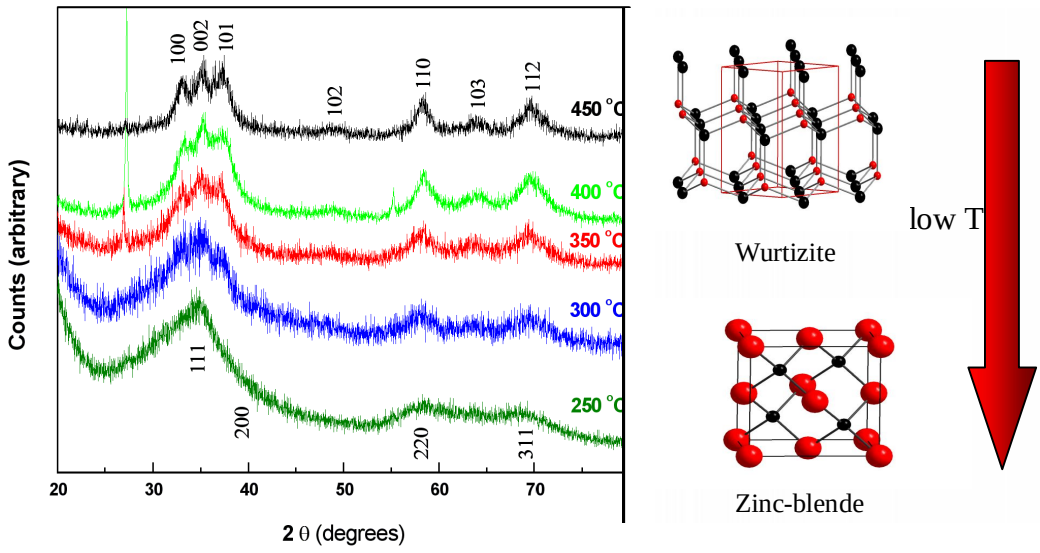


**Figure 3.1** XRD patterns of GaN produced from $GaCl_3$ and $LiNH_2$ at different temperatures. Reflection positions for wurtzite type GaN (hexagonal $P6_3mc$) are marked

over the pattern of GaN prepared at 450 ºC and those of zinc-blende type GaN (cubic F-43m) over the pattern of GaN achieved at 250 ºC.

The feature below 25º (2θ) in the patterns collected from samples made at 250-350 ºC was due to some amorphous content, whereas the peak at 26º showed in the XRD patterns of the sample prepared at 350 and 400 ºC is due to carbon from the bomb gasket. This issue was solved by placing a cap on the silica liner to collect the carbon produced by the degradation of the gasket. X-ray diffraction patterns recorded after this adjustment did not show the peak at 26° (2θ).

Gallium nitride with particles sizes ranging from 1.8 to 6 nm were prepared at temperatures in the range 250-450 ºC. Poor Rietveld fits were obtained to all the PXD patterns analysed. This was due to the amorphous content of the materials which leads to a poor background and to broad overlapping peaks. An improvement in the signal:noise ratio of the diffraction patterns was achieved by placing a wider slit (1mm compared with the usual 0.2 mm) before the detector in the D5000 diffractometer. In this way better defined peaks were observed but Rietveld analysis was still not possible.

The reflections 100 and 101 at 2θ = 33º and 37º respectively are characteristic of wurtzite type GaN and were used to calculate the lattice parameters listed in table 3.1. The 220 reflection in the cubic phase does not overlap with other peaks and was used to calculate a lattice parameter of a = 4.46 Å and an average crystallite size of 1.8 nm at 250 ºC. Literature reports of the lattice parameters of GaN range from 4.36-4.47 Å[31, 32].

Combustion analysis revealed nitrogen-deficient GaN samples with significant carbon and hydrogen content (Table 3.1). A significant amount of chlorine (4.7 %) was found in the sample prepared at 250 °C while EDX analysis made on the other samples did not show chlorine content.

**Table 3.1** Analysis of the products from the reactions of $GaCl_3$ and $LiNH_2$. ($N_{teor}$ = 16.7 %).

| T(°C) | Lattice parameters (Å) | Composition | % C | % N | % H |
|---|---|---|---|---|---|
| 450 | a = 3.137, b = 3.137 c = 5.199 | $GaN_{0.69}C_{0.16}$ | 2.4 | 11.9 | 0.8 |
| 400 | a = 3.119, b = 3.119 c = 5.193 | $GaN_{0.68}C_{0.26}$ | 3.9 | 11.5 | 1.1 |
| 350 | a = 3.103, b = 3.103 c = 5.345 | $GaN_{0.69}C_{0.20}$ | 2.9 | 11.8 | 1.3 |
| 300 | a= 4.49 | $GaN_{0.70}C_{0.13}$ | 2.0 | 12.1 | 1.6 |
| 250 | a = 4.46 | $GaN_{0.70}C_{0.36}$ | 5.1 | 11.7 | 2.1 |

The IR spectra, (Fig. 3.2), show a broad Ga-N stretch around 600 $cm^{-1}$, significant $\nu$(N-H) and weak $\nu$(C-H) bands[33]. The mechanism of GaN formation most likely involves metathesis reactions that produce Ga-$NH_2$ groups that then condense with neighbouring Ga centres. Hence the presence of residual NH groups in the products at these relatively mild temperatures is not surprising. The decomposition of solvent to produce carbon is less expected.

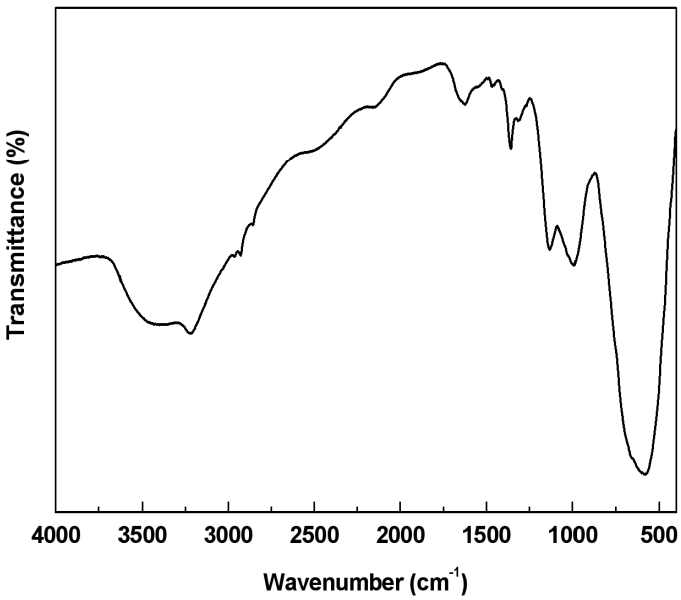


**Figure 3.2**. IR spectrum of GaN produced from $GaCl_3$ and $LiNH_2$ at 400 ºC.

TEM, (Fig.3.3), showed regular-shaped crystallites with particle sizes below 5 nm broadly consistent with the size estimated from the PXD data. All of the samples studied had significant aggregation of these crystallites.

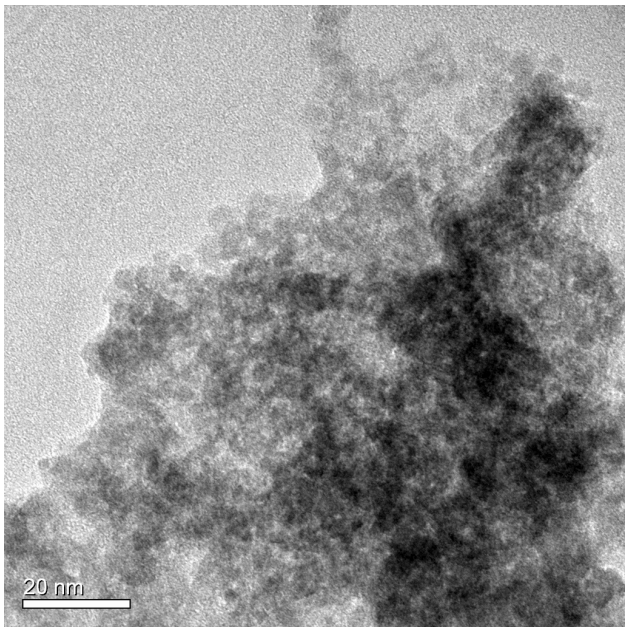


**Figure 3.3** TEM image of GaN prepared from $GaCl_3$ and $LiNH_2$ in benzene at 300 °C.

## 3.3 Reactions between $GaCl_3$ and $LiNH_2$ in the presence of hexadecylamine

The use of surfactants to control the particle size and prevent the agglomeration of nanoparticles is common, and there is one reported example of the production of capped GaN nanocrystals under solvothermal conditions by adding CTAB (N-cetyltrimethylammonium bromide)[26]. Hence reactions analogous to those described in the previous section were tried with added hexadecylamine. Various amounts of HDA were added to reactions between $GaCl_3$ and $LiNH_2$ in benzene at 250 ºC in an attempt to produce capped particles. PXD data identified all of the products as cubic GaN (Fig. 3.4).

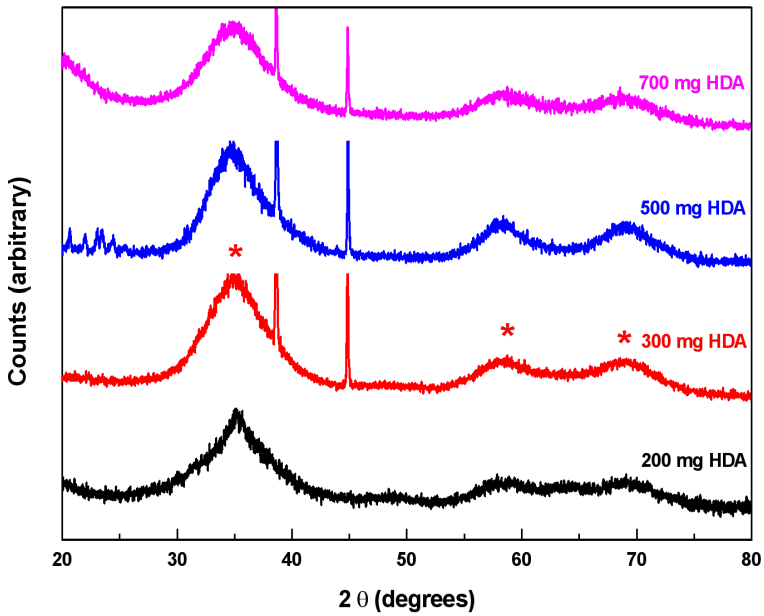


**Figure 3.4**. XRD patterns of GaN prepared from $GaCl_3$ and $LiNH_2$ at 250 °C with different added amounts of HDA. The 111, 220 and 311 GaN reflections are marked by asterisks. Two aluminium peaks resulting from the sample holder are visible in some data sets at 38 and 44°.

The addition of small amounts of HDA led to a small increase in the crystallite size and a reduction in the amorphous content of the samples. When 300 or 500 mg HDA were added, the PXD patterns (Fig. 3.4) showed a remarkable reduction in the amorphous scattering compared with samples made at the same temperature without HDA (Fig. 3.1) Addition of further HDA, however, resulted in the reappearance of amorphous features in the diffraction patterns and further broadening of the reflections. This change suggests that HDA becomes involved in the formation of GaN, possibly reacting more readily with the $GaCl_3$ in solution prior to heating than does the solid $LiNH_2$. Metal primary amides can self condense to produce bridging imide groups. A similar behaviour of primary amides was found in sol gel preparation of TiN[34, 35]. The formation of GaN is believed to proceed as follows:

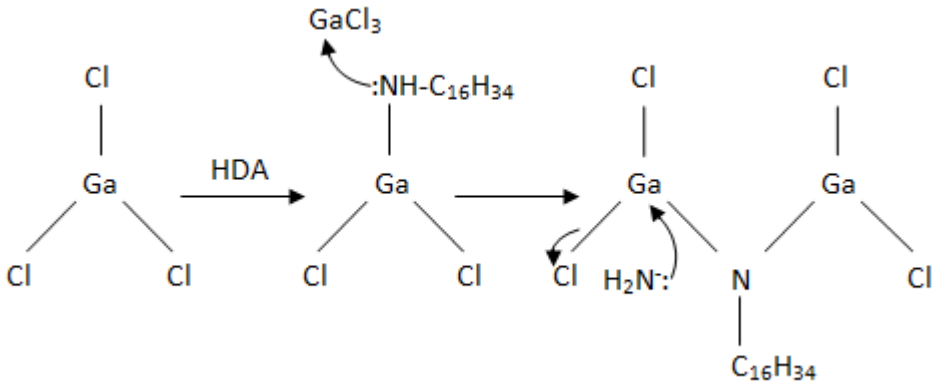


HDA has an electron rich donating group ($NH_2$) which coordinates to the Ga metal. The first step of the reaction is the replacement of Cl with $NHC_{16}H_{34}$ group. These groups can condense with other gallium centres forming Ga-$NC_{16}H_{34}$Ga cross-linkages. Anion $NH_2^-$ from lithium amide react also with gallium helping in the substitution of any remaining chlorine groups again with the possibility of condensation of the Ga-$NH_2$ groups to Ga-NH-Ga. The carbon and hydrogen content in the final product may be due to the presence of bound HDA.

The lattice parameters of these samples are a little higher than those of samples produced without HDA (Tables 3.2 and 3.1) and also slightly higher than the normal range of literature values. Carbon incorporation into nitride structures typically results in an increase in the lattice parameter[36]. Carbon incorporation directly into the GaN structure along with the presence of bound HDA molecules is also consistent with the microanalysis results, (Table 3.2), that show low nitrogen contents (GaN contains 16.7 % N) in these samples. The C, H and N contents all increase as more HDA is added to the reactions, showing that it is carried through to the products.

**Table 3.2**. Products identified from the reactions of $GaCl_3$ and $LiNH_2$ with added HDA. Combustion analyses are accurate to ± 0.3 %.

| Composition | HDA (mg) | % C | % N | % H | Crystallite size, nm | a (Å) |
|---|---|---|---|---|---|---|
| $GaN_{0.17}C_{0.93}$ | 200 | 13.4 | 2.9 | 3.4 | 2.0 | 4.48 |
| $GaN_{0.27}C_{1.25}$ | 300 | 16.9 | 4.3 | 3.9 | 2.0 | 4.46 |
| $GaN_{0.50}C_{2.00}$ | 500 | 23.8 | 7.0 | 4.8 | 1.8 | 4.48 |
| $GaN_{0.76}C_{2.73}$ | 700 | 28.9 | 9.5 | 5.4 | 1.8 | 4.48 |

Evidence of N-H groups was visible in the IR spectra ( Fig 3.5). A broad band $\nu$(N-H) at 3450 $cm^{-1}$ was assigned to the N-H stretching, characteristic of primary amide in condensed phase. Significant sharp $\nu$(C-H) and also broad bands in the $\nu$(Ga-N) region[37] around 600 $cm^{-1}$ were also recorded, consistent with the organic content inferred from the analysis data.

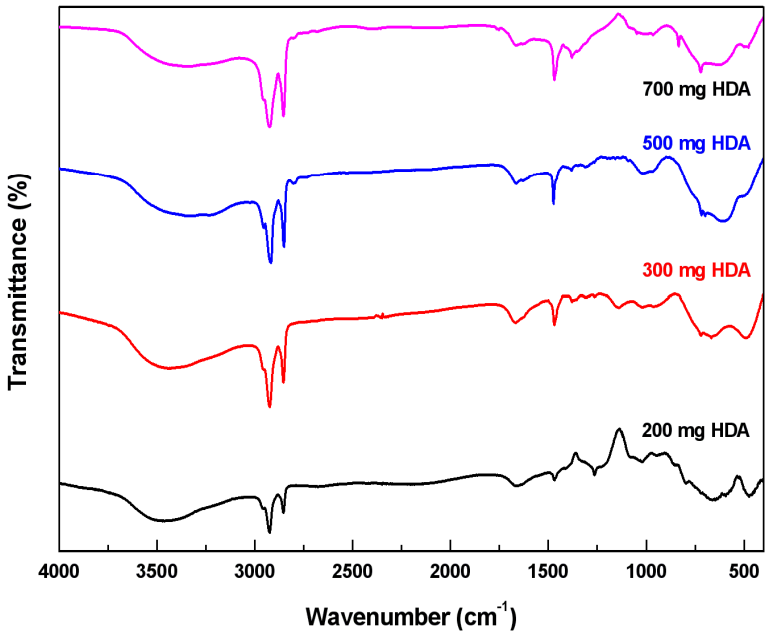


**Figure 3.5** IR spectrum of GaN prepared from $GaCl_3$ and $LiNH_2$ with different amount of HDA at 250 °C.

TGA traces (Fig. 3.6) showed a feature with an onset around 100 °C that could be due to loss of benzene that was dissolved in the HDA and hence not removed when the samples were dried under vacuum. Two further major features are then observed with onsets of around 300 and 400 ºC. It is likely that the lower temperature mass loss is unbound HDA and the higher temperature one is surface-bound, as the sample with only 200 mg HDA only shows the higher temperature feature. As would be expected, the second feature becomes more significant as more HDA is added while the loss of bound HDA remains fairly constant. It appears that addition of around 200 mg in these reactions results in no unbound HDA in the products.

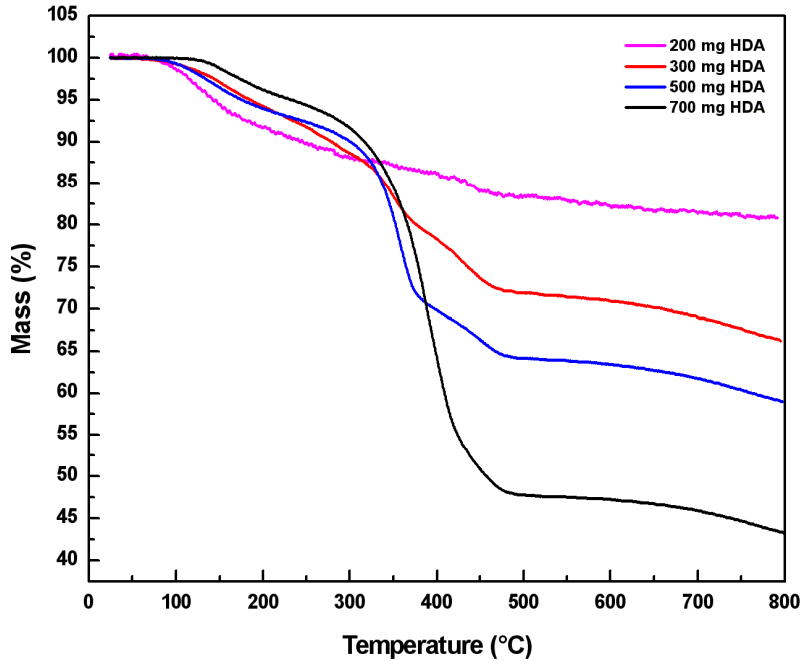


**Figure 3.6**. TGA of GaN produced from $GaCl_3$ and $LiNH_2$ with different amounts of HDA.

TEM images of these samples were somewhat indistinct, probably due to the HDA coating the spaces between particles, but it was apparent that there was a similar level of aggregation to that observed without HDA. TEM (Fig. 3.7) indicated particles of relatively small size (< 5 nm). The examination of these particles showed that they are composed of agglomerates of smaller particles.

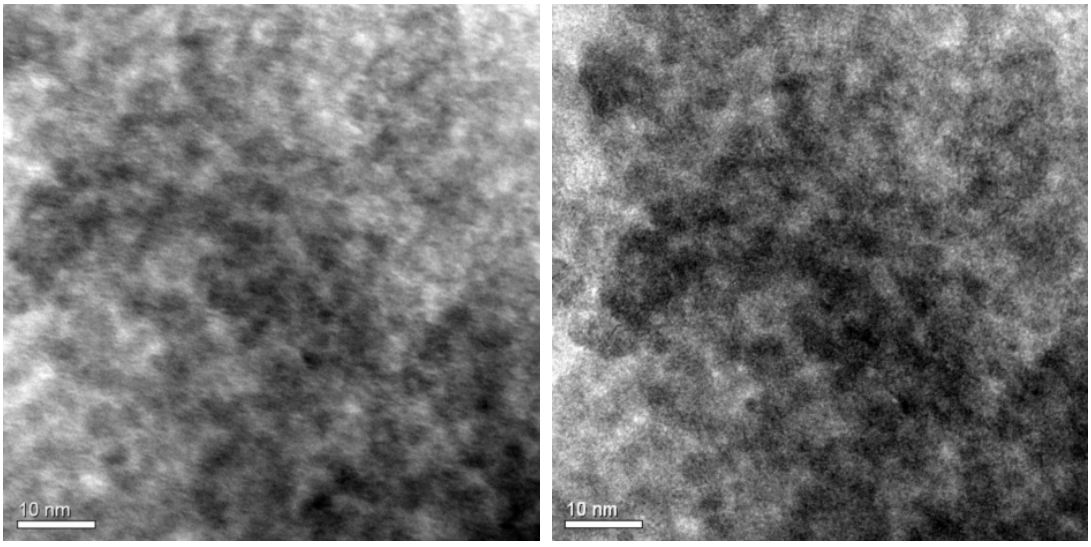


**Figure 3.7** TEM images of GaN prepared from $GaCl_3$ and $LiNH_2$ at 250 ºC with 200 mg HDA.

# 3.4 Reactions between $GaCl_3$ and $LiNH_2$ in the presence of CTAB

CTAB was previously used to cap GaN particles grown in solvothermal reactions between gallium cupferron or $GaCl_3$ and hexamethyldisilazane in toluene[26]. Addition of CTAB to the reactions between $GaCl_3$ and $LiNH_2$ resulted in similar PXD patterns (Fig. 3.8) to those observed with added HDA (Fig. 3.4). Small quantities (300-500 mg) resulted in a reduction in the amorphous content of the samples, but with larger additions (700 mg) the amorphous features returned to the PXD patterns.

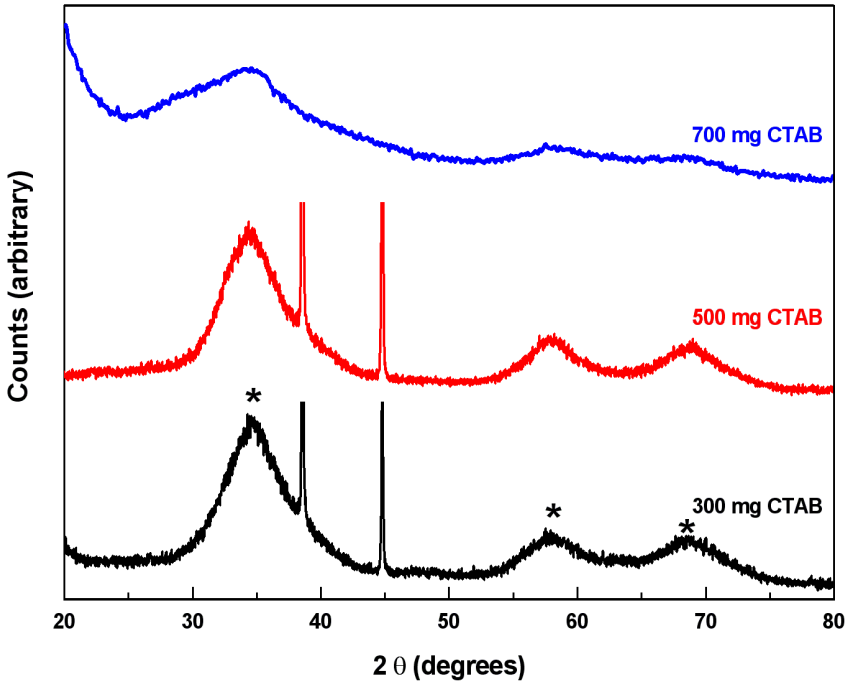


**Figure 3.8.** PXD patterns of the products from the reactions of $GaCl_3$ with $LiNH_2$ using different amounts of CTAB. Sharp peaks at 38 and 44º are due to the Al sample holder.

Lattice parameters, (Table 3.3), were slightly high, again probably reflecting some carbon incorporation. Interestingly the composition of the products varied less with the amount of CTAB and the nitrogen content was higher – presumably the higher solubility of CTAB than that of HDA in benzene and methanol allows more efficient removal of the former.

**Table 3.3**. Compositions and structural data for products of the reactions of $GaCl_3$ and $LiNH_2$ using different amounts of CTAB. Combustion analyses accurate to ± 0.3 %.

| Composition | CTAB (mg) | % C | % N | % H | Crystallite size, nm | a (Å) |
|---|---|---|---|---|---|---|
| $GaN_{0.73}C_{0.37}$ | 300 | 5.3 | 12.1 | 2.2 | 1.8 | 4.49 |
| $GaN_{0.61}C_{0.37}$ | 500 | 5.3 | 10.3 | 2.3 | 2 | 4.51 |
| | 700 | _ | _ | _ | 1.8 | 4.50 |

IR spectra (Fig. 3.9) contained a strong $\nu$(Ga-N) at ~600 $cm^{-1}$ and features corresponding to $\nu$(C-H) and $\nu$(N-H), the relative strength of these features also being very similar however much CTAB was added to the reaction mixture.

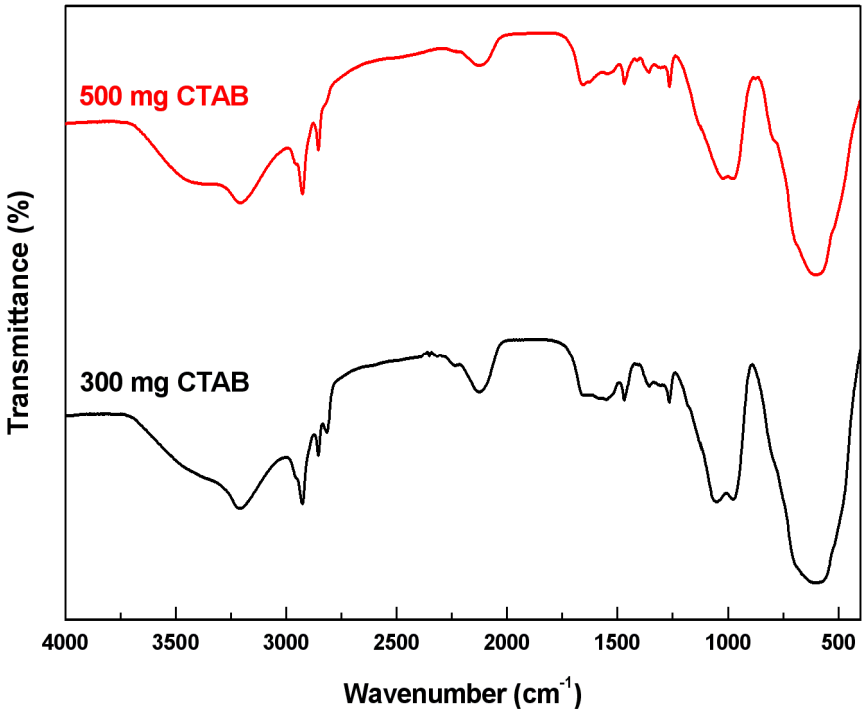


**Figure 3.9** IR spectra of the products of reactions of $GaCl_3$ with $LiNH_2$ using different amounts of CTAB.

The TGA traces were also very similar for samples made with different amounts of CTAB (Fig 3.10). The TGA profile in nitrogen shows a mass loss (~12 %) between 100 and 470 ºC which was assigned to the elimination of unbound CTAB. Only a small mass loss (~2 %) is observed in the temperature range of 470-650 ºC. Further mass loss (~4 %) after 650 ºC is due to the decomposition of the material with nitrogen elimination.

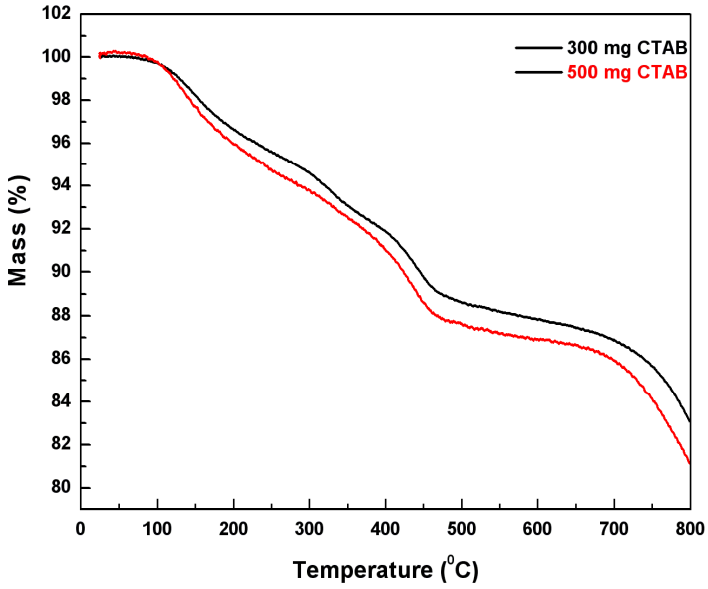


**Figure 3.10**. TGA of GaN produced from $GaCl_3$ and $LiNH_2$ with different amounts of CTAB.

Disappointingly TEM images still showed significant aggregation in these samples, though there was some evidence of individual particles with size of about 20 nm (Fig. 3.11). Compared with the particle size calculated from XRD pattern (~2nm) this value was bigger due to the agglomeration of small crystallites.

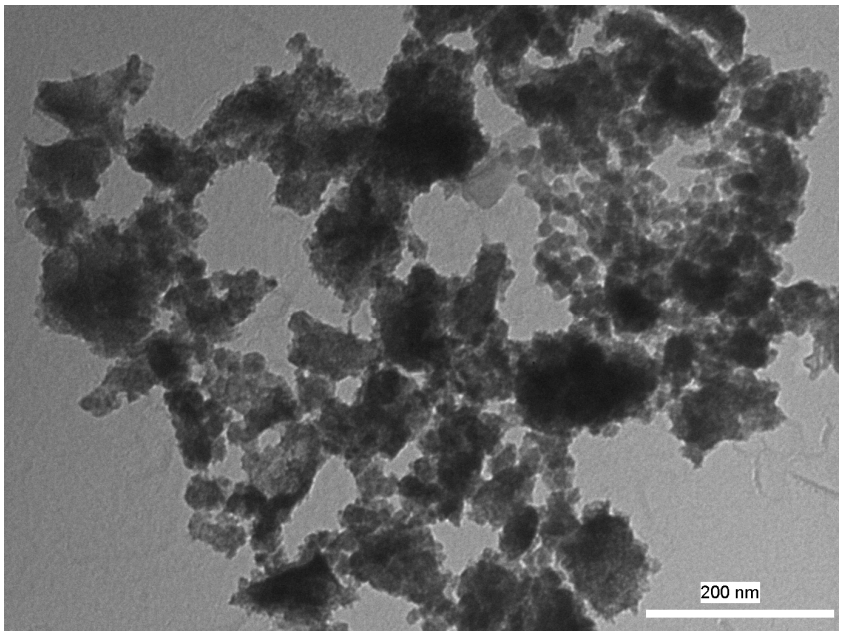


**Figure 3.11** TEM image of GaN produced from $GaCl_3$ and $LiNH_2$ with 500 mg added CTAB.

## 3.5 Reactions of $InCl_3$ and $InI_3$ with $LiNH_2$

The preparation of InN was investigated by methods analogous to those described in section 3.2 for GaN. Due to its low thermal stability[37, 38], InN is more difficult to synthesise by solid state methods than GaN. The formation of InN is expected take place via substitution of halide groups providing $NH_3$ and lithium halides as by products.

$$InX_3 + 3\,LiNH_2 \xrightarrow{\text{benzene}} InN + 2\,NH_3 + 3\,LiX \qquad (X = Cl, I)$$

Samples were prepared at temperature in the range 200-500 ºC. Reactions of $InCl_3$ with $LiNH_2$ resulted in samples containing In metal, even at temperatures well below the decomposition temperature of InN (Fig. 3.12). At 200 ºC a broad reflection is observed at $2\theta = 31º$ in addition to the In peaks, and this closely resembles the zinc blende-type GaN peaks. On raising the temperature sharper peaks at $2\theta = 29º$, 31º, 33º, 52º, 57º and 62º are assigned to the (100), (002), (101), (110), (103) and (200) planes of

wurtzite-type (hexagonal) InN, and on raising the temperature further to 500 ºC only In metal is observed. Addition of HDA to the low temperature (200 ºC) reaction did appear to reduce the amount of In metal in the samples, but significant amounts were still formed.

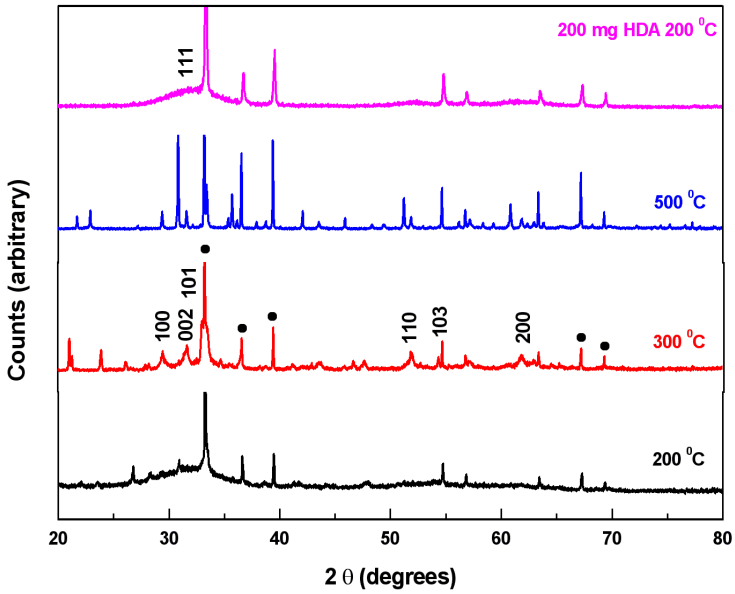


**Figure 3.12**. XRD patterns of samples produced from $InCl_3$ with $LiNH_2$ at different temperatures. Reflection positions for wurtzite (hexagonal $P6_3mc$) InN and In metal (indicated by dots) are marked over the pattern of InN prepared at 300 ºC and those of zinc blende (cubic F-43m) over the pattern achieved at 200 ºC using 200 mg of HDA.

An obvious way to reduce the amount of indium metal by-products in these reactions would be to increase the overall nitrogen content of the reaction mixture. Hence the effect of using an excess of the nitrogen source reagent, $LiNH_2$, was investigated. Fig.3. 13 shows the effect of excess $LiNH_2$. A small excess, 20 %, results in a reduction in the amount of In in the zinc blende-type InN products, but further additions of $LiNH_2$ resulted in no further improvement and, at 100 % excess, amorphous scattering was observed in the diffraction pattern.

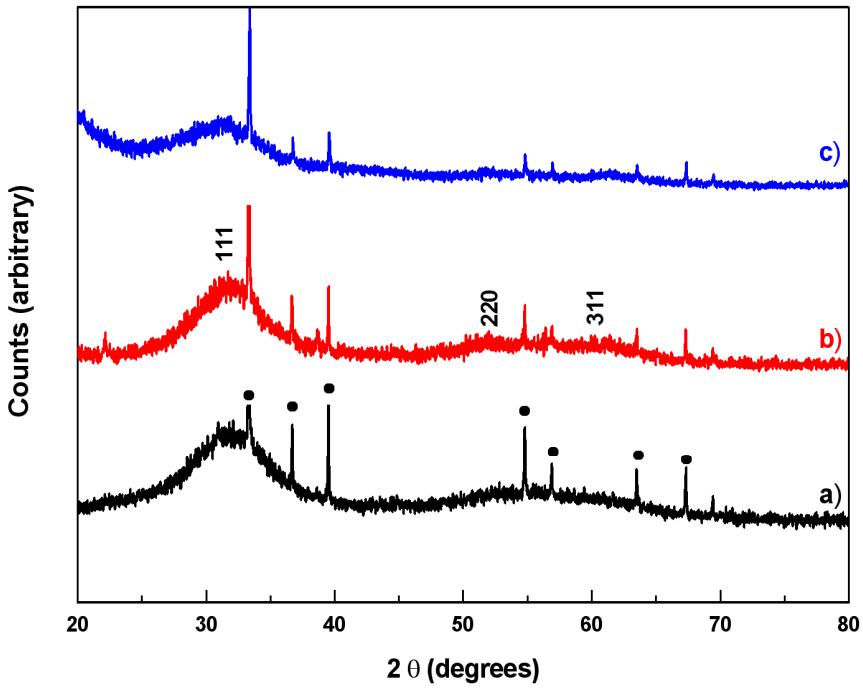


**Figure 3.13** XRD patterns of InN obtained using $InCl_3$ and $LiNH_2$ at 200 ºC using: a) a 20 % excess of $LiNH_2$, b) a 50 % excess of $LiNH_2$, and c) a 100 % excess of $LiNH_2$ (• marks peak positions attributable to In metal). Relection positions for InN zinc blende (cubic F-43m) are marked over the pattern achieved at 200 ºC using 50 % excess of $LiNH_2$. In metal reflections are marked with dots over the diffraction pattern a).

Another option that has been reported by others[28] is the synthesis of InN from $InI_3$ instead of $InCl_3$. $InI_3$ has a higher degree of covalent bonding than $InCl_3$ and this has been argued as the reason why $In^{3+}$ from $InI_3$ is less liable to be reduced to elemental indium. Samples were prepared at temperature of 250 º and 200 ºC in order to reduce the decomposition of indium nitride. Reflections at 2θ =29º, 31º, 33º, 43º, 52º, and 62º are assigned to the (100), (002), (101), (102), (110), and (112) planes of wurtzite (hexagonal) InN. In metal is marked on the diffraction patterns of InN by black dots. Reactions of $InI_3$ with $LiNH_2$, Fig. 3.14, resulted in wurtzite-type InN. Some indium was still also present even at 200 ºC, and the amount increased at 250 ºC.

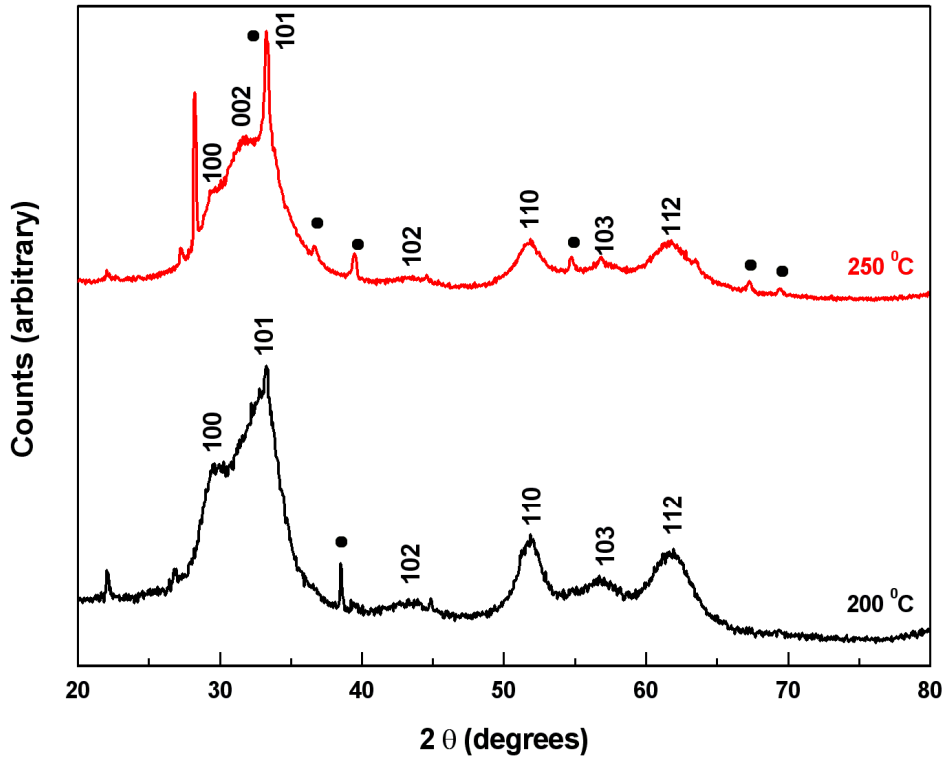


**Figure 3.14** XRD patterns of InN obtained from $InI_3$ with $LiNH_2$ at different temperatures. Relection positions for wurtzite type InN (hexagonal $P6_3mc$) are marked by Miller indeces and those of In metal by dots.

# 3.6 Experimental

All preparations were carried out under anaerobic conditions using either glove box or Schlenk line techniques for sample loading and handling. Benzene was distilled from Na, methanol from $NaOCH_3$ and hexadecylamine was vacuum distilled from BaO. $GaCl_3$ (99.999 %), $InCl_3$ (99.999 %), $InI_3$ (99.998 %) and *N*-cetyltrimethylammonium bromide (CTAB; >99 %) were purchased from Aldrich and used as supplied. Ammonia (Air Products) was distilled from a sodium/ammonia solution before use. $LiNH_2$ was synthesised by reacting 1.6 M $^n$BuLi in hexane (Aldrich) with excess distilled ammonia at -78 °C, filtering, and drying the product under vacuum.

All syntheses were performed in a 75 $cm^3$ autoclave (Parr 4740CH). Typically, 0.6 g of metal halide was placed in the silica liner and covered with 15 $cm^3$ of benzene. A stoichiometric amount of $LiNH_2$, calculated to balance the lithium and chloride components of the reaction mixture, was added. The autoclave was heated at different temperatures, typically for 24 h. After cooling to room temperature, the autoclave was opened and the mixture was transferred to a Schlenk tube inside the glove box. The solid was collected by filtration, washed with dry methanol three times to remove the LiCl by-product, and dried under vacuum.

Powder X-ray diffraction (PXD) measurements were performed on a Siemens D5000 diffractometer using Cu$K_{\alpha_1}$ ($\lambda$ = 1.5406 Å) radiation. The phases present were identified by comparison with the JCPDS database[39] and patterns refined using the GSAS package[31] Crystallite sizes were obtained using the Scherrer formula. Transmission electron microscopy (TEM) was carried out with a Hitachi 7000 (75 kV) instrument. Samples were prepared by ultrasound dispersal in toluene, followed by deposition on carbon-coated Cu grids. IR spectra were recorded as CsI disks using a Perkin Elmer Spectrum 100. TGA data were collected with a Mettler Toledo TGA851e under flowing high purity nitrogen with a heating rate of 10 º/min. C, H, N combustion analyses and Schöniger flask combustion analysis of chlorine content were carried out by Medac Ltd (Egham, Surrey, UK).

# 3.7 Conclusions

Solvothermal reactions of $GaCl_3$ with $LiNH_2$ are an effective method to produce nanocrystalline GaN. Samples were prepared at temperatures ranging from 250-450 ºC. At 250 ºC, GaN forms with the zinc blende structure type, whereas at higher temperatures a mixture of zinc blende and wurtzite-type phases forms. All the diffraction patterns of GaN show low crystallinity because of the mild conditions used. GaN nanoparticles with an average size ranging from 6 to 1.8 were achieved.
The characterization of the samples by TEM (Fig 3.3) revealed the presence of regular shaped crystallites though a significant aggregation of these crystallites was observed. All the samples had nitrogen deficient compositions with significant hydrogen and carbon content.

HDA and CTAB were investigated as agents capping in this work to reduce the aggregation and to control the particle size.
The addition of HDA resulted in an improved crystallinity of the final products. This may suggest that it was involved in the formation of GaN possibly reacting faster than $LiNH_2$ with $GaCl_3$. Smaller particles with size of about 2 nm were formed when HDA was used, but the aggregation was still evident. The lattice parameter of the samples prepared in HDA was higher than those achieved without HDA and significant carbon incorporation was observed in the nitride. The presence of HDA in the final product was also revealed by IR and TGA analysis.
The use of CTAB to cap particles had a similar effect to the use of HDA. The addition of small amount (300 or 500 mg) reduced the amorphous content while at higher concentration the amorphous content was evident at lower angles of $2\theta$. Smaller particles with size of 2 nm were observed by XRD, but aggregation was not fully inhibited, though the samples showed some individual particles.

The analogous reactions with $InCl_3$ produced InN, but this was contaminated with In metal even at temperatures as low as 200 ºC. Use of excess $LiNH_2$, or substitution of $InI_3$ for $InCl_3$, reduces the amount of indium metal in the products, but does not eliminate it entirely.

# 3.8 References


1. D. A. Neumayer and J. G. Ekerdt, *Chem. Mater.*, 1996, **8**, 9.
2. H. Monkoc, S. Strilé, G. B. Gao, M. E. Lin, B. Sverdlov and M. Burns, *J. Appl. Phys.*, 1994, **76**, 1363.
3. B. Garni, J. Ma, N. Perkins, J. Liu, T. F. Kuech and M. G. Lagally, *Appl. Phys. Lett.*, 1996, **68**, 1380.
4. S. D. Lester, F. A. Ponce, M. G. Craford and D. A. Steigerwald, *Appl. Phys. Lett.*, 1995, **66**, 1249.
5. F. A. Ponce, D. A. Bour, W. Götz and P. J. Wright, *Appl. Phys. Lett.*, 1996, **68**, 57.
6. A. P. Purdy, *Chem. Mater.*, 1999, **11**, 1648.
7. J. A. Jegier, S. McKernan, A. P. Purdy and W. L. Gladfelter, *Chem. Mater.*, 2000, **12**, 1003.
8. D. R. Ketchum and J. W. Kolis, *J. Cryst. Growth*, 2001, **222**, 431.
9. J. F. Janik, R. L. Wells, J. L. Coffer, J. V. St. John, W. T. Pennington and G. L. Schimek, *Chem. Mater.*, 1998, **10**, 1613.
10. J.-W. Hwang, J. P. Campbell, J. Kozubowski, S. A. Hanson, J. F. Evans and W. L. Gladfelter, *Chem. Mater.*, 1995, **7**, 517.
11. O. I. Mićić, S. P. Ahrenkiel, D. Bertram and A. J. Nozik, *Appl. Phys. Lett.*, 1999, **75**, 478.
12. J. Karpinski, J. Jun and S. Porowski, *J. Cryst. Growth*, 1984, **66**, 1.
13. D. R. Ketchum and J. W. Kolis, *J. Cryst. Growth*, 2001, **222**, 431.
14. B. Mazumder and A. L. Hector, *J. Mater. Chem.*, 2009, **19**, 4673.
15. G. Demazeau, *J. Mater. Sci.*, 2008, **43**, 2104.
16. J. B. Wiley and R. B. Kaner, *Science*, 1992, **255**, 1093.
17. J. C. Fitzmaurice, A. L. Hector and I. P. Parkin, *Polyhedron*, 1993, **12**, 1295.
18. J. C. Fitzmaurice, A. L. Hector and I. P. Parkin, *J. Chem. Soc. Dalton Trans.*, 1993, 2435.
19. A. L. Hector and I. P. Parkin, *J. Chem. Soc., Chem. Commun.*, 1993, 1095.
20. E. G. Gillan and R. B. Kaner, *Chem. Mater.*, 1996, **8**, 333.
21. E. G. Gillan and R. B. Kaner, *Inorg. Chem.*, 1994, **33**, 5693.
22. A. L. Hector and I. P. Parkin, *Polyhedron*, 1995, **14**, 913.
23. Y. Xie, Y. Qian, W. Zhang, S. Zhang and Y. Zhang, *Science*, 1996, **272**, 1926.
24. C. Falter, M. Klenner and Q. Chen, *Phys. Rev. B*, 1993, **48**, 16690.
25. Y. Zhang, J. Liu, R. He, Q. Zhang, X. Zhang and J. Zhu, *Chem. Phys. Lett.*, 2002, **360**, 579.
26. K. Sardar and C. N. R. Rao, *Adv. Mater.*, 2004, **16**, 425.
27. C. Wu, T. Li, L. Lei, S. Hu, Y. Liu and Y. Xie, *New J. Chem.*, 2005, **29**, 1610.

28. Y.-J. Bai, Z.-G. Liu, X.-G. Xu, D.-L. Cui, X.-P. Hao, X. Feng and Q.-L. Wang, *J. Cryst. Growth*, 2002, **241**, 189.
29. J. Choi and E. G. Gillan, *J. Mater. Chem.*, 2006, **16**, 3774.
30. J. Wang, L. Grocholl and E. G. Gillan, *Nano Lett.*, 2002, **2**, 899.
31. A. C. Larson and R. B. Von-Dreele, *General Structure Analysis System (GSAS), Los Alamos National Laboratory report LAUR*, 2004, 86-748.
32. B. H. Toby, *J. Appl. Crystallogr.*, 2001, **34**, 210.
33. G. Socrates, *Infrared and Raman Characteristic Group Frequencies, 3rd Ed. Wiley*, 2006, 109.
34. B. M. Gray, S. Hassan, A. L. Hector, A. Kalaji and B. Mazumder, *Chem. Mater.*, 2009, **21**, 4210.
35. A. W. Jackson and A. L. Hector, *J. Chem. Mater.*, 2007, **17**, 1016.
36. *Inorganic Crystal Structure Database accessed via "The United Kingdom Chemical Database Service" D. A. Fletcher, R. F. McMeeking and D. Parkin, J. Chem. Inf. Comput. Sci.*, 1996, **36**, 746.
37. S. Porowski and I. Grzegory, *EMIS Datarev.*, 1994, **ser. 11**, 82.
38. S. Krukowski, A. Witek, J. Adamczyk, J. Jun, M. Bockowski, I. Grzegory, B. Lucznik, G. Nowak, M. Wroblewski and A. Presz, *J. Phys. Chem. Solids*, 1998, **59**, 289.
39. *PCPDFWIN, version 2.4; Powder Diffraction File, International Center for Diffraction Data: Swarthmore, PA*, 2003.

# 4.1 Introduction

Group 5 nitrides (e.g. VN, NbN, TaN and $Ta_3N_5$) constitute an interesting class of compounds because of promising properties such as good chemical stability, high hardness, high melting point, catalytic or photocatalytic activity and superconductivity[1-4].

Vanadium nitride is an example of an interstitial nitride which does not have the exact stoichiometry 1:1[5]. This is due to the presence of extrinsic defects inside the lattice due to anion and/or cation vacancies[6]. At high temperature the defects are completely randomized but when it decreases defects cluster at certain points which will lead to dislocations and stacking faults[6]. The two more stable phases are the rocksalt VN and the hexagonal $V_2N$. Their properties are different from one another. VN is considered a refractory nitride and shows higher microhardness than $V_2N$. Vanadium mono-nitrides are extremely hard and have been utilized as abrasives and hardness coatings for tool steel. Moreover they have been found to exhibit some interesting properties as heterogeneous catalyst because of their selectivity and stability[7, 8]. For example vanadium nitrides prepared from $V_2O_5$ with $NH_3$ were stable and highly active butane dehydrogenation catalysts with selectivities greater than 98 %[7].

Nitrides of niobium are low T superconductors[9]. NbN system can form different phases such as β-$Nb_2N$ (hexagonal), γ-$Nb_4N_{3\pm x}$ (tetragonal), δ-$NbN_{1-x}$ (face centered cubic, fcc), η-NbN and β-NbN (hexagonal). Among these nitride the highest superconducting transition temperature is observed in δ-$NbN_{1-x}$ ($T_c$ = 17 K)[10].

Tantalum nitrides (TaN and $Ta_2N$) have been most prepared as thin films using deposition methods[11, 12]. Because of their interesting properties they were used for example as conductive coatings, cutting tools and to improve the resistance of refractory materials[11, 12].

Tantalum (V) nitride is one of the few metal nitrides to contain the metal in its maximum oxidation state. It has a band gap of 2.08 eV and is a red useful pigment and an active photocatalyst[13] in the visible region of the electromagnetic spectrum. It has been studied for use as a capacitor dielectric[14], a gas sensor material for propanal[15] and an antireflective coating in photolithography[16].

Metal nitrides have been prepared using several synthetic approaches. Typically they have been synthesized by the reaction of a metal or metal halide with ammonia or $N_2$ at high temperature[1, 2]. The main problems with this approach include the

incorporation of unreacted metal, non-stoichiometric inclusion of nitrogen in the product and the lack of control over crystallinity and particle size. Reactions of metal amides with ammonia in solvents such as benzene have also been investigated. This route is successful but the products tend to be contaminated by the presence of other elements and especially carbon.

Metathetical reactions have also been used to prepare metal nitrides. Reactions of metal chlorides ($VCl_3$, $NbCl_5$ and $TaCl_5$) with lithium amide[17], magnesium and calcium nitride[18], sodium azide and lithium nitride[19] were used to prepare metal nitrides. When $LiNH_2$ was used in the most case a thermolysis step at 700-800 °C for 1-2 h was important to prepare a crystalline nitride. The characterization of the powder by XRD showed that a cubic phase (VN, NbN, TaN) was produced. Reactions of metal chloride ($VCl_3$ and $TaCl_5$) with $NaN_3$, $Li_3N$ and $Ca_3N_2$ yielded a mixture of VN + $V_2N$ and TaN + $Ta_2N$, respectively. A more crystalline product was achieved when lithium nitride was used as nitrogen source. The reactions of $VCl_4$ and $NbCl_5$ with $Li_3N$ yielded a pure VN[20] and a mixture of $Nb_4N_3$ and $Nb_2N$[19], respectively.
Solid-state metathesis (SSM) reactions were rapid and highly exothermic. This approach has a wide applicability for refractory materials, but cannot be used for nitrides which decompose at low temperature (e.g. mid to late transition metals). Usually these reactions produce thermodynamically stable metal nitrides.

In this work solvothermal conditions were used as a route to transition metal nitrides. NbN has previously been obtained solvothermally from the reaction of $NbCl_5$ with $NaN_3$ in benzene at 380 ºC[21]. The product was cubic NbN with a cell costant a = 4.419 Å. The particle size was estimated to be 10-20 nm in diameter. Significant aggregation of these small particles was also revealed from TEM images. Other precedents for the solvothermal synthesis of nitrides involved the preparation of TiN[22, 23] and GaN[24] in benzene using reactive $Li_3N$ or $NaN_3$. Solvothermal reactions of metal halides ($NiBr_2$, $FeCl_3$, $MnCl_2$) and sodium azide in superheated toluene were also reported[25]. The method was used to prepare thermally metastable nitrides ($Ni_3N$, $Fe_2N$ and MnN) at relative low temperature (~300 ºC)[25]. Because of their low thermal stability was difficult to synthesize using conventional solid state methods.

Here, solvothermal conditions were used to prepare nitrides of group 5 and 6 (group 6 discussed in chapter 5). The solvent in these reactions played an important role, in fact it can absorb part of the heat produced during the reactions resulting in a more controlled growth of crystallites. The methods were easy to use with the ability to change the solvent, temperature and reaction time. The phase, crystallinity and composition of the nitrides prepared at different temperature were studied.

# 4.2 Reactions of $VCl_3$, $NbCl_5$ and $TaCl_5$ with $LiNH_2$

The main aim of this work was to investigate the reactions of transition metal chlorides ($VCl_3$, $NbCl_5$, $TaCl_5$) with nitrogen sources under solvothermal conditions in benzene up to 550 ºC. These reactions are highly exothermic, but it was expected that the temperature would be controlled by absorption of heat into the solvent, in contrast with solid state metathesis reactions. Hence more nitrogen-rich composition, and smaller crystallite sizes should be achieved. Two different nitrogen sources, $LiNH_2$ and $NH_3$, have been used to prepare nitrides of group 5, and reactions with $LiNH_2$ will be described first.

## 4.2.1 Reactions of $VCl_3$ with $LiNH_2$

Previously metathesis reactions were made in order to produce crystalline VN. These were prepared by thermal initiation of reaction between vanadium chlorides ($VCl_3$ or $VCl_4$) and $Li_3N$[26]. The reactions of $VCl_3$ with $Li_3N$ yielded a mixture of cubic VN and hexagonal $V_2N$ (minor phase). The lattice parameter observed in these structures was a = 4.10 Å for VN and a = 4.34 and c = 4.54 Å for $V_2N$. These values were close to those reported in literature[26]. Microanalysis of the nitride prepared revealed ~10 % of nitrogen and no chlorine was present. Pure cubic VN (a = 4.10 Å) was obtained from the reaction of liquid $VCl_4$ and $Li_3N$[26]. These reactions required a careful attention because they self-initiated without no external heating. The nitrides were crystalline with an average size of 30 nm.

The reactions of $VCl_3$ with $NaN_3$ yielded a mixture of VN and $V_2N$[19]. These reactions were more exothermic of that carried out with $Li_3N$, but they yielded less crystalline products. Pure cubic VN was prepared from $VCl_3$ with $Mg_3N_2$ at 500 or 900 °C[18], while the reactions of $VCl_3$ with a mixture of $Mg_3N_2$ and $Ca_3N_2$ yielded pure hexagonal $V_2N$[18]. Crystalline VN was also formed from $VCl_3$ and $LiNH_2$ at 700 °C[17]. The sample was nitrogen deficient ( N 19 %) compared with the calculated value of 21.5 %.

Two sources of vanadium, $VCl_4$ and $VCl_3$, were initially considered in this work as potential reactants in the reactions with lithium amide in benzene. The use of $VCl_4$ led to several issues because it is a poisonous and corrosive liquid. It is also highly reactive with moisture in the atmosphere and its manipulation requires particularly careful attention. The transfer of $VCl_4$ into the autoclave via syringe was also inefficient

because it often remained on the side of the syringe and an excess was required to compensate this loss. $VCl_3$ is in a solid form and it was preferred to $VCl_4$.
Reactions of $VCl_3$ with $LiNH_2$ were carried out in benzene at temperatures in the range 250-550 °C, through the following reaction:

$$VCl_3 + 3\ LiNH_2 \xrightarrow{\text{benzene}} VN + 3\ LiCl + 2\ NH_3$$

PXD patterns shown in Fig. 4.1 matched rocksalt (Fm-3m) vanadium nitride. Rietveld refinements of all the PXD patterns revealed nanocrystalline vanadium nitride with particle size ranging from 7 to 15 nm at temperatures in the range 250-550 ºC. Decreasing the reaction temperature broader peaks were observed and crystalline VN was formed at temperatures as low as 250 ºC.

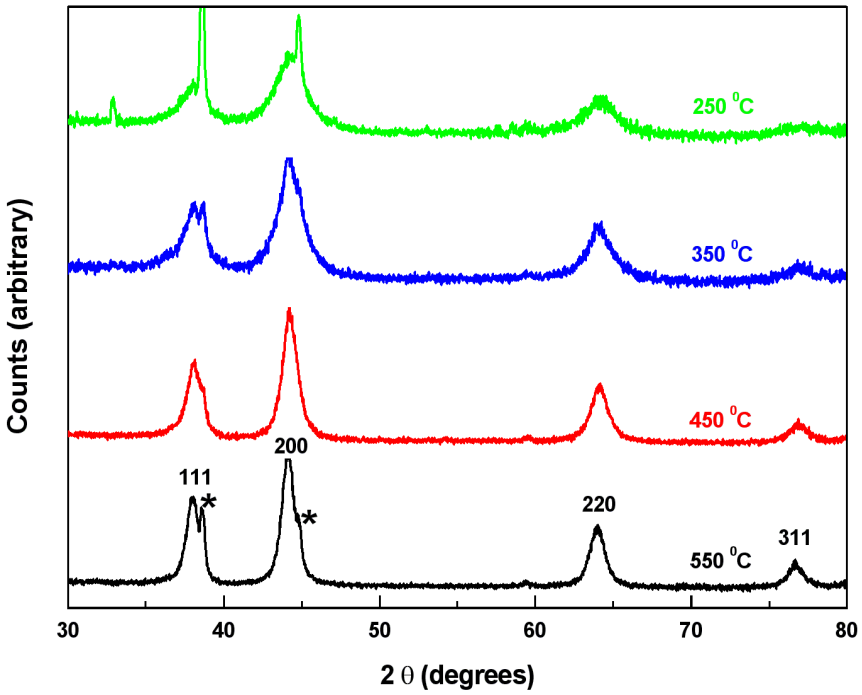


**Figure 4.1** XRD patterns of VN produced from $VCl_3$ with $LiNH_2$ at different temperatures. Reflection positions for rocksalt VN (Fm-3m) are marked over the pattern of VN prepared at 550 ºC. Two aluminium peaks resulting from the sample holder are also visible in all data sets at 38º and 44º and marked by asterix.

All the materials identified as VN by X-ray powder diffraction (Fig. 4.1) revealed nitrogen deficient compositions (expected 21.5 %) by microanalysis (Table 4.1). Non-stoichiometric phases are common in metal nitrides; hence they have often been referred to as “interstitial alloys”.

Refined lattice parameters, carbon and nitrogen analyses are listed in Table 4.1. VN crystallises with the rocksalt structure (Fm-3m), with reported lattice parameters in the range 4.133-4.140 Å[27]. In a study of variable vanadium nitride compositions, values from 4.06 ($VN_{0.71}$) to 4.13 ($VN_{1.00}$) Å were obtained[28]. The lattice parameters suggest samples close to stoichiometry, but the nitrogen analyses show them to be nitrogen deficient, with the most nitrogen rich sample produced at 450 °C and having a composition of $VN_{0.71.}$

**Table 4.1.** Products of reactions of group 5 halides with $LiNH_2$ heated for 24 h in benzene.

| Halide | T/°C | Product/s (lattice parameters in Å) | Size (nm) | % C, N | Composition |
|---|---|---|---|---|---|
| $VCl_3$ | 250 | VN (a = 4.1035(8)) | 7 | 1.5, 13.4 | $VN_{0.57}C_{0.07}$ |
| | 350 | VN (a = 4.1265(17)) | 15 | 1.1, 14.9 | $VN_{0.64}C_{0.05}$ |
| | 450 | VN (a = 4.1229(12)) | 17 | 1.1, 16.2 | $VN_{0.71}C_{0.06}$ |
| | 550 | VN (a = 4.1281(8)) | 15 | 1.3, 13.4 | $VN_{0.56}C_{0.06}$ |
| $NbCl_5$ | 450 | NbN (a = 4.394(4)) + some amorphous | 3 | 1.9, 9.1 | $NbN_{0.68}C_{0.16}$ |
| | 500 | NbN (a = 4.328(3)) + some amorphous | 9 | 0.8, 12.4 | $NbN_{0.95}C_{0.07}$ |
| | 550 | NbN (a = 4.3371(10)) | 9 | 3.0, 11.7 | $NbN_{0.91}C_{0.27}$ |
| $TaCl_5$ | 450 | Amorphous | | 0.7, 7.4 | |
| | 500 | $Ta_3N_5$ (a = 3.896(2), b = 10.231(4), c = 10.286(4)) | 24 | 1.4, 9 | $Ta_3N_{3.88}C_{0.70}$ |
| | 550 | $Ta_3N_5$ (a = 3.895(3), b = 10.217(6), c = 10.287(6)) | 25 | 1.6, 9.5 | $Ta_3N_{4.13}C_{0.81}$ |

Fig 4.2 shows an example of the refined PXD data sets for the product of reaction of $VCl_3$ with $LiNH_2$ at 450 ºC. Structural refinement was carried out using the Rietveld method. The initial atom positions and lattice parameter used as the starting point for the refinement was those of the rocksalt VN (Fm-3m). Refinement of scale factors, lattice parameter and background led to a fit of $R_{wp}$ = 10 %, $R_p$ = 7.8 % and $\chi^2$ = 2.8. The discrepancies between observed and calculated intensity at $2\theta$ = 38 and 44º are due to the strong reflections of aluminium resulting from the sample holder. The value of the Lorentzian component, extracted from GSAS refinement, was then used in the Scherrer equation to calculate a particle size of 15 nm. Refinement of the PXD pattern yielded a lattice parameter of a = 4.1229(12) compared with literature value of 4.06 for N-

deficient compositions. It is likely that some carbide is incorporated into the lattice causing expansion of the unit cell (VC has a larger lattice parameter of 4.163-4.172 Å)[27], hence the real composition at 450 °C could be $VN_{0.71}C_{0.06}$ or a lower carbon-containing composition with some elemental C.

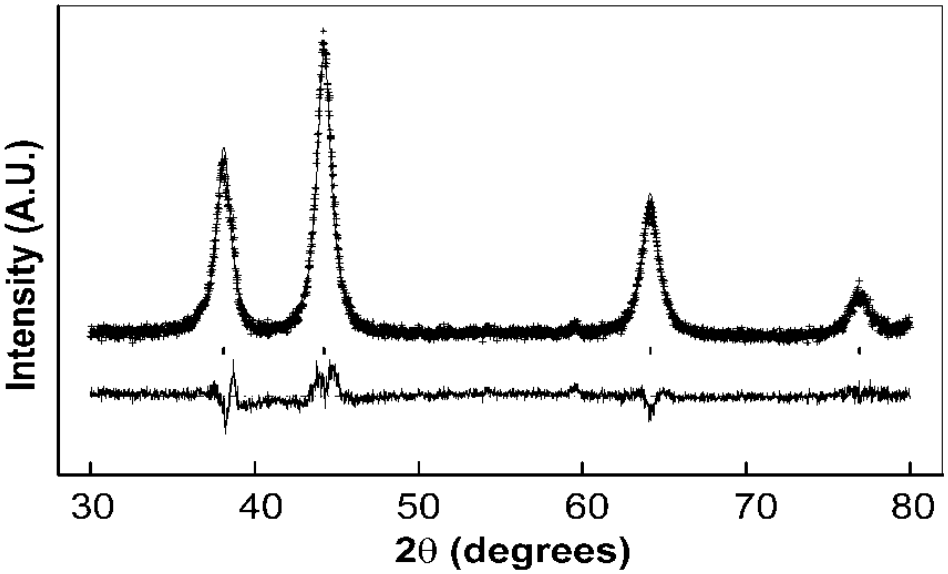


**Figure 4.2**. Fit to the PXD pattern of VN produced at 450 °C. Allowed reflections are shown by tick marks, data points by crosses, the upper continuous line the fit and the lower continuous line the difference.

TEM image (Fig. 4.3) revealed a distribution of spherical particles of about 5 nm broadly consistent with the size calculated from the XRD data. Aggregation of these small crystallites was also revealed.

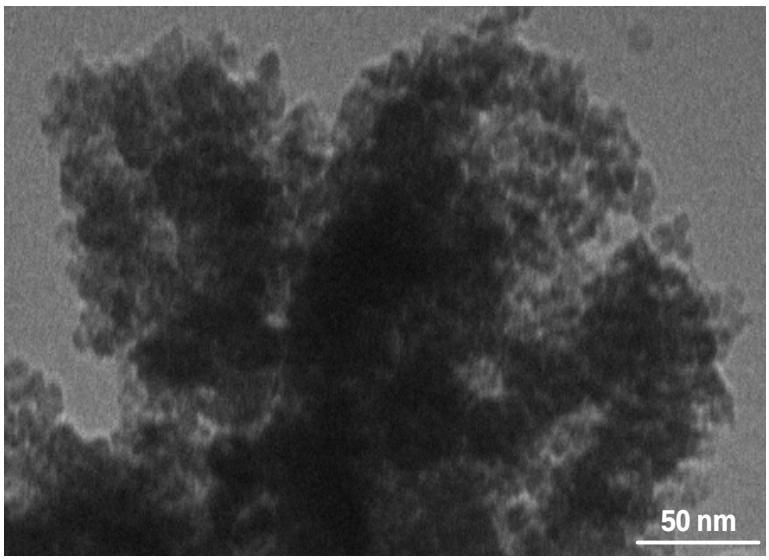


**Figure 4.3** TEM image of VN prepared from $VCl_3$ and $LiNH_2$ at 550 ºC.

The TGA profile of VN under oxygen atmosphere (Fig. 4.4) shows a mass gain (~ 35 %). The vanadium content (84 %) was calculated assuming that at high temperature all VN is converted in $VO_2$. In this case the composition was $VN_{0.56}C_{0.06}$ with low carbon content of about 1.3 %.

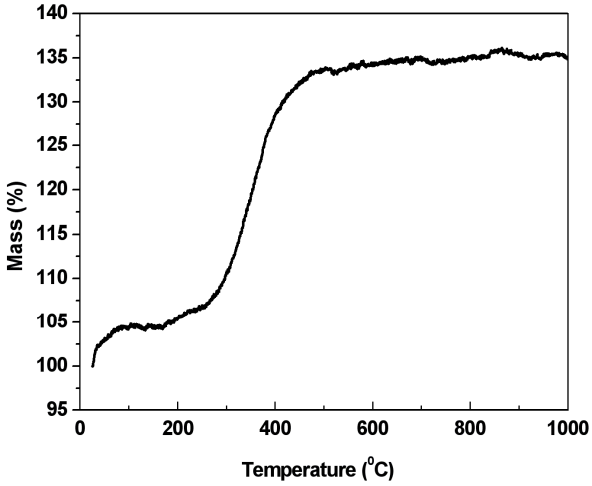


**Figure 4.4** TGA under oxygen of VN produced from $VCl_3$ and $LiNH_2$ at 550 ºC.

## 4.2.2 Reactions of $NbCl_5$ with $LiNH_2$

Solid state reactions were employed to prepare niobium nitride. For example the reaction of $NbCl_5$ with $Li_3N$ led to a mixture of $Nb_4N_3$ and $Nb_2N$[26]. The preparation of NbN was also carried out by filament initiated reactions of $NbCl_5$ with a mixture of $Ca_3N_2$ and $Mg_3N_2$ in a 1:2 ratio[18]. The resulting producted was a mixture of $Nb_2N$ and NbN.

In this work solvothermal preparation of NbN was carried out at various temperatures to determine the temperature at which products were crystalline, and the range of phases which could be obtained. PXD patterns shown in Fig. 4.5 matched cubic niobium nitride. NbN formation required the reduction of niobium, presumably balanced by $N_2$ evolution:

$$NbCl_5 + 5\ LiNH_2 \xrightarrow{\text{benzene}} NbN + {}^{10}/_3\ NH_3 + {}^{1}/_3\ N_2 + 5\ LiCl$$

Rietveld refinements of all the PXD patterns revealed nanocrystalline niobium nitride with particle size ranging from 3 to 9 nm at temperature in the range 450-550 ºC.

From the X-ray diffraction pattern of the resulting NbN, the width of the peaks changed with the temperature from 450 to 550 °C (Fig. 4.5). This phenomenon was attributed to a change in the size of the NbN particles with temperature.

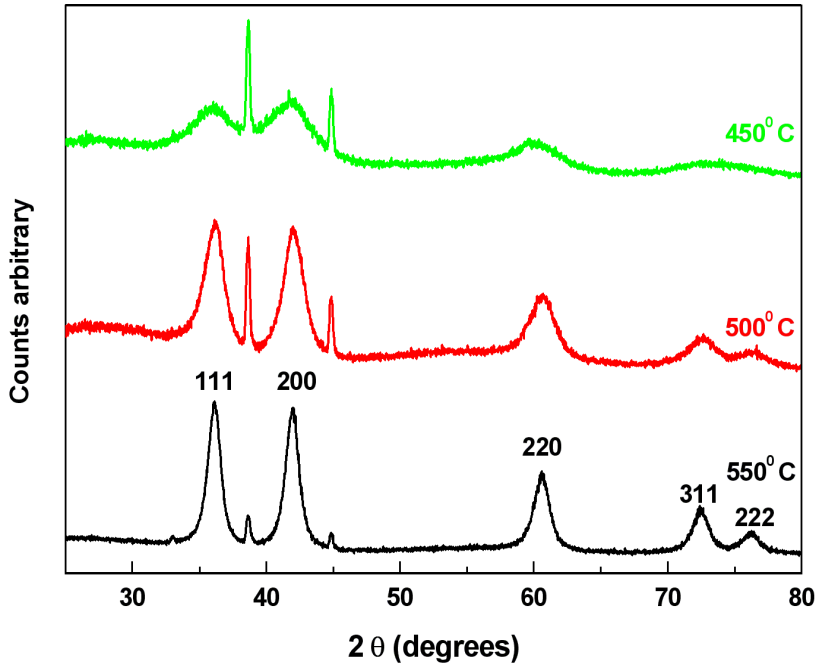


**Figure 4.5** PXD patterns of cubic NbN at different temperatures. The peaks from the aluminium sample holder are at 38 and 44º.

NbN was obtained between 450 and 550 ºC. Amorphous material was observed at 450 and 500 ºC via broad features in the PXD baseline. Crystallite sizes (3-9 nm) were generally smaller than those of VN (7-15nm). The most nitrogen-rich phase, synthesised at 500 °C, was close in composition to NbN (13.1% N calculated). Lattice parameters for NbN are typically reported as 4.375-4.394 Å, higher than those reported in Table 4.1, and, where accurate analyses are given in the literature, nitrogen deficient compositions to $NbN_{0.84}$ fall within this range[27]. NbC compositions have lattice parameters of 4.45-4.47 Å so carbon content would lead to high values as observed with VN. Uncertainty in the refinements at 450 and 500 ºC due to the amorphous content of the two lower temperature samples, seen in the broad baseline features, could explain the variation in the lattice parameter between samples, but the parameter is still a little low in the sample produced at 550 ºC.

As can be seen in Fig. 4.6, TEM images revealed a homogenous distribution of particles of around 6-8 nm consistent with the particle sizes derived from the PXD patterns. Moreover the same d-spacings associated with the cubic structure were observed by

electron diffraction. The texture diffraction rings in the electron diffraction patterns suggest that each particle may be a single crystallite.

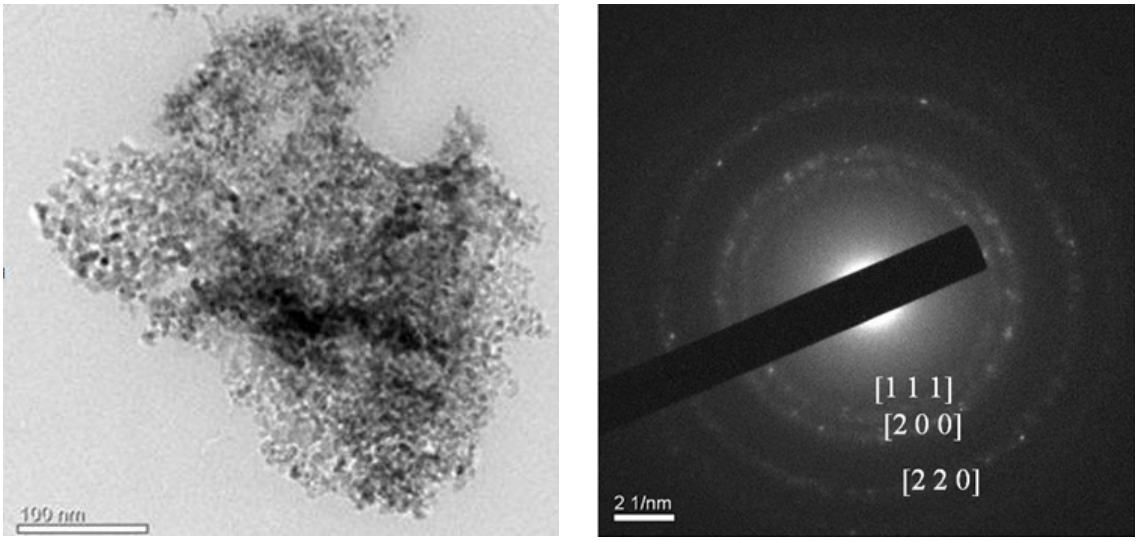


**Figure 4.6** TEM image of the materials synthesised from $NbCl_5$ and $LiNH_2$ at 550 ºC.

Infrared spectroscopy was used to characterize the as-prepared powders. A few mg of samples were ground in an agate mortar and mixed with ~ 200mg of CsI inside the glove box. The data sets were collected in the range 4000-400 $cm^{-1}$. The IR spectrum (Fig. 4.7) of the sample prepared at 550 º C showed ν NH (~ 3420 $cm^{-1}$), bending NH (1619 $cm^{-1}$) δ $NH_2$ (1400 $cm^{-1}$) features as well as a broad ν MN band (~570 $cm^{-1}$)[29]. The observation of νNH and δ $NH_2$ features suggested the presence of surface amide groups an extended in the final products, unsurprising considering the particle size is small so the surface is a significant fraction of the volume.

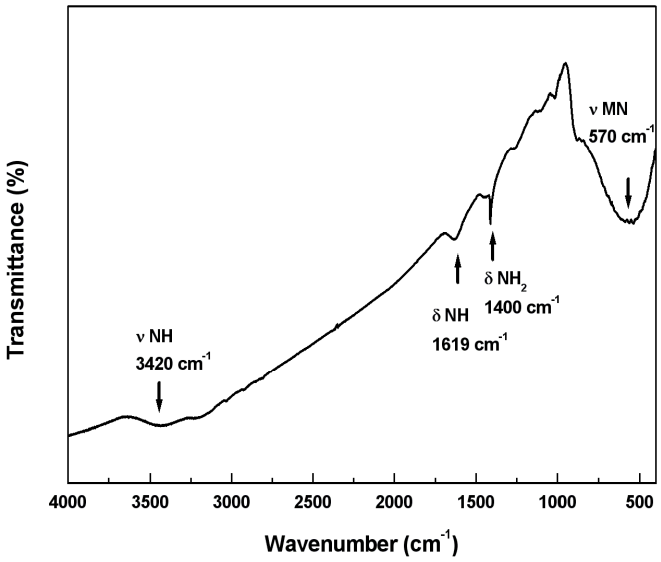


**Figure 4.7** IR spectrum of NbN prepared from $NbCl_5$ with $LiNH_2$ at 550 ºC.

## 4.2.3 Reactions of $TaCl_5$ with $LiNH_2$

Solid state reactions of $TaCl_5$ with $Li_3N$ were previously investigated in order to prepare tantalum nitrides[26]. These reactions thermally initiated up to 425 °C are highly exothermic and rapid. The nitrides formed were a mixture of cubic TaN and hexagonal $Ta_2N$. A successful preparation of $Ta_3N_5$ was obtained from $TaCl_5$ and $LiNMe_2$[17]. These reactions initiated at ~ 300 °C yielded initially an amorphous material which was crystalline $Ta_3N_5$ after thermolisis at 700 °C. Microanalysis revealed of N (11.7 %) and C less than 1 %. Reactions of $TaCl_5$ with $Li_3N$[26] or a mixture of $Ca_3N_2$ and $Mg_3N_2$[18] originated high temperature (more than 900 °C) which led to decomposition of nitride formed. Hence $Ta_3N_5$ starts to decompose at around 900 °C[30] the preparation of this nitride was limitated because of the high temperature generated in these reactions.

In order to reduce the reaction temperature and as consequence provide a better control on the size and morphology of tantalum nitrides, solvothermal conditions were investigated. Reaction of tantalum dialkylamide with $LiNH_2$ at 500 °C in benzene was previously reported[31]. Broad reflections in the PXD pattern resembled the cubic-type TaN phase. Refined lattice parameter was a = 4.302(2) Å lower than those reported in literature (a = 4.331-4.339 Å). In TaN produced the nitrogen content observed was ~7 % as expected for stoichiometric TaN phase (7.2 % calculated). A significant amount of carbon (15 %) was also present in the final nitrides, due to the pyrolysis of the dyalkil groups. TEM images showed isotropic particles with size of about 8 nm in diameter.

In order to reduce the carbon content in the final material, solvothermal preparation of tantalum nitride was performed from $TaCl_5$ (free-carbon precursor) and $LiNH_2$ in benzene at temperatures in the range 450-550 °C. The resulting powders were analyzed by XRD, TEM, IR and microanalysis. The formation of $Ta_3N_5$ must take place via stepwise substitution of chloride groups and condensation with the elimination of $NH_3$:

$$3\ TaCl_5 + 15\ LiNH_2 \xrightarrow{\text{benzene}} Ta_3N_5 + 15\ LiCl + 10\ NH_3$$

These reaction led to the formation of $Ta_3N_5$ which was not formed when $Ta(NMe)_5$ was used as starting material. In the reaction showed above the oxidation state of the metal (+5) in maintained also in the nitride produced while when $Ta(NMe)_5$ is used a reduction of tantalum from +5 to + 3 is observed.

Fig 4.8 shows the evolution of $Ta_3N_5$ with the reaction temperature. Reflections positions marked by Miller indices over the pattern achieved at 550 ºC (Fig. 4.8) are characteristic of orthorhombic type $Ta_3N_5$ (Cmcm). PXD shows a small amount of tetragonal type $Ta_4N_5$ (I4/m) as a second phase revealed from the presence of two peaks at $2\theta$ = 42º and 61º assigned to the (002) and (312) planes respectively. Presumably $Ta_4N_5$ was formed through reduction of some tantalum. A small amount of amorphous scattering was observed at 500 ºC but at 550 ºC the sample was fully crystallised.

Rietveld refinements of the PXD patterns obtained at 550º and 500 ºC revealed nanocrystalline $Ta_3N_5$ with similar particle sizes of about 24 nm. The lattice parameter (Table 4.2) are close to to typical literature values of a= 3.89, b = 10.22 and c = 10.28 Å[30]. The samples as-prepared were nitrogen deficient (~ 9.5 % N observed) compared with stoichiometric sample (11.7 % N calculated). Carbon content in the nitrides made at 550 and 500 °C was similar (~1.5 %).

As can be seen in Fig. 4.8, at 450 ºC the product was amorphous, three broad humps were observed centred at $2\theta$ = 35.5º, 42º and 60º which resembled the 111, 200 and 220 reflections of cubic TaN (Fm-3m) suggesting some short-range order with a roughly rocksalt type atomic arrangement.

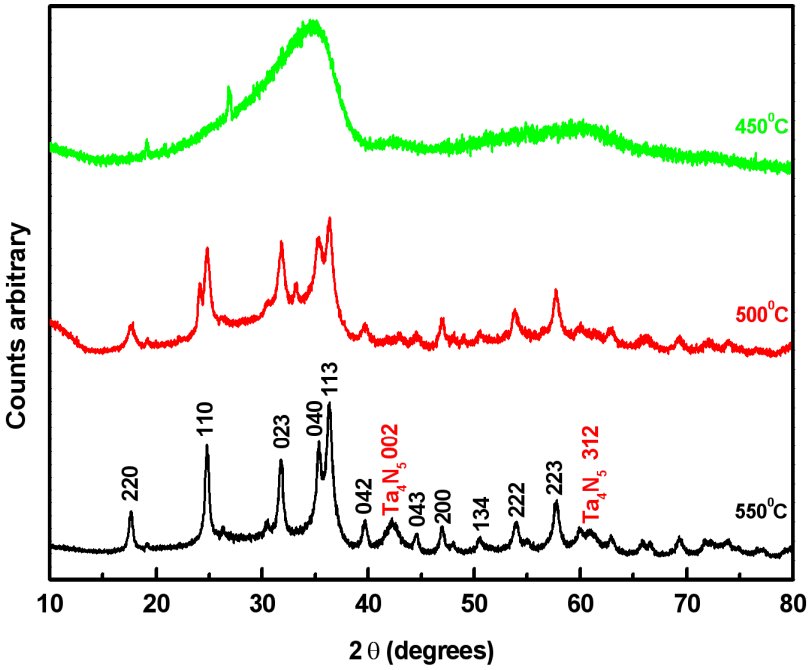


**Figure 4.8.** XRD patterns of the products of reaction of $TaCl_5$ with $LiNH_2$ heated for 24 h at three different temperatures. Miller indices for $Ta_3N_5$ [JCPDS 72-0813] are marked in black. The peaks at 42.3 and 61 degree of 2 theta were the most intense reflections of $Ta_4N_5$ [75-0627].

Samples were terracotta in colour and microanalysis of products indicated carbon incorporation in these phases (Table 4.1). Diffuse reflectance UV-visible spectra, Fig. 4.9, show that the samples prepared at 500 and 550 ºC were semiconducting. The band gap is 2.08 eV for the sample produced at 550 ºC and 2.10 eV at 500 ºC compared with literature value of 2.06-2.08 eV[13, 30, 32].
Above the band edge the absorbance falls away, this is believed to be due to the small particles size.

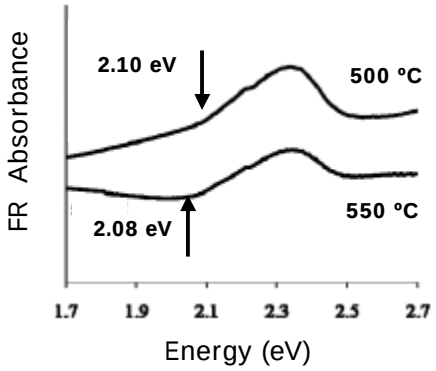


**Figure 4.9.** Diffuse reflectance UV/Visible spectra of $Ta_3N_5$ made at 500 and 550 ºC.

$Ta_3N_5$ has been crystallized directly in a solvothermal process at a lower temperature than used in its synthesis in the solid state[30]. Moreover the reactions didn`t require an annealing step that was common in the preparation of refractory materials.
Table 4.1 shows that the composition of tantalum nitride is highly nitrogen-deficient ($N_{theor}$ =11.4 %). The presence of carbon in the final product was due to the considerable charring of the benzene. Small amounts of H (0.9%) and Cl (<1%) were also present.
The crystallographic b-axis is sensitive to compositional variations in $Ta_3N_5$ and is usually linked with defects or oxide ions in the lattice[30, 33], here the lattice parameters (table 4.1) were close to those of the $Ta_3N_5$ standard.

TEM showed isotropic particles of around 20 nm diameter, again matching closely the PXD derived crystallite size, with electron diffraction showing the textured rings corresponding to the lattice spacings of $Ta_3N_5$ (Fig. 4.10).

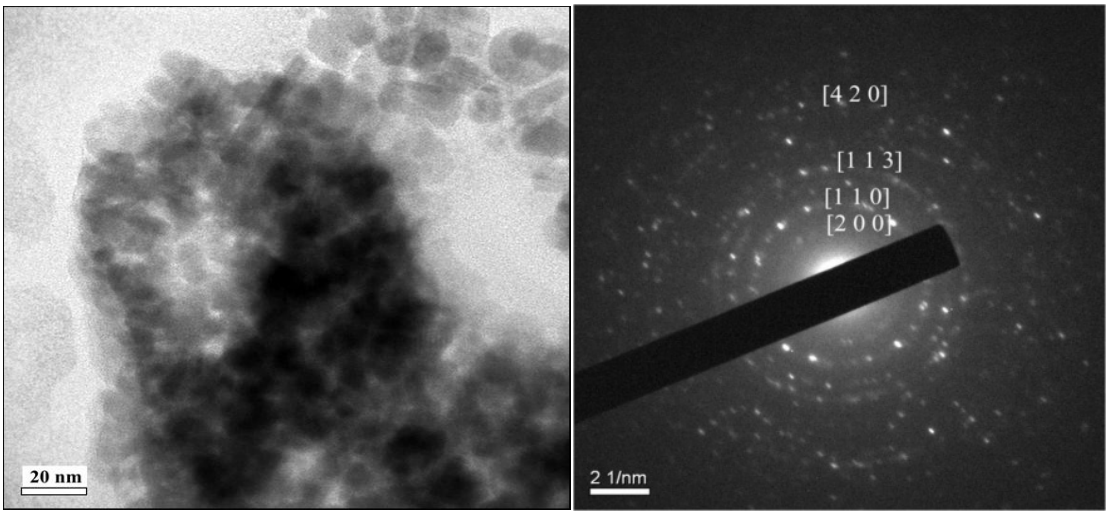


**Figure 4.10.** TEM image and electron diffraction of $Ta_3N_5$ prepared in benzene at 550 ºC.

The IR spectrum (Fig. 4.11) of $Ta_3N_5$ prepared at at 550 and 500 ºC showed ν NH (~ 3450 $cm^{-1}$), sharp ν CH (~ 2928-2848 $cm^{-1}$), bending NH (1614 $cm^{-1}$) and δ $NH_2$ (1400 $cm^{-1}$) features as well as a broad ν MN band (~600 $cm^{-1}$). Decreasing the reaction temperature the solvent decomposition may be reduced as the characteristic absorption peaks of ν CH were not observed at 450 ºC. As for the niobium nitride the observation of N-H groups suggested that chloride species were replaced by amide or imide groups during the course of the reactions that led to formation of the nitride product.

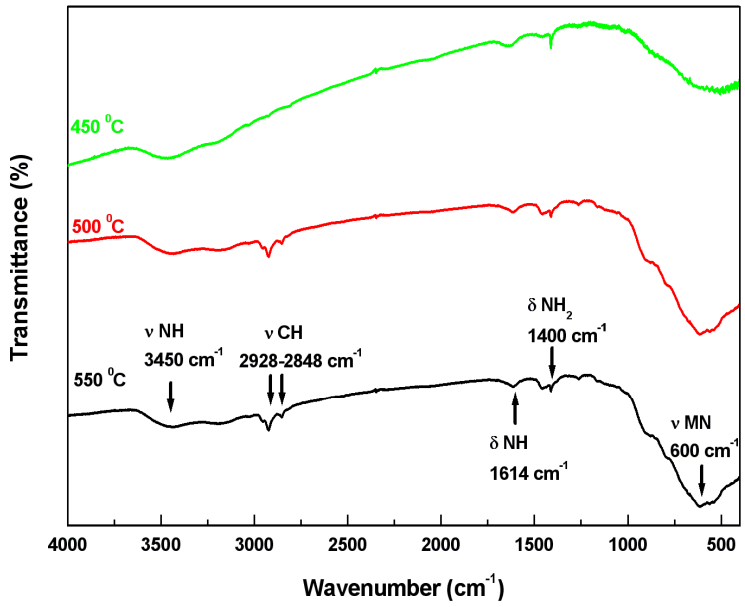


**Figure 4.11** IR spectrum of $Ta_3N_5$ prepared from $TaCl_5$ with $LiNH_2$ at different temperatures.

# 4.3 Reactions of $VCl_3$, $NbCl_5$ and $TaCl_5$ with $NH_3$

These reactions were investigated to determine whether they could be used to produce nitrides under solvothermal conditions and to provide a lithium-free alternative route compared with lithium amide. Because ammonia is a gas at room temperature and atmospheric pressure it is more difficult to handle than $LiNH_2$. All the experiments were carried out using a vacuum line and a glove box to deal with filling ammonia into the autoclave and handling the metal chlorides which are sensitive to air and moisture.

In a typical reaction 0.6 g of metal chloride was placed into the silica liner with 15 $cm^3$ of benzene. The autoclave was then sealed and chilled to – 78 ºC with dry ice and

acetone. Dried ammonia was condensed into a volumetric Schlenk tube and a 10-fold molar excess compared with the stoichiometric amount according to the following equation was transferred by cannula into the autoclave:

$$MCl_x + 2_xNH_3 \longrightarrow \text{“}M(NH_2)_x\text{”} + {}_xNH_4Cl$$

The excess of ammonia was used to ensure sufficient ammonia was present in the system and replacement of chloride. After transferring ammonia, the autoclave was left to warm to room temperature and then heated for 24 h at a specific temperature. The autoclave was then cooled to room temperature and depressurised from the ammonia. The products of the silica liner were collected into a Schlenk tube into the glove box and after removing the solvent were washed with methanol and dried under vacuum.

### 4.3.1 Reactions of $VCl_3$ with $NH_3$

These reactions were carried out by condensing an excess of dried ammonia onto a benzene solution of vanadium chloride in the autoclave before heating at the temperatures shown in Table 4.2. The reactions proceed by sequential replacement of chloride groups as follows:

$$VCl_3 + 6\ NH_3 \longrightarrow \text{“}V(NH_2)_3\text{”} + 3\ NH_4Cl$$
$$V(NH_2)_3 \longrightarrow VN + 2\ NH_3$$

PXD patterns (Fig. 4.12) matched rocksalt (Fm-3m) vanadium nitride. The main reflection positions are marked by Miller indices over the pattern obtained at 500 ºC. In the sample prepared at 450 ºC a contamination of rhombohedral (R-3c) $V_2O_3$ was observed and marked by asterix over the pattern. $V_2O_3$ was formed because of same incorporation of oxygen during the synthesis of VN. Compared with the same reactions carried out in $LiNH_2$, here the formation of crystalline VN occurred at higher temperatures.

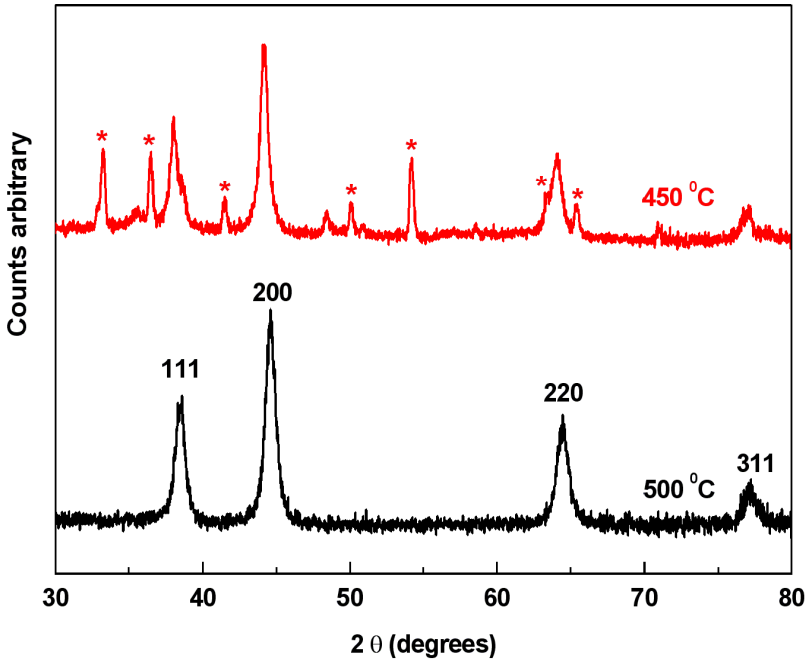


**Figure 4.12** XRD patterns of the products of reaction of $VCl_3$ with $NH_3$ heated for 24 h. Miller indices mark the VN peaks. $V_2O_3$ reflections in the 450 ºC sample are marked by asterix.

Use of ammonia increased the carbon contents of these materials significantly compared with reacting the same chlorides with $LiNH_2$. This carbon can only be due to solvent decomposition.

The reaction of $VCl_3$ with ammonia or $LiNH_2$ produced similar products in terms of lattice parameters and particle sizes, but the carbon content with $NH_3$ was high, corresponding to a composition of $VN_{0.40}C_{0.38}$ at 500 ºC. The expansion in the lattice parameter in VN produced from $LiNH_2$ is also found in these materials.

**Table 4.2.** Products of reactions of metal (group 5) halides with $NH_3$ heated for 24 h in benzene.

| Halide | T/°C | Product/s (lattice parameters in Å) | Size (nm) | % C, N | Composition |
|---|---|---|---|---|---|
| $VCl_3$ | 450 | VN (a = 4.124(2)) | 10 | | |
| | 500 | VN (a = 4.1267(10)) | 12 | 7.5, 9.1 | $VN_{0.4}C_{0.38}$ |
| $NbCl_5$ | 400 | Amorphous | | | |
| | 450 | NbN (a = 4.301(4)) + some amorphous | 6 | 1.2, 9.6 | $NbN_{0.71}C_{0.10}$ |
| | 500 | NbN (a = 4.320(2)) | 4 | 10.4, 10.8 | $NbN_{0.90}C_{1.02}$ |
| | 550 | NbN (a = 4.373(2)) | 5 | 26.6, 9.4 | $NbN_{0.97}C_{3.22}$ |
| $TaCl_5$ | 450 | Amorphous | | | |
| | 500 | $Ta_3N_5$ (a = 3.898(3), b = 10.247(9), c = 10.265(8)) | 9 | 0.6, 7.5 | $Ta_3N_{3.15}C_{0.29}$ |
| | 550 | $Ta_3N_5$ (a = 3.910(2), b = 10.257(12), c = 10.310(10)) | 10 | 15.5, 8.2 | $Ta_3N_{4.15}C_{3.05}$ |

TEM images (Fig. 4.13) showed isotropic particles of around 10 nm diameter, again matching closely the PXD derived crystallite size.

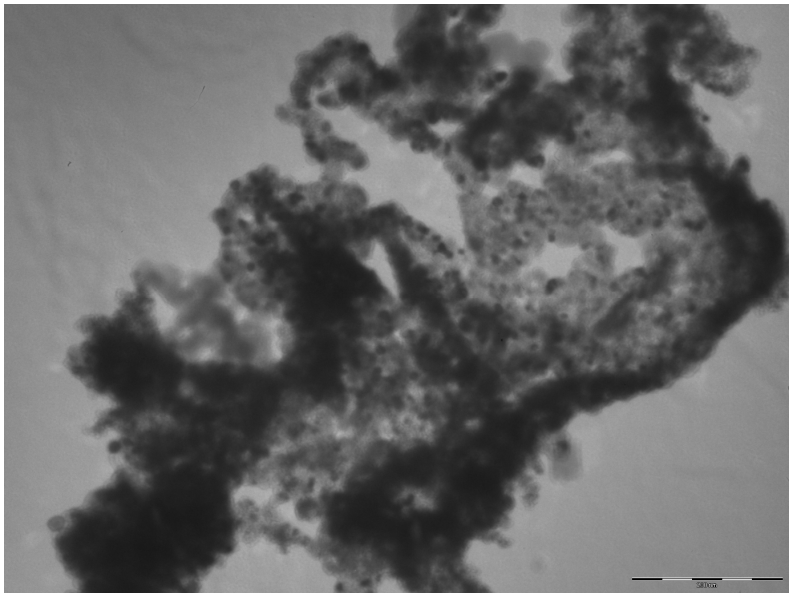

**Figure 4.13** TEM images of VN synthesised from $VCl_3$ and $NH_3$ at 550 ºC.

TGA of VN carried out under nitrogen ( Fig. 4.14 b) shows a mass loss (~10 %) up to 720 ºC due to the presence of surface amide groups while at higher temperature the mass loss is attributed to the elimination of $NH_3$ and $N_2$.

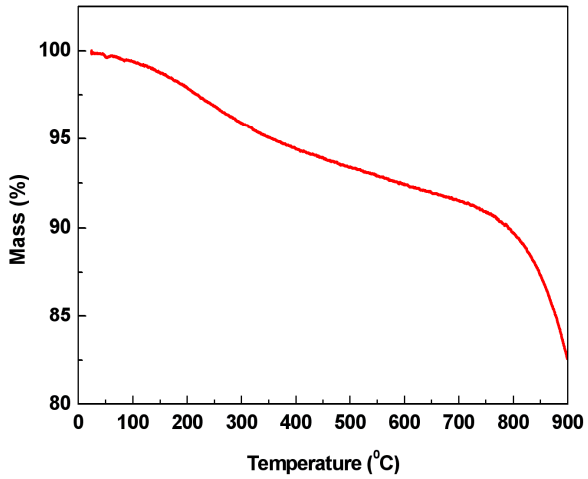


**Figure 4.14** TGA under nitrogen of VN produced in $NH_3$ at 500 ºC.

SEM images of VN (Fig 4.15 a) do not provide information regarding the morphology of the particles but were used to study the surface of the materials. Images of unground samples revealed porous structures indicating likely high surface area. EDX (Fig. 4.15 b) shows small amount of chlorine (less than 1 %) as an impurity in the sample presumably due to incomplete elimination after washing with methanol.

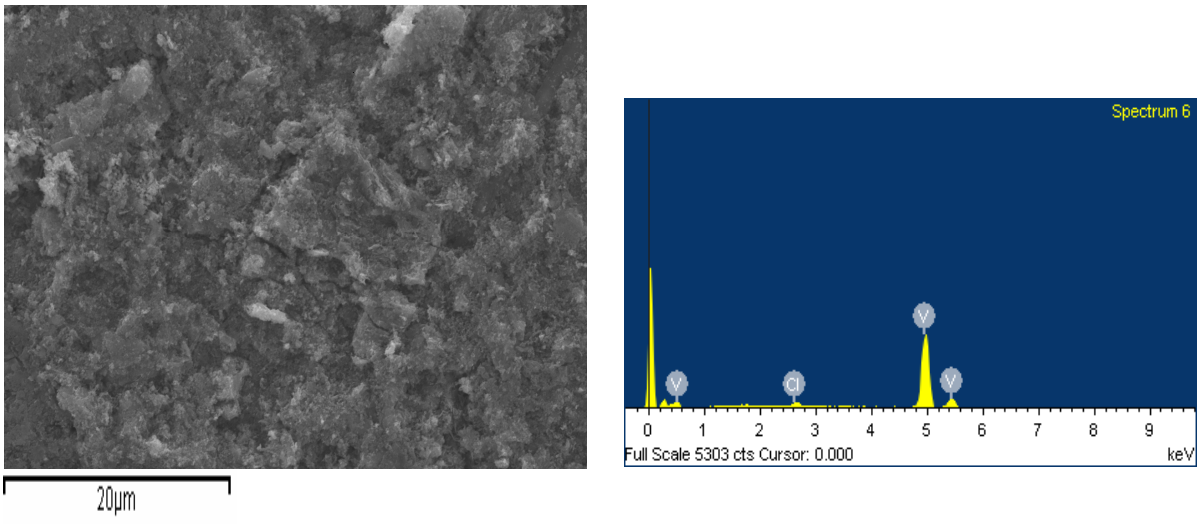


**Figure 4.15** a) SEM image of VN prepared at 550 ºC and b) EDX data.

### 4.3.2 Reactions of $NbCl_5$ with $NH_3$

These reactions proceed in a similar way to those described for vanadium nitrides. The first step involves the formation of niobium amide through sequential substitutions of chloride groups. The number of moles of $NH_4Cl$ byproduct formed depends from the number of chlorine replaced in the niobium chloride. Considering a complete substitution, the reaction can be written as follow:

$$NbCl_5 + 10\ NH_3 \longrightarrow \text{“}Nb(NH_2)_5\text{”} + 5\ NH_4Cl$$

The subsequent condensation during heat treatment leads to the transformations of the niobium amide in NbN with production of $NH_3$ and $N_2$:

$$\text{“}Nb(NH_2)_5\text{”} \longrightarrow NbN + {}^{10}/_{3}\ NH_3 + {}^{2}/_{3}\ N_2$$

The formation of NbN involves the reduction of niobium from its +5 oxidation state to +3.

Fig. 4.16 shows the XRD patterns of the as prepared NbN samples. There are 4 diffraction peaks at different d-spacing indexed as cubic NbN. The influence of the reaction temperature on the formation of nanocrystalline niobium nitride was investigated. It was found to be fully crystallised at 550 and 500 ºC (Fig. 4.16). If the reaction temperature was lower than 450 °C nanocrystalline NbN could not be obtained. The materials prepared at different reaction temperatures revealed particle sizes ranging from 4 to 6 nm. In these samples a trend of the carbon content increasing with reaction temperature is strongly observed. The lattice parameter is low at 500 ºC, similarly to those in Table 4.2, but is closer to the normal range at 550 ºC. Presumably at least some of the carbon is going into the lattice and this is responsible for the increase in the lattice parameter, though at 550 ºC the total composition is $NbN_{0.97}C_{3.21}$ so the bulk of the carbon is expected to be present in an elemental form.

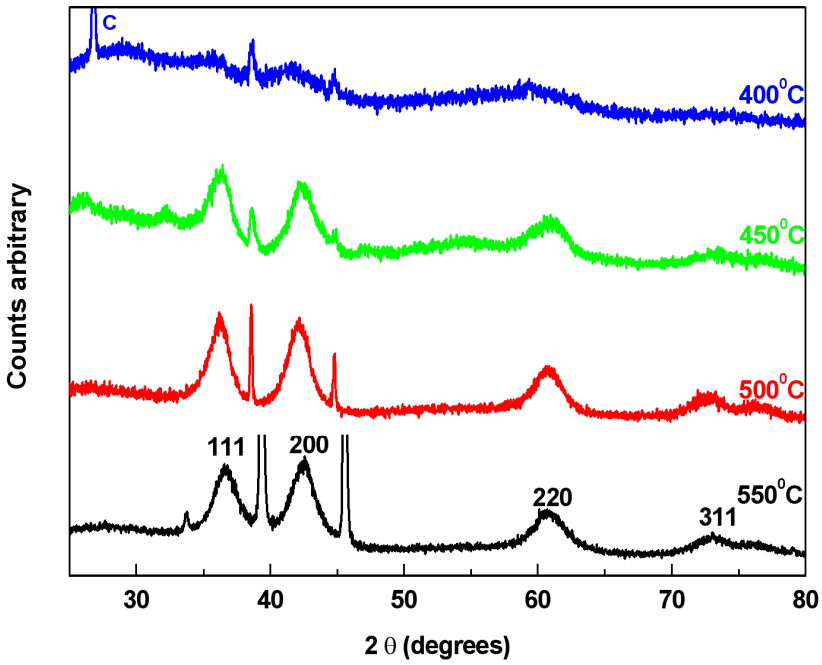


**Figure 4.16** XRD patterns of NbN produced from $NbCl_5$ with $NH_3$ at different reaction temperatures. Two aluminium peaks resulting from the sample holder are visible in all data sets at 2θ = 38º and 44º.

TEM image (Fig 4.17) of the samples prepared at 550 ºC shows small spherical particles with average diameter of 2-3 nm matching closely with the size particles derived by XRD data. The aggregation of these small crystallites was clearly observed in various areas of the samples.

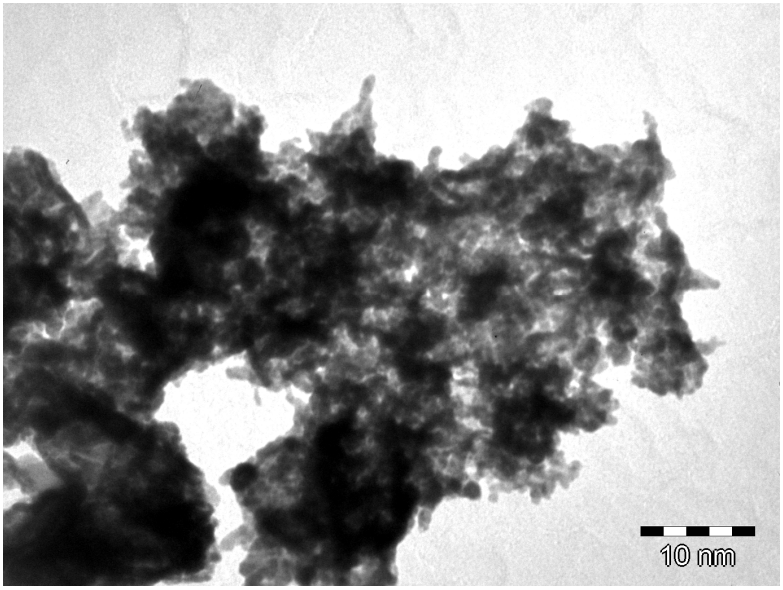


**Figure 4.17** TEM image of NbN synthesised from $NbCl_5$ and $NH_3$ at 550 ºC.

### 4.3.3 Reactions of $TaCl_5$ with $NH_3$

The preparation of $Ta_3N_5$ from $TaCl_5$ and $NH_3$ was previously achieved using solid state reaction at temperature over 1000 °C. $Ta_3N_5$ was also prepared from the reaction of $Ta_2O_5$ with $NH_3$ at various temperature (680-900 °C) and heating time (2-120 h)[30]. samples as prepared revealed by combustion analysis low carbon and hydrogen content (less than 0.1 %). Nitrogen and oxygen content were found depending from the reaction temperature and time. Sample prepared at 680 °C for 8 h contained amorphous material and anion rich composition ($Ta_3N_{3.99}O_{3.36}$). Crystalline $Ta_3N_5$ with composition $Ta_3N_{4.67}O_{0.23}$ was obtained by heating the starting material at 900 °C for 5 days. Sample prepared at higher temperature were found anion deficient. Aggregated products were formed using these reactions and the products were oxygen contaminated also after long heating time. Other work reported that controlled ammonolysis of nanocrystalline $Ta_2O_5$ yielded crystalline $Ta_3N_5$ at temperature of 660 °C[34-36].

In this study the reactions of $TaCl_5$ with ammonia were employed to determinate whether it could be achieved under solvothermal conditions. The reactions proceed as those described for niobium chloride:

$$TaCl_5 + 10\ NH_3 \longrightarrow \text{“}Ta(NH_2)_5\text{”} + 5\ NH_4Cl$$

$$3\ \text{“}Ta(NH_2)_5\text{”} \longrightarrow Ta_3N_5 + 10\ NH_3$$

In this system the tantalum oxidation state (+5) is maintained hence no $N_2$ is evolved. The samples were prepared at temperatures in the range 550-450 °C. PXD patterns (Fig. 4.18) show the evolution of $Ta_3N_5$ with the temperature.

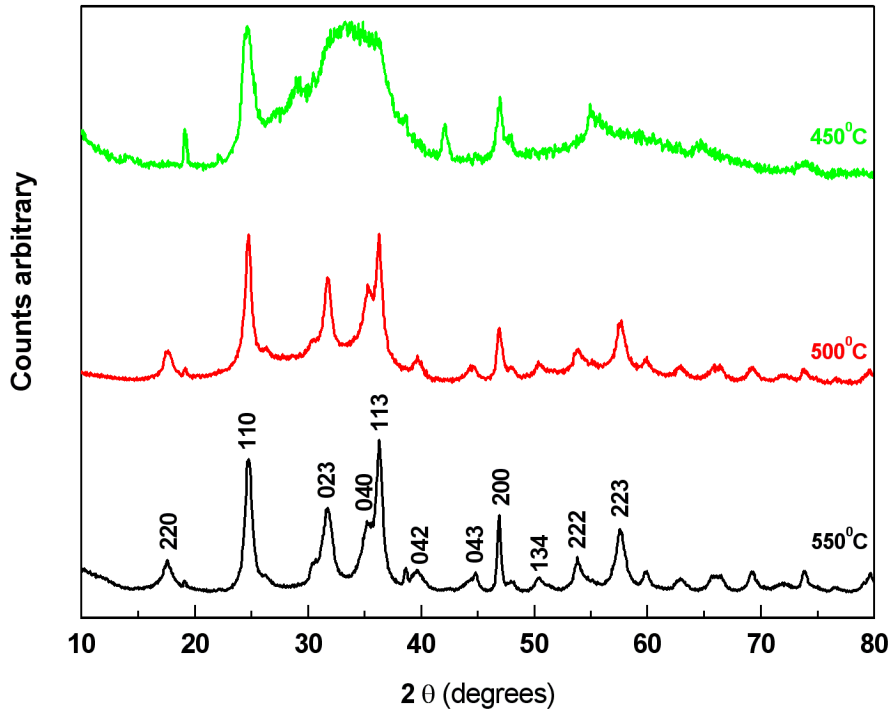


**Figure 4.18** XRD patterns of the products from $TaCl_5$ and $NH_3$ at different temperatures.

PXD patterns (Fig. 4.18) matched $Ta_3N_5$ at 550 ºC whereas a mixture of amorphous and crystalline material was prepared at 450 ºC.

The crystallization of $Ta_3N_5$ with ammonia followed a similar trend to that with $LiNH_2$-crystalline products obtained at 500 °C and above. The refined crystallite sizes (~ 9 nm) were smaller with ammonia, (Table 4.2) but samples from both routes were nitrogen deficient to a similar extent. Refinement of the PXD pattern obtained after synthesis at 550 °C initially yielded a poor fit. However, inclusion of the anisotropy coefficient (the stec parameter in GSAS profile function 2) into the Lorentzian broadening yielded a good fit with lattice parameters of a = 3.910(2), b = 10.257(12) and c = 10.310(10) Å. The most obvious effect was to fit a strong 200 reflection that was sharper than other peaks. This will be discussed later in the context of the TEM data. The lattice parameters at 550 °C are also slightly higher than typical literature values of a = 3.89, b = 10.22 and c = 10.28 Å[30], or values obtained in this study and elsewhere[31, 33] suggesting an effect of carbon incorporation into the lattice of these samples.

$Ta_3N_5$ samples were found to consist almost entirely of high aspect ratio nanorods. Fig. 4.19 shows a sample of ~5 × 100 nm rods produced at 550 °C. These were found to exhibit lattice fringes running along the length of the rods that confirmed them to be single crystalline. Their lattice spacings correspond to the (110) or (022) planes of $Ta_3N_5$. The preferred growth component observed in the 200 peak during fitting of the PXD data suggests the fringes to be attributable to (110) planes.

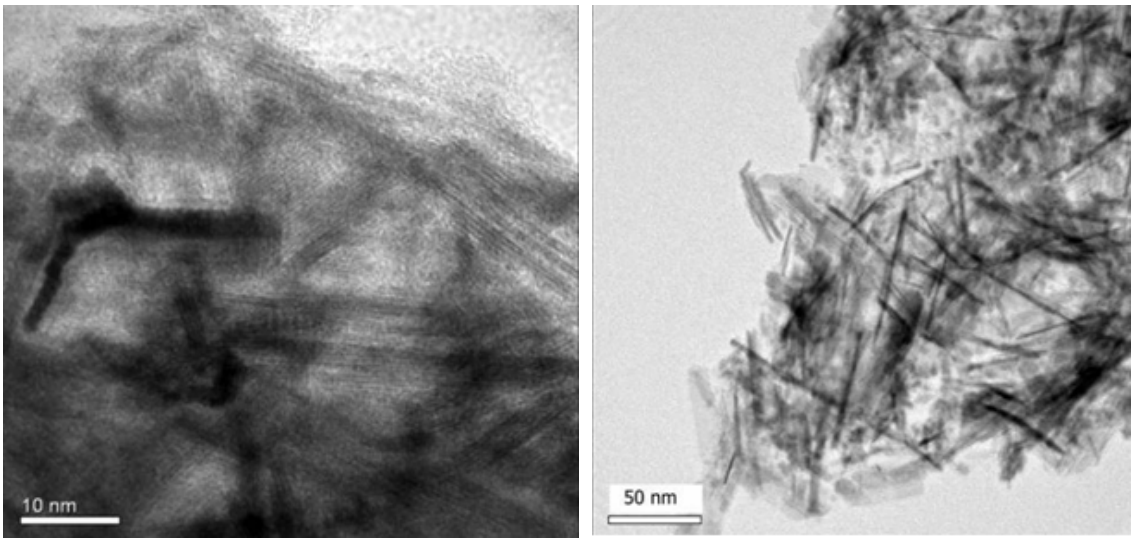


**Figure 4.19** TEM images of $Ta_3N_5$ nanorods grown from $TaCl_5$ and $NH_3$ at 550 ºC.

The TGA profile (Fig. 4.20) in oxygen shows a mass loss (~10 %) between 400 and 580 ºC showing the presence of elemental carbon in the system. The C content is disappointing since little solvent charring was observed under these conditions with $LiNH_2$. The amount of tantalum (~74 %) was calculated from the conversion of $Ta_3N_5$ in $Ta_2O_5$ formed at high temperature in oxygen atmosphere.

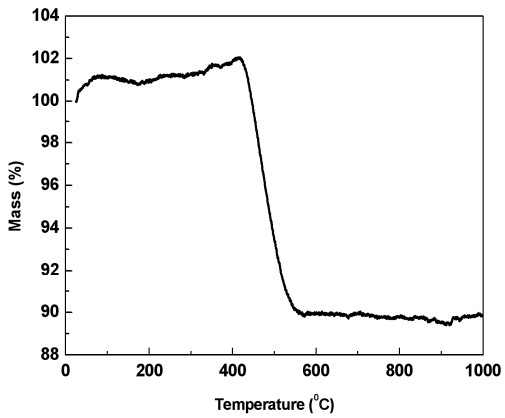


**Figure 4.20** TGA under oxygen of $Ta_3N_5$ produced from $TaCl_5$ with $NH_3$ at 550 ºC.

# 4.4 Experimental

Preparations were carried out under anaerobic conditions using either glove box or Schlenk line techniques for sample loading and handling. Benzene was distilled from Na and $CH_3OH$ from $NaOCH_3$. $VCl_3$ (97%), $NbCl_5$ (99.999%), $TaCl_5$ (99.999%) were purchased from Aldrich and used as supplied. Ammonia (Air Products) was distilled from a sodium/ammonia solution before use. $LiNH_2$ was synthesised by reacting 1.6 M $^nBuLi$ in hexane (Aldrich) with excess distilled ammonia at -78 ºC, filtering, and drying the product under vacuum.

All synthesis was performed in a 75 $cm^3$ autoclave (Parr 4740CH). Typically, 0.6 g of metal chloride was placed in the silica liner and covered with 15 $cm^3$ of benzene. Either a stoichiometric amount of $LiNH_2$, calculated to balance the lithium and chloride components of the reaction mixture, or a 10-fold molar excess of ammonia, was added. The autoclave was heated at temperature between 250-550 °C, typically for 24 h. After cooling to room temperature, the autoclave was opened and the mixture was transferred to a Schlenk tube inside the glove box. The solid was collected by filtration, washed with dry methanol three times to remove LiCl or $NH_4Cl$ by-product, and dried under vacuum.

Powder X-ray diffraction (PXD) measurements were performed on a Siemens D5000 diffractometer using Cu $K_{\alpha_1}$ ($\lambda$ = 1.5406 Å) radiation. The phases present were identified by comparison with the JCPDS database[37] and patterns refined using the GSAS package[38, 39]. Crystallite sizes were extracted from the Lorentzian component of the profile coefficients as described in the GSAS manual[38, 39]. Transmission electron microscopy (TEM) was carried out with a Hitachi 7000 (75 kV) microscope at the Biomedical Imaging Unit, Southampton General Hospital or a Jeol JEM3010 microscope with an Oxford Inca EDX detector. Samples were prepared by ultrasound dispersal in toluene, followed by deposition on carbon-coated Cu grids. C, H, N combustion analyses were carried out by Medac Ltd. (Egham, Surrey, UK). Scanning electron microscopy (SEM) was performed in a Jeol JSM5910 microscope with an accelerating voltage of 10 kV. Thermogravimetric analyses (TGA) were performed in a mettle Toledo TGA/SDTA851e instrument under flowing BIP nitrogen or 60 % $O_2$-40 % $N_2$ from 25° to 1000 °C at a rate of 10 °/min.
Infrared spectroscopy was performed on CsI disks using a Perkin Elmer Spectrum One FT-IR spectrometer. Diffuse reflectance UV-vis spectra were collected using a Perkin Elmer Lambda 35 spectrometer with an integrating sphere in the range of 400-800 nm.

# 4.5 Conclusions

Reactions of $VCl_3$, $NbCl_5$ and $TaCl_5$ with $LiNH_2$ and $NH_3$, in benzene, under solvothermal conditions at high temperatures produced nanocrystalline metal nitrides (VN, NbN, and $Ta_3N_5$).

As noted in the introduction vanadium nitrides are the most interesting in group 5 for catalysis[7, 8] and it was synthesized solvothermally in a pure rocksalt phase.

In the case of $Ta_3N_5$ it was obtained directly under solvothermal conditions. This was surprising since the analogous solid state reaction produced cubic TaN[17].

In this work was observed that when $VCl_3$ was used, the reactions in $LiNH_2$ occurred at moderate temperature (250 ºC) whereas with $NbCl_5$ and $TaCl_5$ higher temperature of 550 or 550 ºC were required to crystallise the products. In the formation of vanadium nitrides the vanadium oxidation state (+3) is maintained and less reorganization may be required to make the corresponding nitrides and this could affect the crystallization temperature. One consequence of these reaction temperatures was solvent decomposition and incorporation of carbon into the samples. These were also nitrogen deficient compared with the stoichiometric phase and generally the samples produced could be considered as carbonitrides. From an application viewpoint, this is not necessarily a problem as the equivalent carbides are also active catalysts. The variation by metal suggested a catalytic effect in the solvent decomposition. In fact no carbon was found when benzene was heated to 550 ºC in the same autoclave with no ammonia or metal salts. Carbon content was generally found to be much higher when $NH_3$ was the nitrogen sources, implicating the ammonia in the process of benzene decomposition.

Moreover the nitrides produced using ammonia as nitrogen source, showed smaller particle size compared with the same reactions in $LiNH_2$. In the first case, the materials gave broad PXD peaks and at low temperature an amorphous material was achieved. This may be due to worse heat transfer in these reactions.
TEM of the samples typically showed isotropic particles, which were fairly aggregated and had individual crystallites of similar size to those, obtained from the PXD linewidths.

Only in $Ta_3N_5$ case, nanorods particles were obtained. The growth of nanorods was surprising, only $NH_4Cl$ could potentially be present acting as a flux.

Solvothermal conditions were clearly effective in moderating the exothermicity of these reactions, but nitrogen deficient compositions were still obtained in many of the cases studied.

# 4.6 References


1. L. E. Toth, *Transition Metal Carbides and Nitrides, Academic Press, New York*, 1971.
2. A. W. Weimer, *Carbides, Nitrides, and Boride Materials Synthesis and Processing. Chapman & Hall, London, 1997*.
3. O. I. Shulishova, *Superconductivity and the Nature of the Bond in Carbides and Nitrides of Transition Metals and their Solid Solutions with the NaCl Structure, Fiz. Tverd. Ttela*, 1996, p. 299.
4. T. Y. Kosolapova, *Handbook of High Temperature Compounds: Properties, Production, Application. Hemisphere Publishing Corp., New York, 1990.*
5. A. Marouchkine, *Room Temperature Superconductivity, Cambridge International Science Publishing Chippenham, 2004*.
6. S. E. Dann, *Reactions and Characterization of Solids, RSC, Exeter, 2000.*
7. H. Kwon, S. Choi and L. Thompson, *J. Catal.*, 1999, **184**, 236.
8. S. T. Oyama, *Catal. Today*, 1992, **15**, 179.
9. C. C. Agrafiotis, J. A. Puszynski and V. Hlavacek, *J. Am. Ceram. Soc.*, 1991, **74**, 2912.
10. R. Riedel, *Handbook of Ceramic Hard Material, Ed., Wiley*, 2000.
11. M. Ritala, P. Kalsi, D. Riihela, K. Kukli, M. Leskela and J. Jokinen, *Chem. Mater.*, 1999, **11**, 1712.
12. J. S. Becker, S. Suh, S. Wang and R. G. Grodon, *Chem. Mater.*, 2003, **15**, 2969.
13. C. M. Fang, E. Orhan, G. A. de-Wijs, H. T. Hintzen, R. A. de-Groot, R. Marchand, J.-Y. Saillard and G. de-With, *J. Mater. Chem.*, 2001, **11**, 1248.
14. K. J. Lee and H. S. Yang, *Jps. Patent 2001237399*, 2001.
15. O. Merdrignac-Conanec, M. Kerlau, M. Guilloux-Viry, R. Marchand, N. Barsan and U. Weimar, *Silc. Ind.*, 2004, **69**, 141.
16. A. Jain and K. Lucas, *US Patent 5741626, 1998*.
17. I. P. Parkin and A. T. Rowley, *J. Mater. Chem.*, 1995, **5**, 909.
18. A. L. Hector and I. P. Parkin, *Chem. Mater.*, 1995, **7**, 1728.
19. A. L. Hector and I. P. Parkin, *Polyhedron*, 1995, **14**, 913.
20. A. L. Hector and I. P. Parkin, *J. Chem. Soc., Chem. Commun.*, 1993, 1095.
21. J. Ma, Y. Du and Y. Qian, *J. All. and Cmpds.*, 2005, **389**, 296.
22. Y. Gu, F. Guo, Y. Qian, H. Zheng and Z. Yang, *Mater. Lett.*, 2003, **57**, 1679.

23. J. Hu, Q. Lu, K. Tang, B. Deng, R. Jiang, Y. Qian, G. Zhou and X. Liu, *Chem. Lett.*, 2000, **29**, 74.
24. Y. Xie, Y. Qian, W. Zhang, S. Zhang and Y. Zhang, *Science*, 1996, **272**, 1926.
25. J. Choi and E. G. Gillan, *Inorg. Chem.*, 2005, **44**, 7385.
26. J. C. Fitzmaurice, A. L. Hector and I. P. Parkin, *J. Chem. Soc. Dalton Trans.*, 1993, 2435.
27. *Inorganic Crystal Structure Database accessed via "The United Kingdom Chemical Database Service" D. A. Fletcher, R. F. McMeeking and D. Parkin, J. Chem. Inf. Comput. Sci.*, 1996, **36**, 746.
28. W. Lengauer and P. Ettmayer, *Monatsh. Chem.*, 1986, **117**, 713.
29. S. Akyüz and J. E. D. Davies, *J. Mol. Struct.*, 1982, **95**, 157.
30. S. J. Henderson and A. L. Hector, *J. Solid State Chem.*, 2006, **179**, 3518.
31. B. Mazumder, P. Chirico and A. L. Hector, *Inorg. Chem.*, 2008, **47**, 9684.
32. M. Jansen, E. Guenther and H. P. Letschert, *German patent 199 07 618.9*, 1999.
33. B. Mazumder and A. L. Hector, *J. Mater. Chem.*, 2008, **18**, 1392.
34. G. Hitoki, A. Ishikawa, T. Takata, J. N. Kondo, M. Hara and K. Domen, *Chem. Lett.*, 2002, **7**, 736.
35. M. Hara, G. Hitoki, T. Takata, J. N. Kondo, H. Kobayashi and K. Domen, *Catal. Today*, 2003, **78**, 555.
36. A. Rugge, J. S. Park, R. G. Gordon and S. H. Tolbert, *J. Phys. Chem. B.*, 2005, **109**, 3764.
37. *PCPDFWIN, version 2.4; Powder Diffraction File, International Center for Diffraction Data: Swarthmore, PA*, 2003.
38. A. C. Larson and R. B. Von-Dreele, *General Structure Analysis System (GSAS), Los Alamos National Laboratory report LAUR*, 2004, 86-748.
39. B. H. Toby, *J. Appl. Crystallogr.*, 2001, **34**, 210.

# 5.1 Introduction

Group 6 nitrides (e.g. CrN, MoN and WN) are characterised by chemical instability and the compounds are not generally considered to be refractory because of their rapid dissociation to $N_2$ and the pure element at high temperature[1]. They become progressively less stable in the order Cr to Mo to W[1].

The known phases in the Cr-N system are β-$Cr_2N$ and δ-$CrN_{1-x}$[2] The atomic position of the Cr atoms is h.c.p. with the nitrogen atoms distributed in the interstitial voids corresponding to the ε-$Fe_2N$-type structure[2]. δ-$CrN_{1-x}$ has the NaCl type structure[2]. CrN is paramagnetic at room temperature while at temperatures below 276-286 K (depending on the composition[2]) it exhibits antiferromagnetic properties[2]. CrN coatings have a friction coefficient slightly lower than that of TiN and in the case of hot corrosion resistance CrN coatings exhibit superior properties to TiN[3, 4]. They found applications also as optical and decorative coatings[5, 6]. CrN has been previously obtained[7] under solvothermal conditions from the reaction of $CrCl_3$ with $Li_3N$ in benzene. Nanocrystalline CrN with average size about 25 nm was prepared in the temperature range of 350-420 ºC. The as-prepared products contained a small amount of amorphous carbon probably due to the carbonization of benzene.

Molybdenum nitrides are among the most studied nitrides in the field of catalysis. In general, these nitrides are rather unstable and decompose at moderate temperatures. The known phases in the Mo-N system include: β-$Mo_2N$ (tetragonal structure), γ-$Mo_2N$ (face-centred cubic structure) and δ-MoN (hexagonal structure). δ-MoN was first synthesized by Hagg[8] by the reaction of Mo metal power with flowing ammonia. This phase is superconducting and its transition temperature is around 15 K[9]. Although it has not been prepared with a stoichiometric composition γ-$MoN_{1.00}$ has been predicted in theorical studies to have a $T_c$ of up to 30 K[2]. γ-$Mo_2N$ has catalytic activity for CO hydrogenation[10-12], $C_2H_6$ hydrogenation[10, 11], $CO_2$ methanation[13], hydrodesulfurization[14], and $NH_3$ synthesis[15].

Molybdenum nitrides have been typically synthesized from the reaction of Mo metal or Mo oxides with nitrogen or ammonia[16-19]. These reactions require long reaction time and in the case of $N_2$ high nitrogen pressures. The preparation of γ-$Mo_2N$ from $MoO_3$ under ammonia flow led to products with large specific area. The main issue with this synthetic approach was the presence of large amount of oxygen in the final products. The use of high reaction temperature reduced this contamination but then the resulting molybdenum nitride contained molybdenum metal because of thermal

decomposition. Moreover high temperature increased the grain size and the specific area was reduced with a consequent detrimental effect on the catalytic properties. In order to avoid the presence of oxygen in molybdenum nitrides, oxygen free precursors such as $MoCl_5$ need to be used. The reactions from $MoCl_5$ with flowing ammonia were investigated at temperature of 770-1060 K[20]. In this work, single phase WC type δ-MoN was obtained up to 910 K, while at higher temperature a mix of δ-MoN and γ-$MoN_{1-x}$ were found in the final products. Moreover only the lattice parameter of γ-$MoN_{1-x}$ were depending on the reaction temperature. By increasing the temperature γ-$MoN_{1-x}$ was the main phase in the product and its lattice parameter was decreased. Ammonolysis reactions of $MoS_2$ were also studied[21] leading to a nitrogen rich phase $Mo_5N_6$ prepared at ~750 ºC while a pure δ-MoN was obtained at higher temperature (~850 ºC).

The main phases of tungsten nitrides are β-$W_2N$ and δ-WN[1]. δWN was prepared from the reaction of W powder in $NH_3$ at temperature lower than 800 ºC[8, 22]. These nitrides are unstable at high temperature and this is reflected in a paucity of reports on these materials. Tungsten nitrides have applications as stable thin film resistors and diffusion barrier of metals in electronic devices[23].

Solid state reactions of $CrCl_3$, $MoCl_3$ , and $WCl_4$ with lithium amide have been used to prepare metal nitrides[24]. The reactions of $CrCl_3$ with $LiNH_2$ yielded a mixture of hexagonal $Cr_2N$ and cubic CrN while for molybdenum a mixture of cubic $Mo_2N$ and molybdenum metal was achieved. The reactions of $WCl_4$ with $LiNH_2$ led to the formation of cubic $W_2N$. Thermally initiated reactions led to amorphous products and in order to produce crystalline metal nitrides they were crystallised at 700-800 ºC for 1-2 h. The crystallite size of the nitride prepared was 20-30 nm. The solid-state metathesis reactions of metal chlorides ($CrCl_3$, $CrCl_2$, $MoCl_3$ ,$MoCl_5$ and $WCl_4$) with $Li_3N$ have been reported[25]. In the reaction of $CrCl_3$ with $Li_3N$ only Cr with minor phase $Cr_2N$ (typically less than 20 %) was obtained. Using $CrCl_2$ a mixture of $Cr_2N$ and Cr was always obtained, but in this case the minor phase was Cr. The reactions of molybdenum halides ($MoCl_3$ and $MoCl_5$) and $Li_3N$ yielded Mo+$Mo_2N$ (minor phase) with $MoCl_3$ and Mo with $MoCl_5$. This result showed that metal halides in lower oxidation state were more likely to produce metal nitride. The reactions were less exothermic and the decomposition temperature of metal nitride prepared was less likely to be reached. Only tungsten was achieved from the reaction of $WCl_4$ and lithium nitride. The reaction of $WCl_6$ and $Na_3N$ yielded a mix of W+$W_2N$ whereas the reactions of $CrCl_2$ and $MoCl_3$ with $Na_3N$ yielded Cr+$Cr_2N$ and Mo+$Mo_2N$, respectively[26]. The high temperature was responsible of the decomposition of metal nitride and formation of dinitrogen and metal. These results show that the solid state reactions achieve temperatures too high for effective group 6 nitride formation.

In order to reduce the temperatures reached in these exothermic reactions, solvothermal condition were used in this work. Molybdenum and tungsten nitrides have been synthesised solvothermally for the first time herein.

# 5.2 Reactions of $CrCl_3$, $MoCl_5$ and $WCl_4$ with $LiNH_2$

The main aim of this work was to study the reactions of transition metal chlorides ($CrCl_3$, $MoCl_5$, $WCl_4$) with lithium amide and ammonia under solvothermal conditions in benzene up to 550 °C.

## 5.2.1 Reactions of $CrCl_3$ with $LiNH_2$

Nanocrystalline CrN was synthesised from the reaction of $CrCl_3$ and $LiNH_2$ in benzene at temperatures in the range 300–550 °C. This reaction can be described as follows:

$$CrCl_3 + 3\ LiNH_2 \xrightarrow{\text{benzene}} CrN + 3\ LiCl + 2\ NH_3$$

Fig. 5.1 shows the PXD patterns of all samples produced. The main reflection positions marked by Miller indices over the pattern at 550 ºC, indicated the formation of cubic chromium nitride (Fm-3m). A secondary phase identified as hexagonal $Cr_2N$ (P-31m) was also observed at 400 and 550 ºC.

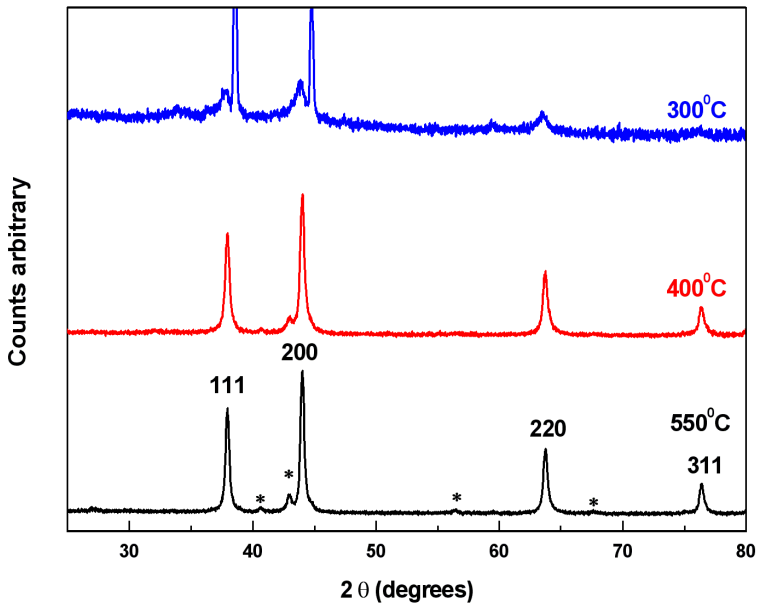


**Figure 5.1** PXD patterns of chromium nitride produced at 300 (top), 400 (middle) and 550 ºC (bottom). Miller indices mark the CrN reflections, those of $Cr_2N$ are marked by asterix. Two truncated aluminium peaks resulting from the sample holder are visible in the 300 ºC dataset at 38 and 44º.

The evolution of this secondary phase was examined by carrying out reactions for a shorter time period, 5h, and no $Cr_2N$ was found at 550 ºC (Fig. 5.2). CrN has poor thermal stability and the growth of $Cr_2N$ with a longer reaction time is thus due to thermal decomposition of the product. The peak width at 550 ºC was similar to that after 24 h, suggesting similar particle sizes. At 400 ºC the shorter heating period resulted in significantly broader diffraction peaks.

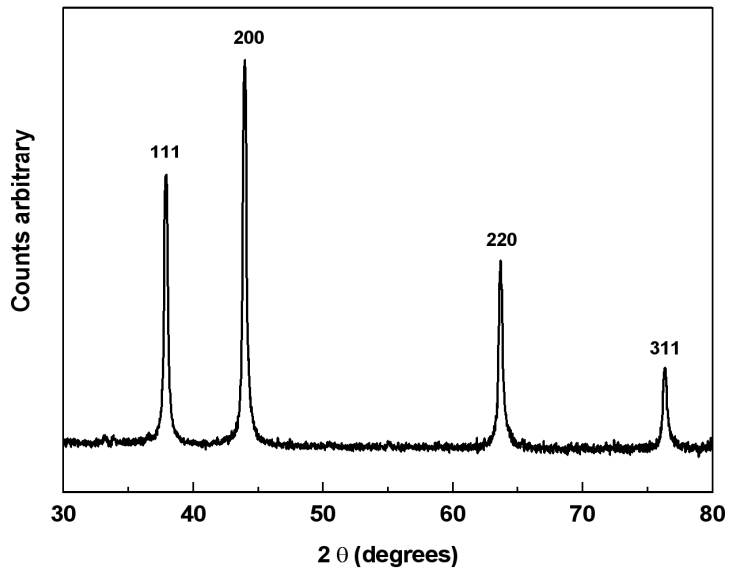


**Figure 5.2.** PXD pattern of CrN produced from $CrCl_3$ and $LiNH_2$ at 550 °C for 5h.

In the formation of CrN it can be observed that the chromium oxidation state (+3) is maintained. Similarly to the preparation of VN (discussed in chapter 4) the crystallization of the metal nitrides occurred at temperature as low as 300 ºC. Because both metals are initially already in the oxidation state + 3, less reorganization may be required to make the corresponding nitrides and this could affect the crystallization temperature.

The production of chromium nitrides was previously investigated using a thermally-initiated solid state metathesis of $CrCl_3$ with $Li_3N$ at temperature of 400 ºC for a period ranging from a few seconds to five minutes[25]. These reactions yielded a mix of Cr + $Cr_2N$. Hexagonal $Cr_2N$ with the same lattice parameter reported in literature (a= 4.17 and c= 4.44 Å) was present in the final product as minor phase. $Cr_2N$ was the main phase when $CrCl_2$ was reacted with $Li_3N$. Use of $CrCl_2$ with oxidation state (+2) reduced the amount of chromium metal in the products, but did not eliminate it entirely[25]. In the reactions of $CrCl_2$ with $NaN_3$ a mix of Cr metal (major phase) and hexagonal $Cr_2N$ were observed in the final material[26]. The products were less crystalline compared with the reactions carried out in $Li_3N$. Reactions of $CrCl_3$ with $LiNH_2$ at 160-400 ºC led

initially to an amorphous material which was crystalline after thermolysis at 700 ºC for 1-2 h[24]. A mixture of $Cr_2N$ and CrN was observed. These methods were successful in the preparation of early transition metal nitrides, but the high exothermicity of these reactions and the low chemical stability of CrN usually led to metal contamination and the hexagonal $Cr_2N$ was usually the main phase of the materials.

The main phase of CrN prepared under solvothermal conditions in this work was cubic CrN with traces of hexagonal $Cr_2N$. Pure cubic CrN was formed at shorter reaction time (5 h). Under solvothermal conditions the reactions are just as exothermic but part of the heat evolved during the reactions can be absorbed into the solvent and hence the decomposition temperature of the metal nitride formed is less likely to be reached.

Stoichiometric CrN contains 21.2% N and the compositions obtained were non-stoichiometric. The highest N content (17.1 %) was observed in the sample prepared at 400 ºC (Table 5.1). The particle sizes calculated by Rietveld refinement was ranging from 6 to 25 nm at temperatures in the range 550-300 ºC. The reported lattice parameters for CrN range from 4.135-4.149 Å[27]. Higher parameters obtained here suggest some incorporation of carbon directly into the lattice.

**Table 5.1** Products of reactions of group 6 halides with $LiNH_2$ heated for 24 h in benzene.

| Halide | T/ºC | Product/s (lattice parameters in Å) | Size (nm) | % C, N | Composition |
|---|---|---|---|---|---|
| $CrCl_3$ | 300 | CrN (a = 4.1504(3)) + some amorphous | 6 | 1.8, 14.2 | $CrN_{0.63}C_{0.09}$ |
| | 400 | CrN (a = 4.1511(3)) + trace $Cr_2N$ | 21 | 2.2, 17.1 | $CrN_{0.79}C_{0.12}$ |
| | 550 | CrN (a = 4.167(4)) + trace $Cr_2N$ | 25 | 0.7, 14.9 | $CrN_{0.65}C_{0.03}$ |
| $MoCl_5$ | 450 | Amorphous | | 1.8, 8.8 | |
| | 550 | MoN (a = 4.106(4)) | 11 | 0.9, 9.2 | $MoN_{0.70}C_{0.08}$ |
| $WCl_4$ | 450 | WN (a = 4.077(15)) + some amorphous | 1.5 | 2.8, 6.8 | $WN_{0.99}C_{0.47}$ |
| | 550 | WN (a = 4.089(3)) | 2.4 | 0.9, 5.2 | $WN_{0.73}C_{0.15}$ |

Small particle sizes were observed by TEM. Figure 5.3 shows a distribution of particles of 8-10 nm in diameter and also aggregation of these small particles. PXD revealed larger crystallites of about 25 nm.

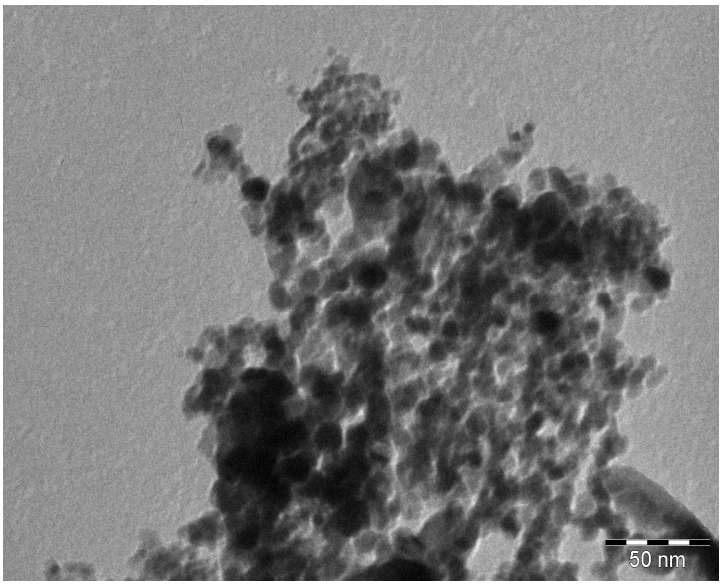


**Figure 5.3** TEM image of CrN prepared from $CrCl_3$ and $LiNH_2$ at 550 ºC.

The TGA profile (Fig. 5.4) of CrN under nitrogen shows a mass loss (~6.5 %) up to 700 ºC presumably due to the elimination of surface amide groups, at higher temperature the mass loss is due to the thermal decomposition of chromium nitride. However based on TGA analysis only is difficult to determinate the amide or imide groups present in the product.

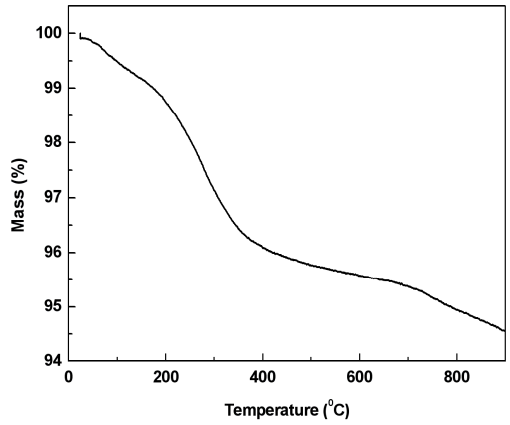


**Figure 5.4** TGA under nitrogen of CrN produced from $CrCl_3$ and $LiNH_2$ at 550 ºC with a 24 h heating time.

## 5.2.2 Reactions of $MoCl_5$ with $LiNH_2$

The formation of molybdenum nitride from $MoCl_5$ and $LiNH_2$ was investigated at temperatures in the range 450-550 ºC, through the following reaction:

$$MoCl_5 + 5\ LiNH_2 \xrightarrow{\text{benzene}} MoN + 10/3\ NH_3 + 1/3\ N_2 + 5\ LiCl$$

PXD patterns of the powder obtained are shown in Fig. 5.5. The five main broad diffraction peaks centred at around 2θ = 37.6, 43.6, 63, and 76 º corresponded to cubic γ $Mo_2N$ (Pm-3m). The peak broadening implied that the average crystallite size of the powder was small (Table 5.1).

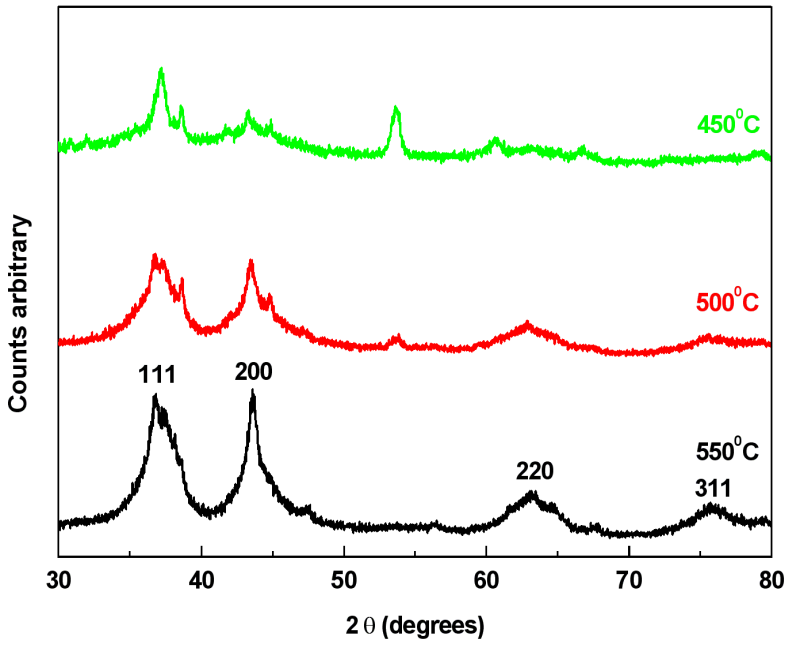


**Figure 5.5** XRD patterns of molybdenum nitride prepared from $MoCl_5$ and $LiNH_2$ [JCPDS 3-0907]. The peak at 53.6 ºof 2θ was $MoO_2$.Two aluminium peaks resulting from the sample holder are visible at 38 and 44 °.

MoN typically crystallises in a hexagonal structure[27], reports of rocksalt-structured material are comparatively recent. A theoretical study of MoN suggested a lattice parameter of 4.304[28] but the only structurally characterised samples were from high pressure preparations and have formulae of approximately $Mo_2N$[29, 30]. These were $Mo_2N_{0.92}$ (a = 4.161 Å) and $MoN_{0.56}$ (a = 4.162 Å) and simply have disordered N vacancies in the rocksalt-type lattice. MoN contains 12.7% N compared with 6.8% for $Mo_2N$, the product obtained at 550 ºC was somewhere between the two, with a composition of $MoN_{0.70}C_{0.08}$ if all the carbon was incorporated.

The lattice parameter was smaller than those from the high pressure reactions. The particle size calculated by Rietveld refinement in the diffraction pattern obtained at 550 ºC was 11 nm.

Previous methatetical reactions from $MoCl_5$ with $Mg_3N_2$ or $Ca_3N_2$ at temperature of 500 ºC led to the formation of Mo metal[31]. Use of $Li_3N$ as nitriding source yielded a mixture of Mo metal and $Mo_2N$ (minor phase)[25]. The reactions of $MoCl_5$ (the metal has higher oxidation state than $MoCl_3$) with $Li_3N$ did not produce molybdenum nitride presumably due to the higher exothermicity (more LiCl was produced) reached in these reactions. The formation of molybdenum nitride was also investigated from the reactions of $MoCl_5$ with $LiNH_2$ at temperature range of 160-400 ºC[24]. A thermolysis step at 700 ºC was required to prepare crystalline cubic $Mo_2N$, though Mo metal was found in the nitride formed. All these evidence show the potentiality of the solvothermal method in the preparation of nitrides with poor thermal stability.

TEM image (Fig. 5.6) shows the formation of a mixture of isotropic particles and 30-50 nm rods or tubes was obtained. The synthesis of molybdenum nitride involves the production of a meltable LiCl byproduct that does not have significant solubility in benzene and it is likely that the rods or tubes grow in this melted phase at the bottom of the reactor.

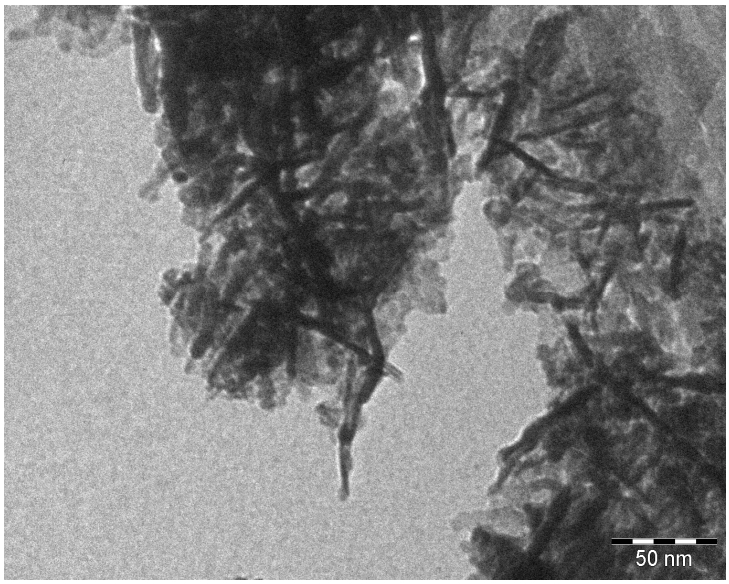


**Figure 5.6** TEM image of molybdenum nitride prepared from $MoCl_5$ and $LiNH_2$ at 550 ºC.

The TGA plot (Fig. 5.7) of $Mo_2N$ under nitrogen shows a weight change (~4 %) up to 700 ºC presumably due to the elimination of surface amide groups. The mass loss at temperature higher than 600 ºC is due to the decomposition of molybdenum nitride.

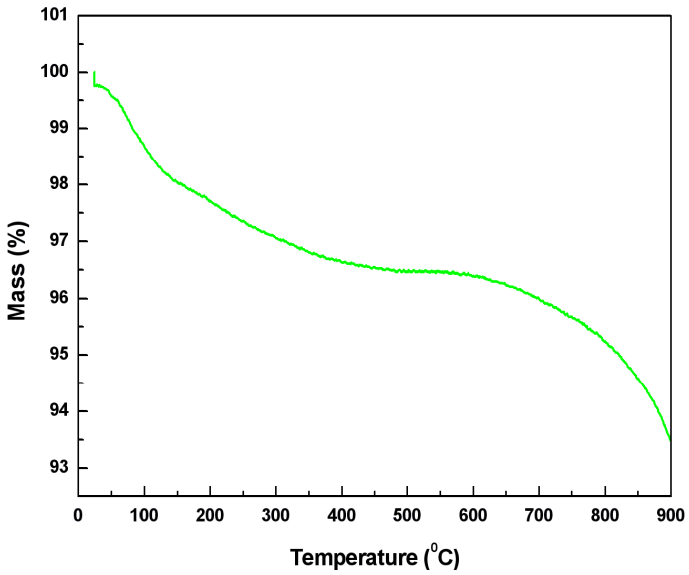


**Figure 5.7** TGA under nitrogen of $Mo_2N$ produced from $MoCl_5$ and $LiNH_2$ at 550 ºC.

## 5.2.3 Reactions of $WCl_4$ with $LiNH_2$

The formation of tungsten nitrides was investigated through the following reaction:

$$WCl_4 + 4\ LiNH_2 \xrightarrow{\text{benzene}} WN + 8/3\ NH_3 + 1/6\ N_2 + 4\ LiCl$$

Descending group 6 the metal nitrides become progressively less stable. Because of its thermal instability the preparation of pure tungsten nitride is often difficult to achieve. Solid-state reactions of $WCl_4$ with $Li_3N$ yielded W metal[25], while the products from the reaction of $WCl_6$ with $NaN_3$ were a mix of W metal (major phase) and $W_2N$[26]. Pure cubic $W_2N$ was prepared from $WCl_4$ and $LiNH_2$ at 700 ºC[24].

PXD patterns of the samples prepared at 450 and 550 °C are shown in Fig. 5.5. Four broad peaks were observed at around $2\theta$ = 38, 44, 64 and 76° corresponding to the rocksalt structure. A small peak at $2\theta$ = 40.3° was attributed to W metal. Crystalline tungsten nitride was obtained at 550 ºC while at 450 ºC an amorphous material was formed via broad features in the PXD baseline. Crystallite sizes ranged from 2.4 to 1.5 nm at temperatures in the range 550-450 ºC. Smaller crystallites sizes than found in

CrN (6-25nm) or MoN (11nm) ware obtained. The most nitrogen-rich phase $WN_{0.99}C_{0.47}$ synthesised at 450 ºC was close in composition to WN (7 % N calculated).

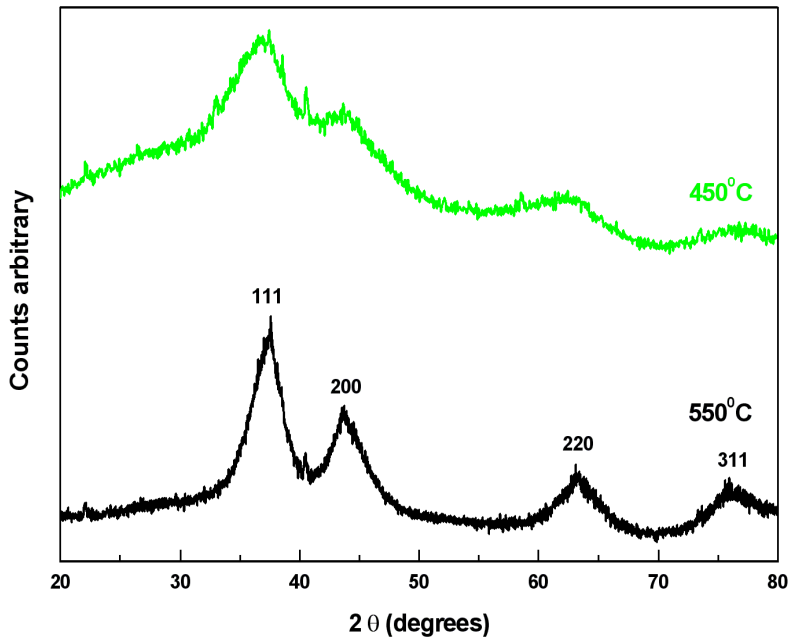


**Figure 5.8** XRD patterns of the products of reaction of $WCl_4$ with $LiNH_2$.

The fully crystallised sample obtained from $WCl_4$ and $LiNH_2$ at 550 ºC had a similar composition, $WN_{0.73}C_{0.15}$, assuming that all the carbon was in the lattice, not present as a secondary phase. Only one rocksalt-structured WN is listed in ICSD[27], which used electron diffraction to obtain a lattice parameter of 4.13 Å[32]. Thermal treatment of $WCl_4$ with ammonia has, however, been used to obtain a similar material to that observed in this work, with a lattice parameter of 4.12 Å[33]. The lattice parameters obtained herein (Table 5.1), were slightly smaller than those previously reported.

TEM images (Fig 5.9) of WN produced from $WCl_4$ and $LiNH_2$ at 550 ºC shows particles fairly aggregated with size of about 40 nm.

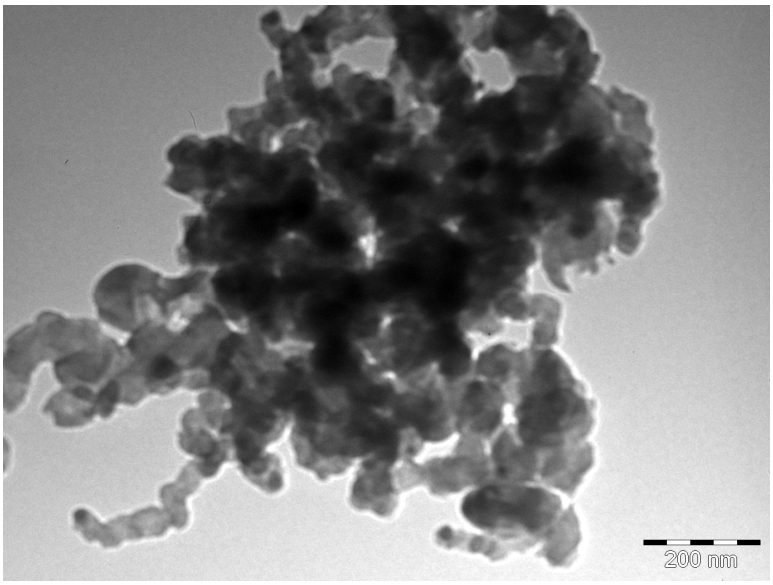


**Figure 5.9** TEM image of WN prepared from $WCl_4$ and $LiNH_2$ at 550 ºC.

TGA ( Fig. 5.10 a) of WN carried out under nitrogen shows a mass loss (~10 %) up to 700 ºC due to the presence of amide groups while at higher temperature the mass loss is attributed to the elimination of $NH_3$ and $N_2$.

The TGA profile (Fig. 5.10 b) in oxygen of WN produced in $NH_3$ shows a mass gain (~ 9 %) between 120 and 470 ºC corresponding mainly to oxidation of WN to $WO_2$. The composition of the sample was $WN_{0.73}C_{0.15}$ with carbon content of ~2.8 %. The amount of tungsten (~93 %) calculated from the TGA was consistent with this composition.

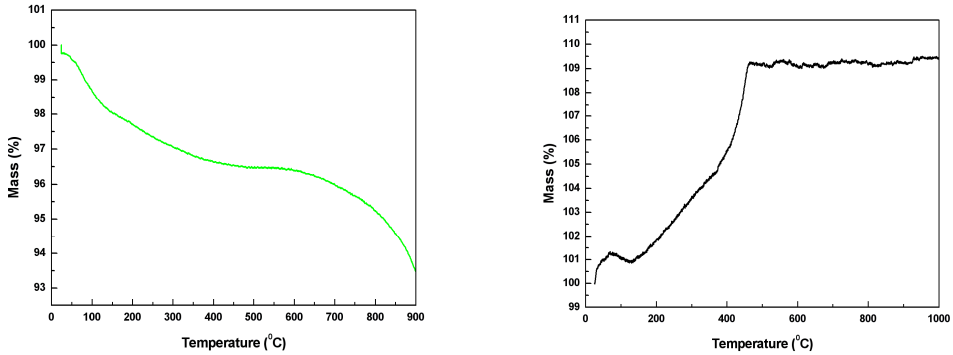


**a)** **b)**

**Figure 5.10** TGA of WN produced from $WCl_4$ and $LiNH_2$ at 550 ºC. a) under nitrogen and b) oxygen.

# 5.3 Reactions of $CrCl_3$, $MoCl_5$ and $WCl_4$ with $NH_3$

The following section describes an extension of the use of ammonia as nitrogen source in the preparation of group 6 nitrides. Previous studies reported the synthesis of transition metal nitride from the reactions of solid metal chlorides in ammonia gas at relatively low temperature, but the nitradation mechanism have been rarely investigated. In this study the reactions of transition metal chloride with ammonia were carried out under solvothermal conditions in a similar way to those discussed in chapter 5. Comparison between the products obtained with $LiNH_2$ and $NH_3$ will be made.

## 5.3.1 Reactions between $CrCl_3$ and $NH_3$

The reactions of $CrCl_3$ with $NH_3$ were performed in benzene at temperatures in the range 400-550 ºC. The formation of chromium nitride proceeds as that described in chapter 4 for the preparation of vanadium nitride with a 10-fold molar excess of ammonia. The PXD patterns of the products (Fig. 5.11) matched cubic CrN. Sharper reflections than those observed in the reactions of $CrCl_3$ with $LiNH_2$ revealed large crystallites with size ranging from 46 to 51 nm (Table 5.2) at temperatures in the range 550-500 ºC. No $Cr_2N$ was observed in CrN samples made using $NH_3$ (Fig. 5.11).

**Table 5.2** Products of reactions of group 6 halides with $NH_3$ heated for 24 h in benzene

| Halide | T/ºC | Product/s (lattice parameters in Å) | Size (nm) | % C, N | Composition |
|---|---|---|---|---|---|
| $CrCl_3$ | 450 | Unidentified phase | | | |
| | 500 | CrN (a = 4.1516(4)) | 46 | 3.2, 22.5 | $CrN_{1.12}C_{0.18}$ |
| | 550 | CrN (a = 4.1534(2)) | 51 | 1.5, 17.1 | $CrN_{0.78}C_{0.08}$ |
| $MoCl_5$ | 550 | MoN (a = 4.095(8)) | 2 | 0.1, 6.2 | $MoN_{0.45}$ |
| $WCl_4$ | 450 | Amorphous | | | |
| | 500 | WN (a = 4.061(5)) | 2 | 2.3, 6.3 | $WN_{0.86}C_{0.38}$ |
| | 550 | WN (a = 4.087(3)) | 2 | 8.1, 7.6 | $WN_{1.18}C_{1.47}$ |

% H always < 0.1%.

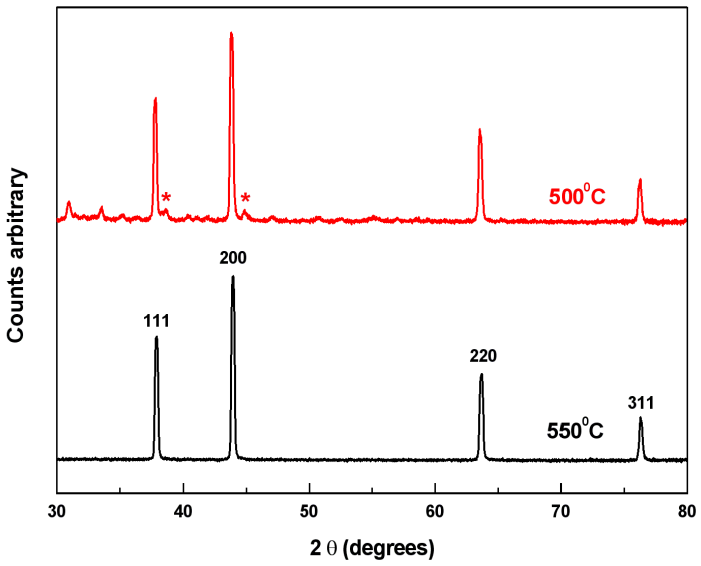


**Figure 5.11** XRD patterns of the products of reaction of $CrCl_3$ with $NH_3$ heated for 24 h.

Lattice parameters listed in Table 5.2 were higher than expected (4.14 Å), suggesting that the small quantity of carbon observed in these samples must be incorporated into the CrN lattice.

Stoichiometric CrN contains 21.2% N and the analyses indicated compositions of $CrN_{1.12}C_{0.18}$ at 500 ºC and $CrN_{0.78}C_{0.08}$ at 550 ºC. At 400 and 450 ºC an unidentified phase with reflections at $2\theta$ = 31.9 and 34.6 º was found. There was no evidence of CrN and the samples were always sticky. It was thought likely that these reactions did not proceed to completion.

TEM images (Fig 5.12) of CrN produced from $CrCl_3$ and $NH_3$ at 550 ºC shows a mixture of spherical and elongated particles which were fairly aggregated and had individual crystallites of close in size to those obtained from the PXD linewidths.

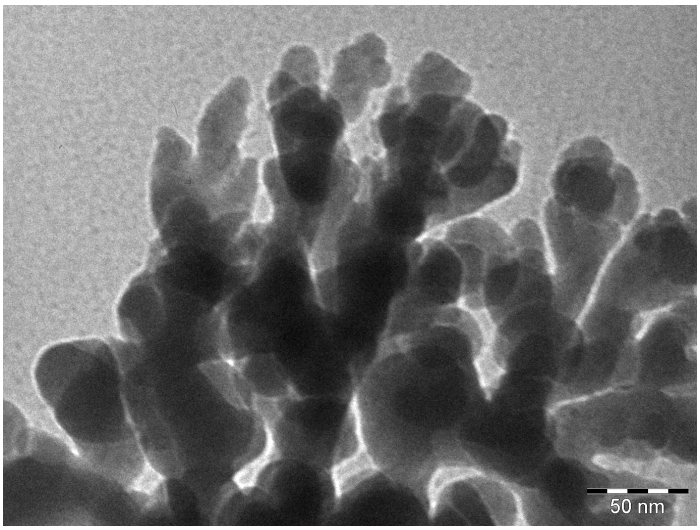


**Figure 5.12** TEM of VN synthesised from $CrCl_3$ and $NH_3$ at 550 ºC

## 5.3.2 Reactions of $MoCl_5$ with $NH_3$

The formation of molybdenum nitrides from $MoCl_5$ and $NH_3$ can be considered to proceed as follows:

$$MoCl_5 + {}^{20}/_{3}\ NH_3 \longrightarrow MoN_{1-x} + 5\ NH_4Cl + ({}^{1}/_{3} + {}^{1}/_{2}\ x)\ N_2$$

The reaction produced molybdenum nitride, ammonium chloride and nitrogen. $NH_4Cl$ is a solid which sublimes at 340 ºC without melting. Since the reactions were carried out in a closed system it was always found mixed with the nitride phase. Its elimination was then carried out by dissolution of the powder in methanol.

The PXD pattern of molybdenum nitride is shown in Fig. 5.13. Four broad peaks assigned by Miller indices revealed pure crystalline $\gamma$-$Mo_2N$. It was only obtained at 550 ºC. Samples prepared at 550 ºC and below were amorphous. The particle size of the powder was estimated to be 2 nm which was significantly lower than that found with $LiNH_2$ (11 nm). As with Cr, the carbon content was low. The overall composition can be calculated as $MoN_{0.45}C_{0.01}$, close to $Mo_2N$. The nitrogen content in the sample prepared at 550 ºC was 6.2 %, significantly lower than that revealed with $LiNH_2$ (9.2%).

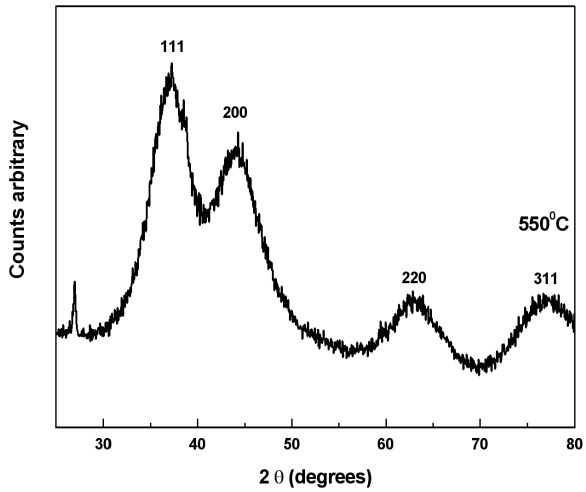


**Figure 5.13** XRD pattern of $Mo_2N$ produced from $MoCl_5$ with $NH_3$ at 550 ºC.

TEM images in Fig. 5.14 show a mixture of small spherical crystallites (less than 5 nm) and tubes of various lengths (100-600nm) and diameter (30-60 nm). Aggregation of these small crystallites was revealed in various area of the samples.

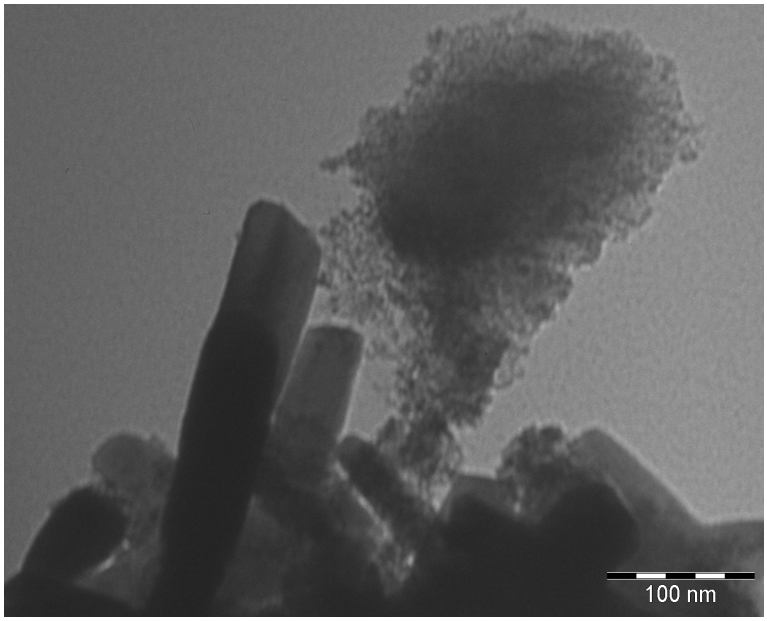


**Figure 5.14** TEM of $Mo_2N$ produced from $MoCl_5$ and $NH_3$ at 550 ºC

Previously molybdenum nitrides nanotubes were obtained by atomic layer deposition method[34]. This approach involved the deposition of molybdenum film on anodized aluminum oxide (AAO) template which was the etched away with sodium hydroxide solution. AAO is one of the most used templates for nanotube preparation. AAO with pore diameter of about 50 nm and pore length of 80 μm was used to make

molybdenum nitrides nanotubes. It has also been used in other applications like enantiomeric filtering[35], catalysis[36] etc. Depending on the condition used, different forms of molybdenum nitride nanotube were prepared. Isolated tubes (6 μm) were achieved when the template was dissolved in ultrasonic bath whereas bundle was prepared when the sample was soaked in sodium hydroxide solution without agitation.

TGA plot of $Mo_2N$ carried out under nitrogen is shown in Fig. 5.15. The initial decomposition starts at ~ 34 ºC and ends at ~ 600 ºC with a mass loss (~ 4 %) presumably due to the presence of amide groups. A second decomposition observed at higher temperature involves the elimination of $N_2$. The sample prepared at 550 ºC had a composition of $MoN_{0.45}$ with low carbon content of about 0.1 %. This suggested the possibility that benzene decomposition is somehow catalyzed by metal. Different carbon content was found in nitrides prepared with different metal type. Higher carbon content (1.5 %) was revealed in the nitride prepared from $CrCl_3$ with ammonia at 550 ºC.

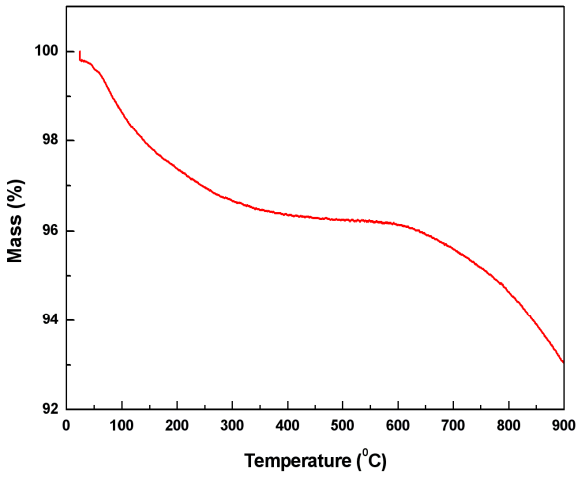


**Figure 5.15** TGA under nitrogen of $Mo_2N$ produced from $MoCl_5$ and $NH_3$ at 550 ºC.

### 5.5.3 Reactions of $WCl_4$ with $NH_3$

Tungsten nitride was previously synthesized from $WCl_6$ and $NH_3$ at temperature in the range 600-675 ºC using chloroform as solvent[33]. Cubic type WN was prepared at 675 º C whereas at higher temperature (~800 ºC) the product contained W metal. The lattice parameter of cubic WN formed at 675 ºC was a = 4.121 Å which is lower than the value reported in literature (a = 4.13 Å). WN contained excess of nitrogen (~9 %) compared with the calculated value (~ 7 %) and TEM images consisted of agglomerated clusters of nanocrystallites.

The reactions of $WCl_4$ with $NH_3$ were performed in benzene at temperatures in the range 450-550 °C. The formation of WN proceeds as follows:

$$WCl_4 + 6\ NH_3 \longrightarrow WN + 4\ NH_4Cl + {}^{2}/_{3}\ NH_3 + {}^{1}/_{3}\ N_2$$

The production of tungsten nitride involves the reduction of tungsten from its +4 oxidation state to +3. Comparing these nitrides with MoN prepared from $MoCl_5$ (Mo has oxidation state + 5) and $NH_3$ was observed (Fig. 5.16) that tungsten nitride crystallized at temperature of 500 °C whereas $Mo_2N$ was amorphous. At 450 ºC the reaction between $WCl_4$ and $NH_3$ yielded an amorphous material with broad humps in the PXD pattern (Fig. 5.16) resembling the peaks for WN. At 500 and 550 ºC, nanocrystalline WN with same particle size (~ 2nm) was obtained with overall composition $WN_{0.86}C_{0.38}$ and $WN_{1.18}C_{1.47}$ respectively. A carbon content of about 8 % was revealed by microanalysis in the sample prepared at 550 °C. Considering that the initial precursors do not contain carbon it can be only due to the decomposition of benzene. It is probable that at least some of the carbon in these materials is present in an elemental form. The lattice parameters (Table 5.2) were similar to those obtained with $LiNH_2$.

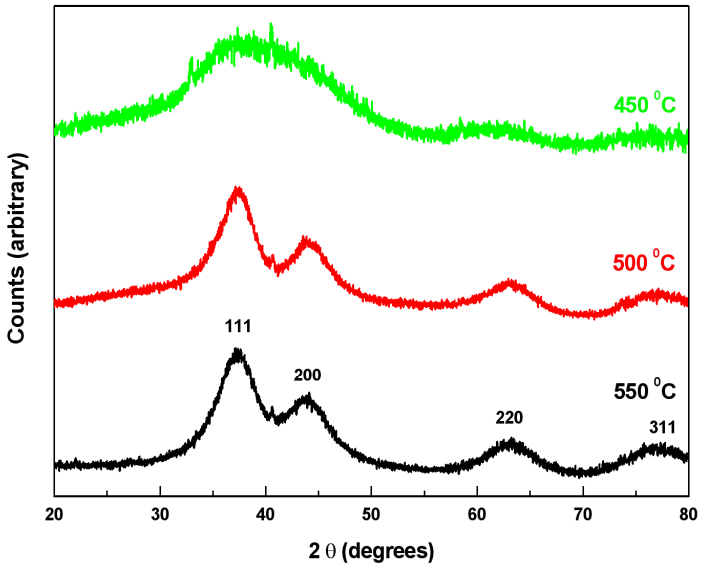


**Figure 5.16** XRD patterns of WN produced from $WCl_4$ with $NH_3$ at different temperatures. Reflection positions for WN are marked over the pattern of WN prepared at 550 °C. The peak at $2\theta = 40°$ revealed small traces of W metal in the final materials.

TEM images (Fig. 5.17) show significant aggregation of crystallites in the sample prepared due to the small crystallites formed.

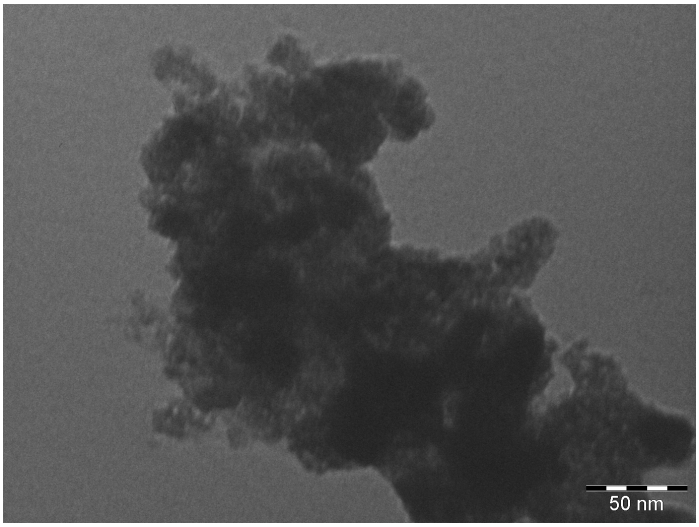


**Figure 5.17** TEM images of WN prepared from $WCl_4$ and $NH_3$ at 500 ºC

# 5.4 Experimental

Preparations were carried out under anaerobic conditions using either glove box or Schlenk line techniques for sample loading and handling. Benzene was distilled from Na and $CH_3OH$ from $NaOCH_3$. $CrCl_3$ (99.99%), $WCl_4$ (95%), were purchased from Aldrich Chemical Co. and $MoCl_5$ (99.6%) from Alfa Aesar, all were used as supplied. Ammonia (Air Products) was distilled from a sodium/ammonia solution before use. $LiNH_2$ was synthesised by reacting 1.6 M $^n$BuLi in hexane (Aldrich) with excess distilled ammonia at -78 ºC, filtering, and drying the product under vacuum.

All synthesis was performed in a 75 $cm^3$ autoclave (Parr 4740CH). Typically, 0.6 g of metal chloride was placed in the silica liner and covered with 15 $cm^3$ of benzene. Either a stoichiometric amount of $LiNH_2$, calculated to balance the lithium and chloride components of the reaction mixture, or a 10-fold molar excess of ammonia, was added. The autoclave was heated at various temperatures, typically for 24 h. After cooling to room temperature, the autoclave was opened and the mixture was transferred to a Schlenk tube inside the glove box. The solid was collected by filtration, washed with dry methanol three times to remove the LiCl or $NH_4Cl$ by-product, and dried under vacuum.

Powder X-ray diffraction (PXD) measurements were performed on a Siemens D5000 diffractometer using Cu $K_{\alpha_1}$ ($\lambda$ = 1.5406 Å) radiation. The phases present were identified by comparison with the JCPDS database[37] and patterns refined using the GSAS package[38, 39]. Crystallite sizes were extracted from the Lorentzian component of the profile coefficients as described in the GSAS manual[38, 39]. Transmission electron microscopy (TEM) was carried out with a Hitachi 7000 (75 kV) or Jeol JEM-3100 (300 kV). Samples were prepared by ultrasound dispersal in toluene, followed by deposition on carbon-coated Cu grids. C, H, N combustion analyses were carried out by Medac Ltd. (Egham, Surrey, UK). Samples were also analysed for chlorine content (none found) by energy dispersive X-ray analysis (Jeol JSM-5910 with Oxford Inca probe). Thermogravimetric analyses (TGA) were performed in a mettle Toledo TGA/SDTA851e instrument under flowing BIP nitrogen or 60 % $O_2$-40 % $N_2$ from 25° to 1000 °C at a rate of 10 °/min.

# 5.5 Conclusions

Reactions of $CrCl_3$, $MoCl_5$ and $WCl_4$ with $LiNH_2$ or $NH_3$ in benzene, under solvothermal conditions produced nanocrystalline metal nitrides (CrN, $Mo_2N$, and WN).
CrN has previously obtained solvothermally[7] whilst molybdenum and tungsten nitrides/carbonitrides were synthesised solvothermally for the first time herein.

In the reactions of $CrCl_3$ with $LiNH_2$ cubic CrN with traces of hexagonal $Cr_2N$ was observed. Pure cubic CrN was obtained at shorter reaction time (5h). The particle size calculated by Rietveld refinements ranged from 6 to 25 nm at temperatures in the range 550-300 °C. The composition of the sample prepared from $CrCl_3$ and $LiNH_2$ at 550 ºC was nitrogen deficient whereas excess of nitrogen (22.5 %) was found in the sample made at 500 ºC. Higher lattice parameters calculated here, than that reported in literature[27], suggested incorporation of some carbon. When $CrCl_3$ was reacted with ammonia pure cubic CrN was prepared with particle sizes ranged from 46 to 51nm. Reaction temperatures lower than 500 °C did not lead to the formation of chromium nitride. Samples were nitrogen deficient with similar lattice parameter calculated from the same reaction performed in $LiNH_2$.

Reactions of $MoCl_5$ with $LiNH_2$ or $NH_3$ led to samples with composition between MoN and $Mo_2N$. Small crystallites (~2 nm) were prepared when ammonia was used as nitrogen source. Low carbon and nitrogen contents were found when molybdenum nitride was prepared in $NH_3$ at 550 ºC. The reactions of $MoCl_5$ with $LiNH_2$ or $NH_3$ yielded an amorphous material at temperature lower than 550 ºC. Different carbon content was found in nitride prepared with different metal type. This may suggest that benzene decomposition is catalyzed by metal.

Similar crystallites size (~2 nm) was also observed in the reactions of $WCl_4$ with $LiNH_2$ or $NH_3$. In these systems traces of W metal were also revealed in the PXD patterns due to the thermal instability of these nitrides. Most samples were nitrogen deficient, the exceptions were $WN_{0.99}C_{0.47}$ and $WN_{1.18}C_{1.47}$ formed in $LiNH_2$ and $NH_3$ at 450 and 550 ºC. The preparation of WN at 550 ºC revealed a higher carbon (8.1 %) and nitrogen (7.6 %) content when ammonia was used. Generally the samples produced can be considered as carbonitrides.

TEM images of the samples typically showed isotropic particles, which were fairly aggregated and had individual crystallites of similar size to those, obtained from the PXD linewidths. The only exception was MoN where a mixture of isotropic particles and 30-50 nm rods was obtained. The reaction of metal chlorides with $LiNH_2$ produce a

meltable LiCl by-product during the synthesis process that did not have significant solubility in the benzene or benzene/ammonia solvent, and it was likely that the nanorods grow in this partially melted phase at the bottom of the reactor.

A mix of small crystallites and tubes of various lengths (100-600 nm) and diameter (30-60 nm) was formed when $MoCl_5$ was reacted with ammonia. Previously preparation of molybdenum nitride nanotube has been achieved by deposition methods. Solvothermal reaction of $MoCl_5$ with $NH_3$ performed in this study offers an alternative route to perform nanostructured nitrides which could have application in catalysis.

# 5.6 References


1. L. E. Toth, *Transition Metal Carbides and Nitrides, Academic Press, New York*, 1971.
2. R. Riedel, *Handbook of Ceramic Hard Material, Ed., Wiley*, 2000.
3. L. Swadzba, A. Maciejny, B. formanek, P. Liberski, P. Podolski, B. Mendala, H. Gabriel and A. Poznanska, *Surf. Coat. Technol.*, 1996, **78**, 137.
4. P. Panjan, B. Navinsek, A. Cvelbar, A. Zalar and I. Milosev, *Thin Solid Films*, 1996, **282**, 298.
5. U. Kopacz and R. Riedl, *Z. Metallkd.*, 1992, **83**, 492.
6. Y. Claesson, M. Georgson, A. Roos and C.-G. ribbing, *Solar Energy Mater.*, 1990, **20**, 455.
7. X. F. Qian, X. M. Zhang, C. Wang, K. B. Tang, Y. Xie and Y. T. Qian, *Mater. Res. Bull.*, 1999, **34**, 433.
8. G. Hägg, *Z. Phys. Chem.*, 1930, **B7**, 339.
9. A. Bezinge, K. Yvon, J. Muller, W. Lengauer and P. Ettmayer, *Solid State Comm.*, 1987, **63**, 141.
10. G. S. Ranhotra, G. W. Haddix, A. T. Bell and J. A. Reimer, *J. Catal.*, 1987, **108**, 24.
11. G. S. Ranhotra, A. T. Bell and J. A. Reimer, *J. Catal.*, 1987, **108**, 40.
12. M. Saito and R. B. Anderson, *J. Catal.*, 1980, **63**, 438.
13. M. Saito and R. B. Anderson, *J. Catal.*, 1981, **67**, 296.
14. E. J. Markel and J. W. Van-Zee, *J. Catal.*, 1990, **126**, 643.
15. L. Volpe and M. Boudart, *J. Phys. Chem.*, 1986, **90**, 4874.
16. H. Jehn and P. Ettmayer, *J. Less-Common Metals*, 1978, **58**, 75.
17. L. Volpe and M. Boudart, *J. Solid State Comm.*, 1985, **59**, 332.
18. M. D. Lyutaya, *Sov. Powder Metall. Met. Ceram.*, 1979, **3**, 190.
19. B. Cendlewska, A. Morawski and A. Misiuk, *J. Phys. F. Met. Phys.*, 1987, **17**, L71.
20. W. Lengauer, *J. Cryst. Growth*, 1988, **87**, 295.

21. R. Marchand, F. Tessier and F. J. DiSalvo, *J. Mater. Chem.*, 1999, **9**, 297.
22. N. Schonberg, *Acta Chem. Scand.*, 1954, **8**, 204.
23. M. Y. Kwak, D. H. Shin, T. W. Kang and K. N. Kim, *Phys. Stat. Sol.*, 1999, **174**, R5.
24. I. P. Parkin and A. T. Rowley, *J. Mater. Chem.*, 1995, **5**, 909.
25. J. C. Fitzmaurice, A. L. Hector and I. P. Parkin, *J. Chem. Soc. Dalton Trans.*, 1993, 2435.
26. A. L. Hector and I. P. Parkin, *Polyhedron*, 1995, **14**, 913.
27. *Inorganic Crystal Structure Database accessed via "The United Kingdom Chemical Database Service" D. A. Fletcher, R. F. McMeeking and D. Parkin, J. Chem. Inf. Comput. Sci.*, 1996, **36**, 746.
28. M. B. Kanoun, S. Goumri-Said and M. Jaouen, *Phys. Rev. B: Condens. Matter Mater. Phys.*, 2007, **76**, 134109.
29. T. Kawashima, E. Takayama-Muromachi and P. F. McMillan, *Physica C.*, 2007, **460**, 651.
30. C. L. Bull, T. Kawashima, P. F. McMillan, D. Machon, O. Shebanova, D. Daisenberger, E. Soignard, E. Takayama-Muromachi and L. C. Chapon, *J. Solid State Chem.*, 2006, **179**, 1762.
31. A. L. Hector and I. P. Parkin, *Chem. Mater.*, 1995, **7**, 1728.
32. V. I. Khitrova, *Sov. Phys. Crystall.*, 1959, **4**, 513.
33. D. Choi and P. N. Kumta, *J. Am. Ceram. Soc.*, 2007, **90**, 3113.
34. V. Miikkulaien, M. Suvanto and T. A. Pakkanen, *Thin Solid Films*, 2008, **516**, 6041.
35. S. Liu and K. Huang, *Sol. Energy Mater. Sol. Cells*, 2005, **85**, 125.
36. M. Kemell, V. Pore, J. Tupala, M. Ritala and M. Leskela, *Chem. Mater.*, 2007, **19**, 1816.
37. *PCPDFWIN, version 2.4; Powder Diffraction File, International Center for Diffraction Data: Swarthmore, PA*, 2003.
38. A. C. Larson and R. B. Von-Dreele, *General Structure Analysis System (GSAS), Los Alamos National Laboratory Report LAUR*, 2004, **86-748.**
39. B. H. Toby, *J. Appl. Crystallogr.*, 2001, **34**, 210.

# 6.1 Introduction

The following chapter describes the preparation of gallium nitride through thermal decomposition of $[Ga(NEt_2)_3]_2$ and $[Ga(NMe_2)_3]_2$. The amido-gallium precursors were prepared by reacting $GaCl_3$ with $LiNM_2$ (M = Et, Me), in diethylether and hexane respectively. The pyrolysis reactions were investigated employing stabilizing agents such as hexadecylamine- trioctylamine (HDA-TOA), TOA or trioctylphosphine (TOP) to prevent uncontrolled growth and aggregation of nanoparticles. This method known as the "hot injection technique" has been used extensively in the preparation of II-VI semiconductor nanoparticles (e.g. CdSe, CdS, CdTe and ZnSe)[1]. Less information is available about III-V semiconductors (e.g. GaN) due to their higher lattice energies, meaning high temperature is usually required to achieve satisfactory crystallinity.

## 6.2 Colloidal preparations of III-V semiconductors

The synthesis and characterization of InP[2-8], GaP[3], InAs[9, 10] and GaAs[11-16] nanocrystals have been reported. Colloidal dispersions of crystalline InP were synthesized from the reaction of a chloroindium oxalate complex with $P(SiMe_3)_3$ in $CH_3CN$[8]. The precursor was then added to a solution of trioctylphosphine oxide (TOPO)- trioctylphospine (TOP) and heated at 270 ºC for 3-6 days. Prolonged heating (6 days) was necessary to convert the precursor to InP. Crystalline zinc-blende InP with a particle size of about 25 Å was produced. The same starting material $P(SiMe_3)_3$ was used to prepare GaP[8]. Two different compounds ($GaCl_3$ or a chlorogallium oxalate complex) were mixed with $P(SiMe_3)_3$ in toluene to room temperature. The resulting precursors were heated in the coordinating solvent TOPO-TOP. Zinc-blende GaP was obtained at temperature in the range 270-400 ºC. The particle size was estimated at about 30 Å, while at lower reaction temperatures broad, poorly defined peak were observed and the diffraction patterns did not permit an estimate of the particle size. The synthesis of colloidal InAs was achieved by the reaction of $InCl_3$ with $As(SiMe_3)_3$. InAs was obtained at temperatures ranging from 240 to 265 ºC. TOP was used both as solvent and capping agent. The size of the nanocrystals isolated was in the range from 25 to 60 Å in diameter. The powder X-ray diffraction patterns showed reflections characteristic of the cubic zinc blende structure. The luminescence properties of InP and InAs nanocrystals were improved through the growth of an epitaxial shell of a higher band gap II-VI or III-V on the core InAs nanocrystal[17, 18].

Gallium nitride is an important III-V semiconductor that has recently attracted much attention due to its physical properties, such as a wide and direct band gap[19], low

compressibility and high thermal conductivity which make it useful in applications as blue-light emitting and laser diodes, transistors[20, 21], UV photodetectors and high temperature electronic devices[22-24].

Nanocrystalline GaN was prepared by Wells and co-workers[25, 26] through pyrolysis of polymeric gallium imide $\{Ga(NH)_{3/2}\}_n$. In order to prepare this gallium imide, $[Ga(NMe_2)_3]_2$ was reacted with gaseous or liquid $NH_3$. The pyrolysis of $\{Ga(NH)_{3/2}\}_n$ was carried out at temperatures in the range 450-500 °C under vacuum or $NH_3$ flow. A mixture of cubic and hexagonal GaN was always obtained. The same mixture of phases for GaN was previously reported by Gladfelter et al[27] from thermal decomposition of $[H_2GaNH_2]_3$. Pyrolisis of cyclotrigallazane, $[H_2GaNH_2]_3$, was performed under argon for 4 h at 600 °C. In $N_2$ or $NH_3$ atmosphere the results were similar. Microanalysis after pyrolisis at 600 °C revealed low hydrogen and carbon content (less than 1 %) and nitrogen was ~ 14 %. This value was low compared to the calculated percentage of nitrogen in GaN (16.7 %). The particle was 60 Å in diameter. Gonsalves and co-workers[28, 29] prepared cubic GaN from thermal decomposition of $Ga_2(NMe_2)_6$ under $NH_3$ at 600 °C for 4 h. Microanalysis revealed nitrogen deficient material with formula $GaN_{0.86}$. Carbon and hydrogen content were found less than 1 %. TEM images indicated particles of large size ranging from 50-100 nm in diameter. A better analysis of the particles at higher magnification revealed that larger particles were composed of agglomerates of smaller particles (~5 nm). These methods offered minimal control over particle size and did not allow the nanocrystals to be dispersed in solvents to form transparent solutions suitable for optical measurements or for the processing.

A lot of interest is focused on advanced chemical synthesis routes for producing a size-controlled nanocrystalline GaN semiconductor. The preparation of GaN nanocrystals have been proven to be difficult and only a few studies have been reported. One of these methods was investigated by Micic et al[30] by the reaction of $[Ga(NMe_2)_3]_2$ with gaseous ammonia. The polymer achieved, $\{Ga(NH)_{3/2}\}_n$, was pyrolyzed in HDA/TOA yielding zinc blende GaN with particles of spherical shape and diameter of about 30 Å. Evidence of quantum confinement was observed, in that the band gap of GaN nanocrystals was shifted to higher energy (Eg = 3.65eV) compared with bulk GaN (Eg = 3.2-3.3 eV for zinc blende structure). The same amido gallium precursor was used by G. Pan[31] et al to produce colloidal GaN nanocrystals. Pyrolytic preparation of GaN from $[Ga(NEt_2)_3]_2$ and its ammonolysis polymer, pyrolyzed at 600 ºC for 4h, was also reported[32]. A mix of hexagonal and cubic GaN was achieved in both the products.

The main aim of this work was the study of composition, size and shape of GaN nanoparticles produced via pyrolysis of gallium amides. This was important both for

the study of their size-dependent properties and for their further use in different applications.

## 6.3 Synthesis of tris (diethylamido) gallium (III)

All procedures were performed under a protective nitrogen atmosphere using standard Schlenk techniques or in a glove box filled with nitrogen. Hexane and diethylether were freshly distilled from sodium/benzophenone and $HNEt_2$ from barium oxide prior to use. $LiNEt_2$ was prepared by the reaction of $HNEt_2$ (7.8 $cm^3$, 74.6 mmol) with a solution of n-BuLi (45.8 $cm^3$ 74,6 mmol) 1.6 M in hexane. The reaction proceeded as follows:

$$BuLi + HNEt_2 \xrightarrow{\text{ether}} LiNEt_2 + BuH$$

$HNEt_2$ was added slowly to the solution of BuLi and an ice bath was used to keep the reaction temperature at 0 °C. The white lithium diethylamide solid was isolated by filtration and dried under vacuum. In order to prepare the amido gallium precursor, $LiNEt_2$ (5.38 g, 68 mmol) in ether (70 $cm^3$) was added dropwise to a solution of $GaCl_3$ (4 g, 22.7 mmol) in ether at -78 °C with stirring over a 1 h period. The reaction mixture was allowed to warm slowly to room temperature and stirred for a further 12 h. After the removal of the solvents from the reaction mixture under a reduced pressure, 100 $cm^3$ of hexane was added to the resulting residue. The white precipitate of LiCl was filtered off, and the solvent was removed to form a brown oily solid.

$$2\ GaCl_3 + 6\ LiNEt_2 \xrightarrow[24\ h]{\text{hexane}} [Ga(NEt_2)_3]_2 + 6\ LiCl$$

The identity of the product was investigated using NMR. A few mg of product was dissolved in $C_6D_6$ and the NMR spectrum was analyzed. The literature[30] $^1$H-NMR spectrum (270 MHz, $C_6D_6$) of $[Ga(NEt_2)_3]_2$, showed the presence of two sets of triplets ($CH_3$) at $\delta$ 1.08 and 1.21 ppm and overlapped quartets ($CH_2$) at $\delta$ 3.09 and 3.16 ppm. The integrated intensity ratio of the signal at $\delta$ 1.21 to the signal at $\delta$ 1.08 ppm and that of the signal at $\delta$ 3.16 to the signal at $\delta$ 3.09 ppm were almost 2. The $^{13}$C-NMR spectrum (67.8 MHz, $C_6D_6$) showed two $CH_3$ signals at $\delta$ 12 and 17 ppm and two $CH_2$ signals at $\delta$ 42 and 45 ppm, which were also consistent with the structure possessing two environments of ethyl groups. A representation of the structure of $[Ga(NEt_2)_3]_2$ is shown in Fig. 6.1.

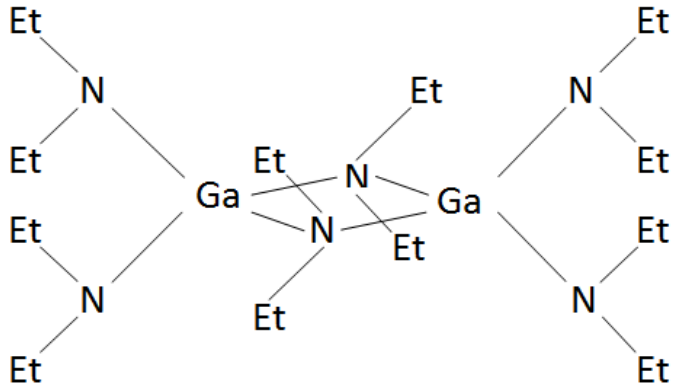


**Figure 6.1.** Representation of the structure of $[Ga(NEt_2)_3]_2$.

$[Ga(NEt_2)_3]_2$ is a dimer that contains 40 H terminal and 20 in the bridging $–NEt_2$.
The precursor prepared was investigated by $^1$H-NMR. The resulting spectrum showed the presence of overlapping signals.
Overlapped quartets ($CH_2$) at $\delta$ = 3.13 and at $\delta$ = 3.08 and the triplets ($CH_3$) at $\delta$ = 1.07 and at $\delta$ = 1.18 confirmed the presence of $[Ga(NEt_2)_3]_2$. The presence of extra signals for which identification was not achieved showed that the precursor obtained contained impurities.

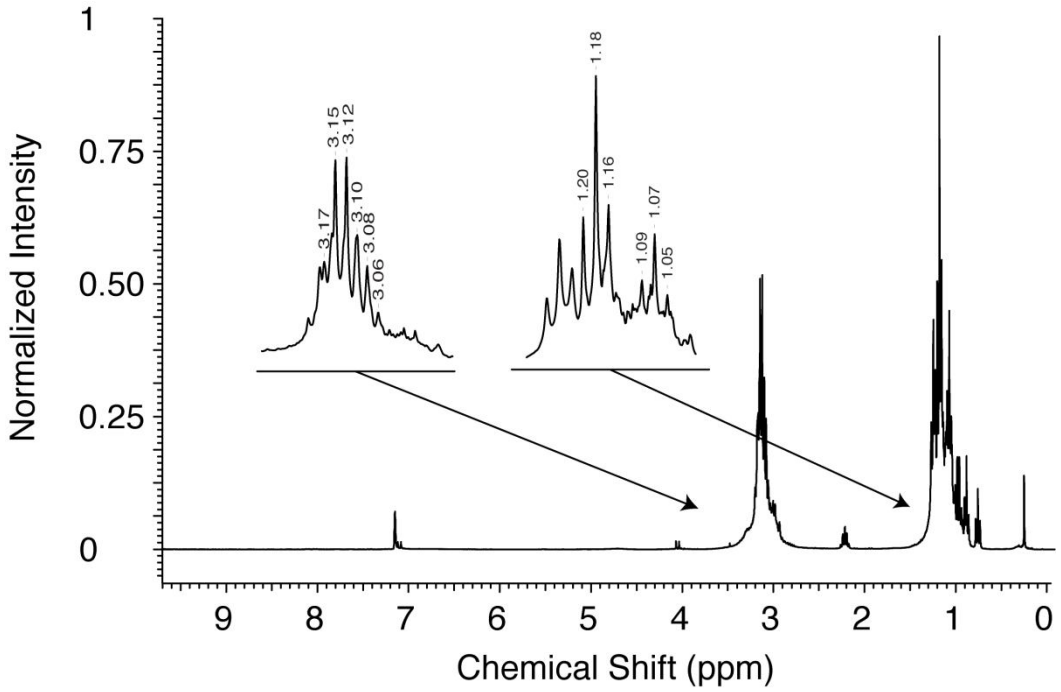


**Figure 6.2.** $^1$H-NMR spectrum of $[Ga(NEt_2)_3]_2$.

Several methods were attempted for the purification of the precursor. In the first investigation the precursor was dissolved in 5 $cm^3$ of ether and left in the freezer at 0 ºC for few days. The solution was filtered and the $^1$H-NMR was repeated. The separation by crystallization was not successful even in the presence of different solvents such as hexane. Another method was the sublimation under vacuum at 100 ºC by increasing the temperature slowly. In a previous work[32] was observed that $[Ga(NEt_2)_3]_2$ heated in the range from 130 ºC to 230 ºC decomposed with loss of $Et_2NH$. In order to avoid any decomposition of the precursor the sublimation was done under vacuum. $^1$H-NMR achieved after the purification of the oily product showed the same signals indicating that the impurities were not removed. The isolation of pure $[Ga(NEt_2)_3]_2$ was not achieved. Due to the difficulties in the purification of the final product, the pyrolysis reactions were not investigated.

$[Ga(NEt_2)_3]_2$ could be an important alternative to the preparation of GaN as it could reduce the carbon content in the final product due to the clean decomposition (β-hydrite elimination) of any residual $NEt_2$ groups. However, due to the difficulties with purification its use in GaN synthesis was abandoned.

## 6.4 Synthesis of tris (dimethylamido) gallium (III)

$[Ga(NMe_2)_3]_2$ was synthesized in an identical manner as described in the literature[33] to afford the product as colourless crystals. All procedures were performed under a protective nitrogen atmosphere using standard Schlenk techniques or a glove box filled with nitrogen. Hexane was freshly distilled from sodium/benzophenone prior to use. $LiNMe_2$ was prepared by the passage of $HNMe_2$ through a solution of n-BuLi (1.6 M in hexane):

$$BuLi + HNMe_2 \xrightarrow{\text{hexane}} LiNMe_2 + BuH$$

The production of n-butane as byproduct required a special attention during the reaction. $HNMe_2$ was added slowly to the solution of BuLi and an ice bath was used to keep the reaction temperature at 0 °C. Then lithium dimethylamide was isolated by filtration and dried under vacuum. In order to prepare the amido gallium precursor a slurry of $LiNMe_2$ (5.38 g, 68.1 mmol) in hexane (40 $cm^3$) was added dropwise to a solution of $GaCl_3$ (4 g, 22.7 mmol) in hexane at -78 °C with stirring over a 1 h period. The reaction mixture was allowed to warm slowly to room temperature and stirred for a further 24 h. The resulting cream coloured slurry was filtered and the solvent was

removed under vacuum to yield a caked, cream-colored solid.

$$2\ GaCl_3 + 6\ LiNMe_2 \xrightarrow[24\ h]{hexane} [Ga(NMe_2)_3]_2 + 6\ LiCl$$

The solid was redissolved in hexane (~ 5cm$^3$) and cooled to 0 °C. After two days no crystals were formed. Sublimation at 100 °C was used for the purification of $[Ga(NMe_2)_3]_2$ obtaining colourless crystals. The structure of $[Ga(NMe_2)_3]_2$ is shown in Fig. 6.3.

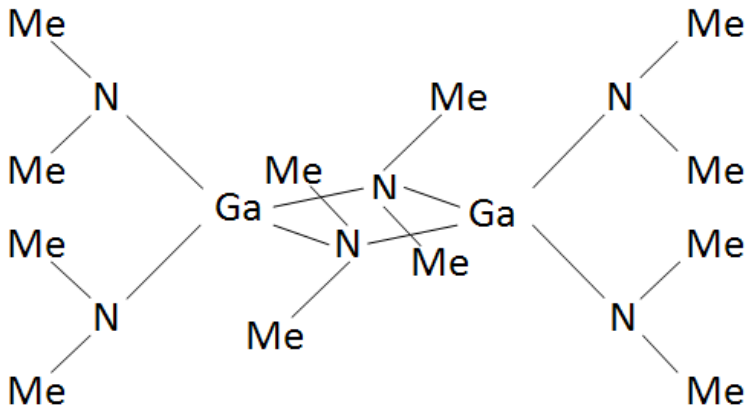


**Figure 6.3.** Representation of the structure of $[Ga(NMe_2)_3]_2$.

The identity of the product was confirmed using NMR. A few mg of product was dissolved in $C_6D_6$ and the NMR spectrum was analyzed. $^1$H-NMR spectrum (300MHz, $C_6D_6$) showed the presence of two different signals at $\delta$ = 2.46 (s, $\mu$-$NMe_2$), and 2.85 (s). $^{13}$C-NMR spectrum (300MHz, $C_6D_6$) showed two signals at $\delta$ = 43.97 and 44.35 ($\mu$-$NMe_2$). The integrated intensity ratio of the signal at $\delta$ = 2.46 to the signal at $\delta$ = 2.85 was almost 2, as expected. $[Ga(NMe_2)_3]_2$ is a dimer that contains 24 H terminal and 12 H in the bridging –$NMe_2$. The resulting spectrum is shown in Fig. 6.4. The compound identified was pure.

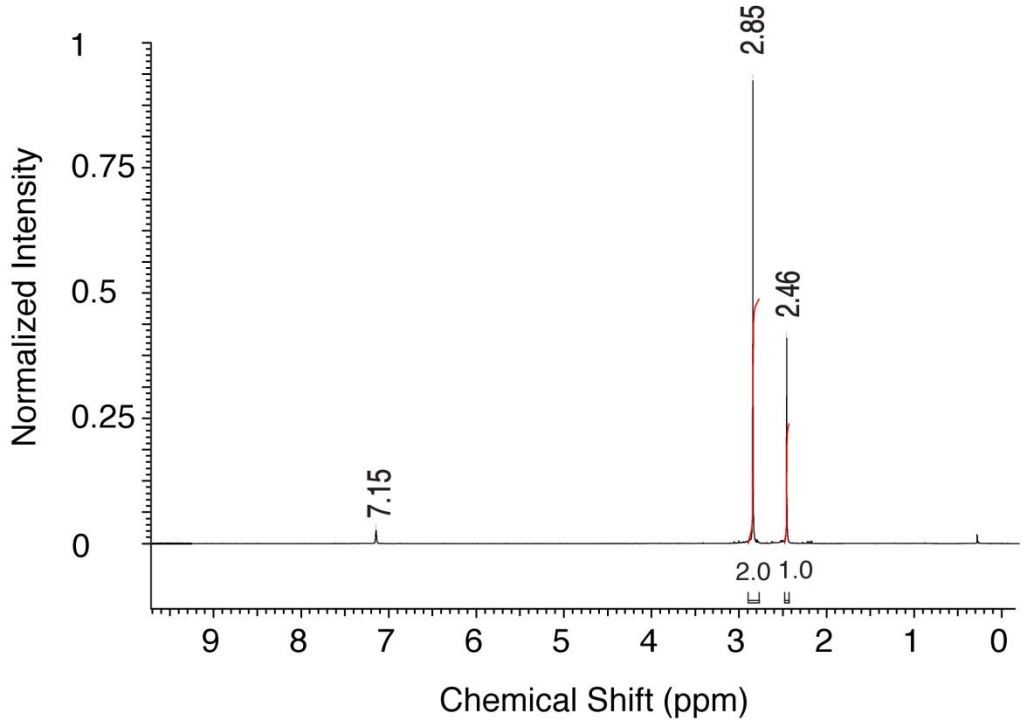


**Figure 6.4.** $^{1}$H-NMR spectrum of $[Ga(NMe_2)_3]_2$.

# 6.5 Pyrolysis of tris (dimethylamido) gallium (III)

The dimeric amidogallium precursor, $[Ga(NMe_2)_3]_2$, was used to prepare GaN nanocrystals by employing HDA (b.p. 330 °C)-TOA (b.p.365 °C) mixture, TOA or TOP (b.p.284-291°C) as solvent and stabilizing agent. The pyrolysis reactions were examined by using the hot injection technique. The setup for performing the synthesis is shown schematically in Fig. 2.2 (chapter 2). Different synthetic strategies to form GaN nanoparticles, were examined.

## 6.5.1 Pyrolysis of $[Ga(NMe_2)_3]_2$ in $N_2$

This method was reported by G. Pan[31] and co-workers. They discovered that $[Ga(NMe_2)_3]_2$ could be converted to zinc blende-type GaN without the formation of $\{Ga(NH)_{3/2}\}_n$ through the following reaction:

$$[Ga(NMe_2)_3]_2 \xrightarrow[N_2,\ \Delta]{\text{TOA, HDA}} GaN$$

This approach to GaN represented an important alternative over reactions involving poly(imidogallane). Colloidal GaN nanoparticles were prepared without the need for ammonia or for the polymeric intermediate. The polymer had poor solubility, which was a disadvantage to particle size control. Various reaction conditions (Table 6.1) such as precursor concentration, pyrolysis temperature, reaction time and concentration of the capping ligands were investigated to evaluate the preparation of GaN.

**Table 6.1** Reaction conditions used for the pyrolysis of $[Ga(NMe_2)_3]_2$ in HDA/TOA.

| $[Ga(NMe_2)_3]_2$ (mg) | Time (h) | Temperature (°C) | HDA/TOA(g/cm$^3$) |
|---|---|---|---|
| 30 | 24-78 | 300 | 1g/4 cm$^3$ |
| 50 | 24-78 | 310 | 1g/4 cm$^3$ |
| 80 | 24-78 | 290 | 1g/4 cm$^3$ |
| 100 | 24-78 | 300 | 1g/4 cm$^3$ |
| 150 | 24-78 | 315 | 1g/4 cm$^3$ |
| 200 | 1 | 326 | 1g/4 cm$^3$ |
| 200 | 10 | 330 | 1g/4 cm$^3$ |
| 200 | 24-78 | 330 | 0.5g/4 cm$^3$ |
| 200 | 24-78 | 330 | 1g/4 cm$^3$ |
| 200 | 24-78 | 330 | 2g/4 cm$^3$ |

Thermal decomposition of $[Ga(NMe_2)_3]_2$ was first investigated at temperature of ~ 300 ºC and typically kept for 3 days. Various amount of precursor were investigated in order to study any variation in size of the nanocrystals formed. When a small amount (30-150 mg) of precursor was used the solid was not isolated. The reactions performed at temperature of ~ 330 ºC in short reaction time (1-10 h) yielded to an amorphous material. Better reaction conditions were achieved at a maximum temperature of 330

°C which was maintained for 3 days. $[Ga(NMe_2)_3]_2$ (200mg), was dissolved in TOA (4 $cm^3$) in a flask on a Schlenk line under a nitrogen atmosphere. Then 1 g of HDA was heated in a three-necked flask at 330 °C.

The reaction temperature was monitored using a thermocouple in contact with the solution. When the temperature of the solution containing HDA reached the value of 330 °C the precursor was rapidly injected giving a yellow solution. The pyrolysis was carried out by refluxing this mixture under nitrogen and kept at this temperature for 3 days. After this prolonged high temperature treatment, the solution was black in colour, indicating the presence of carbon probably derived from decomposition of HDA or TOA that contained long aliphatic chains. This was an issue because the growth of the nanoparticles could not be monitored by taking the absorption spectra of aliquots from the reaction solution at different instants of time. On the other hand, high temperature and prolonged reaction time were necessary to achieve better crystallinity of the nanoparticles. In fact when the reactions were carried out by heating the solution for 1 day and using lower temperature an amorphous product was always the outcome. After pyrolysis the solution was allowed to cool down to room temperature.

### 6.5.1.1 Isolation of nanocrystallites

The solution of GaN produced was capped with HDA/TOA. In order to remove the excess of HDA/TOA the solution was diluted in toluene. A 10 $cm^3$ aliquot of the reaction solution was transferred by syringe into a vial and 5 $cm^3$ of toluene was added to the solution. The consequent addition of 10 $cm^3$ of methanol or acetonitrile to the solution led to the flocculation of nanocrystals. The flocculate was separated from the supernatant by centrifugation. Repeating this step 5-6 times it was possible to prepare nanocrystallites of smaller size. A limitation in this step was the loss of product during the collection of the solid. The samples obtained were always sticky, suggesting the presence of HDA in the final products. PXD pattern (Fig.6.5) matched zinc blende type GaN.

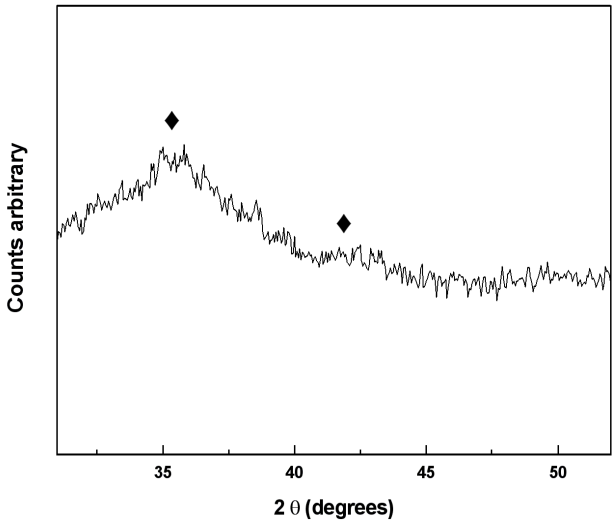


**Figure 6.5.** X-ray diffraction of GaN nanoparticles produced by pyrolysis of $[Ga(NMe_2)_3]_2$ in 200 mg of HDA and 4 $cm^3$ of TOA at 330 °C for 3 days. ♦ marks reflection positions of 111 and 200 planes for zinc blende-type GaN.

The broad peak suggested the presence of small particles in the product. This evidence was confirmed by TEM image reported in Fig. 6.6. It showed roughly spherical particles with diameter less than 5 nm. The low contrast in the image made it to difficult to image due to the presence of significant amounts of organic material (presumably HDA) which is most clearly visible on the right side of the figure.
It appears that it has not been possible to separate the particles effectively from the excess of capping agent.

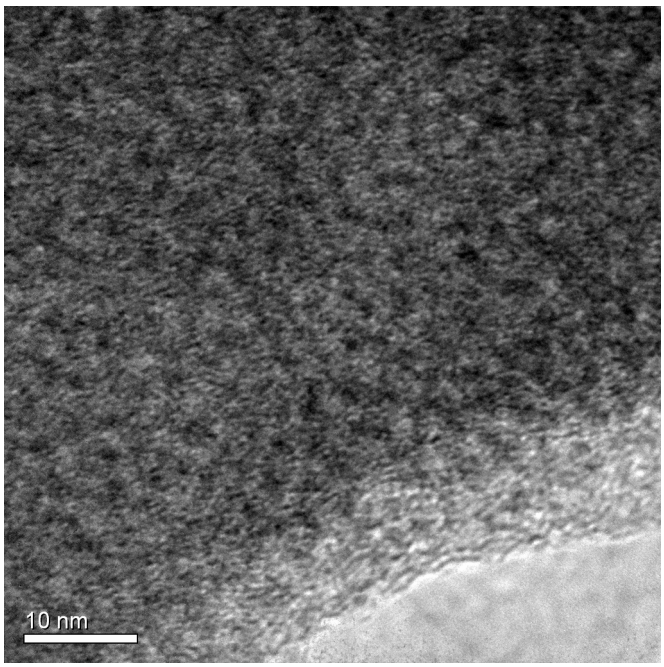


**Figure 6.6.** TEM image of GaN nanoparticles prepared at 330 °C using HDA/TOA.

In chapter 3 the reaction between $GaCl_3$ and $LiNH_2$ in the presence of HDA was reported. Addition of small amount of HDA led to a small increase in the crystallinity of the final product suggesting that it was involved in the formation of GaN whereas here the presence of HDA seemed to decrease the crystallinity of the final product. During the pyrolysis of $Ga[N(Me_2)_3]_2$ in HDA, some of the $–NMe_2$ groups present in the dimer, could be displaced with $NHC_{16}H_{34}$ groups deriving from HDA. The interaction between the precursor and HDA could have led to the formation of small particles that remained in solution and was difficult collect the solid especially considering that HDA could be covalently bound to these small particles so their solubilities could be very similar. Due to the limitation of the system used the maximum reaction temperature was 330 °C. A nucleation step at higher temperature might have allowed better crystallization, but with the equipment used it was not possible achieve this.

## 6.5.2 Pyrolysis of $[Ga(NMe_2)_3]_2$ in TOA

In order to understand the effect of HDA during pyrolysis the same reactions were investigated in the presence of TOA only as coordinating solvent. TOA cannot displace dialkylamide groups from the molecular precursor in the way the HDA can. Hence it could provide a capping group that does not interfere with the $[Ga(NMe_2)_3]_2$ decomposition process. Reaction conditions, shown in Table 6.2, were investigated to produce colloidal GaN.

**Table 6.2** Reaction conditions used for the pyrolysis of $[Ga(NMe_2)_3]_2$ in TOA.

| $[Ga(NMe_2)_3]_2$ (mg) | Time (h) | Temperature (°C) | TOA ($cm^3$) |
|---|---|---|---|
| 50 | 24-78 | 310 | 4 |
| 80 | 24-78 | 290 | 4 |
| 150 | 24-78 | 300 | 4 |
| 150 | 24-78 | 315 | 5 |
| 200 | 120 | 315 | 5 |

200 mg of $[Ga(NMe_2)_3]_2$ was dissolved in 2 $cm^3$ of TOA in a flask on a Schlenk line under a nitrogen atmosphere with stirring. The solution was rapidly injected into a hot solution of TOA (2 $cm^3$) at a temperature of 315 °C and this was maintained for 5 days. The solution was cooled down to room temperature. Even in this case the solution achieved was black indicating the presence of carbon. The solution was centrifuged and the solubility of nanoparticles was investigated using toluene/methanol or

acetonitrile as solvent system. In contrast to GaN achieved using HDA/TOA, the precipitation of nanoparticles was successful when TOA was used as solvent.

PXD data were collected using a C2 diffractometer. Powder X-ray diffraction of GaN is shown in Fig. 6.7. A mixture of cubic and hexagonal GaN was prepared in TOA. The peaks at 2θ = 35 and 40° matched zinc-blende type GaN, while the peaks at 2θ = 33, 37 and 48° resembled wurtzite type GaN.

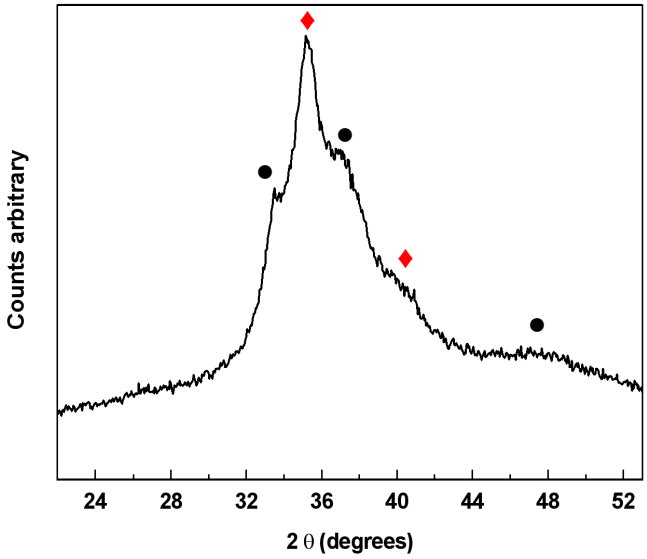


**Figure 6.7.** X-ray diffraction pattern of GaN nanoparticles from pyrolysis of $[Ga(NMe_2)_3]_2$ in TOA at 315 °C for 5 days.(● = reflection position for wurtizite-type GaN; ♦ = positions for 111 and 200 reflections of zinc-blende-type GaN).

The shape and the size distribution of the GaN nanoparticles was analyzed using a JEM-3010 electron microscope operating at 300 KV. Fig. 6.8 a) shows TEM images of several spherical particles agglomerated with diameters of about 30-50 nm. The electron diffraction pattern corresponding to hexagonal and cubic GaN is shown in Fig. 6.8 b).

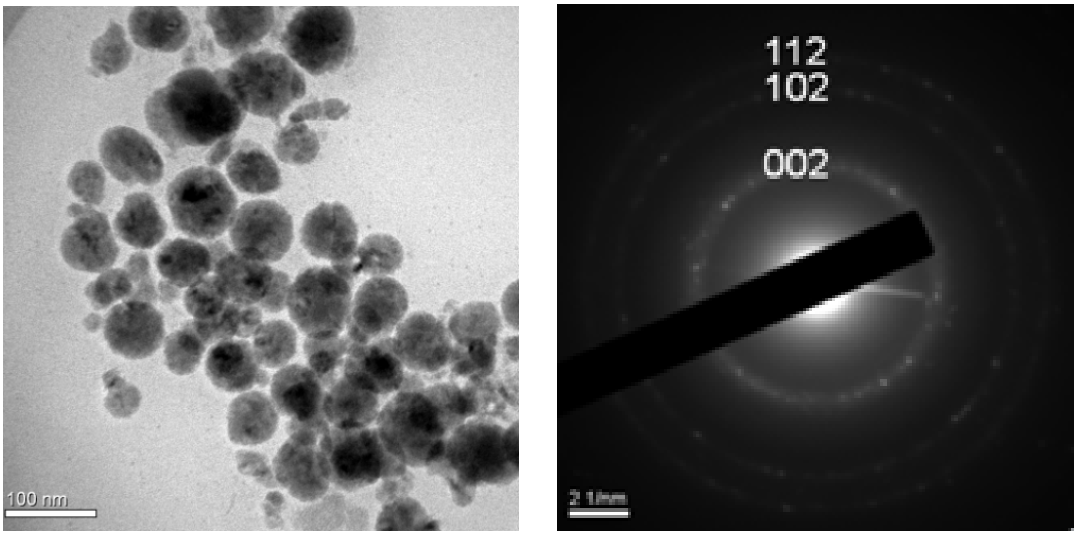


**a)** **b)**

**Figure 6.8.** a) TEM image and b) electron diffraction of GaN nanoparticles from pyrolysis of $[Ga(NMe_2)_3]_2$ at 315 °C using TOA.

Larger particle size (30-50 nm) where observed in Fig.6.8 if compared with PXD data. This can be due to the fact that a single particle can be composed of number of different aggregated crystallites of smaller size. Using the particle size of 30 nm and the main peak at 2θ of 35º in the Scherrer equation, much predicted a linewidth of 0.3º was obtained. The width of the peak at 2θ of 35º should be narrower than that observed in Fig. 6.7. Hence the particles observed in the TEM are polycrystalline and significant aggregation is occurring.

## 6.5.3 Pyrolysis of $[Ga(NMe_2)_3]_2$ in TOP

$[Ga(NMe_2)_3]_2$ was pyrolyzed using TOP (trioctylphosphine) as the coordinating solvent. TOP is a strong donor ligand which would coordinate to gallium surface sites. It was used to produce a passivating shell on the particle surface which could be used to control the growth and the agglomeration of the particles. Moreover through its alkyl groups, it provides an excellent solubility in non-polar solvents such as toluene or hexane. Reaction conditions, shown in Table 6.3, were investigated to produce gallium nitride.

**Table 6.3** Reaction conditions used for the pyrolysis of $[Ga(NMe_2)_3]_2$ in TOP.

| $[Ga(NMe_2)_3]_2$ (mg) | Time (h) | Temperature (°C) | TOP ($cm^3$) |
|---|---|---|---|
| 50 | 24-78 | 310 | 4 |
| 80 | 24-78 | 290 | 4 |
| 150 | 24-78 | 300 | 4 |
| 150 | 24-78 | 315 | 5 |
| 200 | 120 | 315 | 5 |

In a typical preparation 200 mg of $[Ga(NMe_2)_3]_2$ was dissolved in 2 $cm^3$ of TOP in a flask on a Schlenk line under a nitrogen atmosphere with stirring. This colourless solution was rapidly injected into a hot solution of TOP (2 $cm^3$) at a temperature of 315 °C which was maintained for 5 days. The solution was allowed to cool to room temperature. Even in this case the solution achieved was black presumably due to the decomposition of the long aliphatic chains contained in TOP. The solution was centrifuged and the solubility of nanoparticles was investigated using toluene/methanol or acetonitrile as solvent system. In contrast to GaN obtained using only TOA, the precipitation of nanoparticles was not successful when TOP was used as solvent. This difference may be related to strong bonding of Ga to TOP. Moreover the rate of nucleation of nanocrystals could be reduced in this system requiring higher temperature than that used in this work.

The sample was not isolated and TEM grids was made from the solution. In Fig. 6.9 is shown a TEM image of the final product achieved from pyrolysis of $[Ga(NMe_2)_3]_2$ at 315 °C. A broad distribution of spherical particles with diameter of about 50 nm was observed.

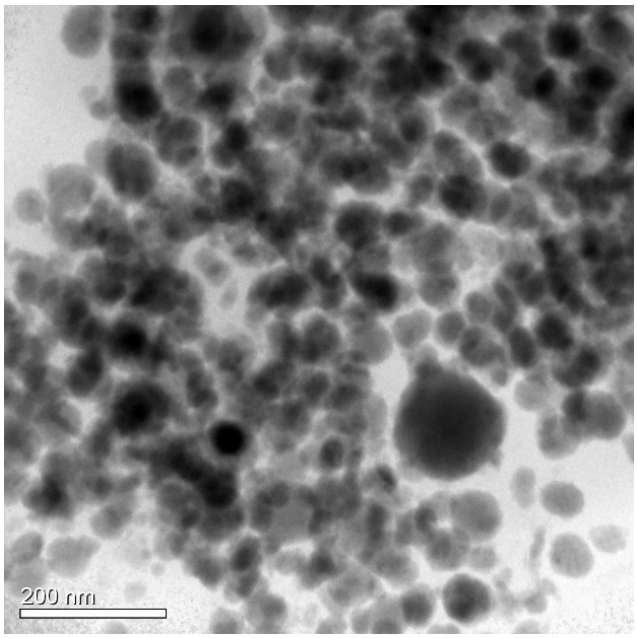


**Figure 6.9.** TEM image of GaN nanoparticles from pyrolysis of $[Ga(NMe_2)_3]_2$ at 315 °C using TOP.

# 6.6 Experimental

All preparations were carried out under anaerobic conditions using either glove box or Schlenk line techniques for sample loading and handling. Hexane, diethylether, TOA and TOP were freshly distilled from sodium/benzophenone prior to use and hexadecylamine (HDA) from BaO. $GaCl_3$ (99.999 %) was purchased from Aldrich and used as supplied. Ammonia (Air Products) was distilled from a sodium/ammonia solution before use. $LiNMe_2$ and $LiNEt_2$ were synthesised by reacting 1.6 M $^n$BuLi in hexane (Aldrich) with $HNMe_2$ and $HNEt_2$ respectively, filtering, and drying the product under vacuum.

Powder X-ray diffraction (PXD) measurements were performed on a Siemens D5000 and on a C2 using Cu$K_{\alpha_1}$ ($\lambda$ = 1.5406 Å) radiation. The phases present were identified by comparison with the JCPDS database[34]. Crystallite sizes were obtained using the Scherrer formula. Transmission electron microscopy (TEM) was carried out with a Hitachi 7000 (75 kV) instrument in a Jeol JEM3010 microscope. Samples were prepared by ultrasound dispersal in toluene, followed by deposition on carbon-coated Cu grids. NMR spectrums were collected using a Bruker AV 300. Samples (~10 mg) were dissolved in deuterated benzene.

# 6.7 Conclusions

In this work, the preparation of nanocrystals GaN was investigated using colloidal chemistry synthesis. Initial results reported by others were developed and studied in this work. $[Ga(NEt_2)_3]_2$ was synthesized, obtaining a brown, oily, impure product. The precursor contained impurities whose presence was visible by the NMR spectrum. The purification by crystallization and sublimation were not successful. Due to these difficulties, the preparation of GaN was most studied using $[Ga(NMe_2)_3]_2$.

$[Ga(NMe_2)_3]_2$ was synthesized by the reaction of $GaCl_3$ with $LiNMe_2$ in hexane obtaining colourless crystals. The characterization by $^1$H-NMR confirmed the dimeric structure of the precursor.

Pyrolytic preparation of GaN from $[Ga(NMe_2)_3]_2$ was investigated using different stabilizing agents such as : HDA/TOA, TOA, TOP. Thermal decomposition of $[Ga(NMe_2)_3]_2$ in HDA/TOA at 330 ºC yielded zinc-blende type GaN.

Various reaction conditions were investigated in the thermal decomposition of $[Ga(NMe_2)_3]_2$ in HDA/TOA. Small particle size (less than 5 nm) were revealed from TEM images with evidence of HDA in the final product. The products collected were sticky. It was attributed to the presence of HDA in the system. HDA elimination was difficult in the common solvents used as toluene or hexane. The products prepared were black in colour indicating carbon content from decomposition of HDA/TOA. Its present did mean that it was incorporated into the particles but it could be related to the long aliphatic chains from the capping ligands. Considering that the maximum reaction temperature with the equipment used was 330 ºC, the crystallization of the final product was good. Moreover a nucleation step at higher temperature could make the difference.

A mixture of wurtzute and zinc blende type GaN was obtained with TOA at 315 ºC. TEM images showed spherical particles with diameter of about 30-50 nm larger than those obtained using HDA/TOA. The particle size was larger than that calculated from the X-ray diffraction pattern of GaN. This was due to the aggregation of small crystallite.
Pyrolysis of $[Ga(NMe_2)_3]_2$ in trioctylphosphine gave a broad distribution of spherical aggregated particles of about 50 nm. The sample was not isolated and TEM grids was made from the solution.

# 6.8 References


1. C. B. Murray, D. J. Norris and M. G. Bawendi, *J. Am. Chem. Soc.*, 1993, **115**, 8706.
2. O. I. Micić, C. J. Curtis, K. M. Jones, J. R. Sprague and A. J. Nozik, *J. Phys. Chem.*, 1994, **98**, 4966.
3. A. Guzelian, J. Katari, A. Kadavanich, U. Banin, K. Hamad, E. Juban, A. Alivisatos, R. Wolters, C. Arnold and J. Heath, *J. Phys. Chem.*, 1996, **100**, 7212.
4. O. I. Micić, H. Cheong, H. Fu, A. Zunger, J. Sprague, A. Mascarenhas and A. Nozik, *J. Phys. Chem. B*, 1997, **101**, 4904.
5. O. I. Micić, K. M. Jones, A. Cahill and A. J. Nozik, *J. Phys. Chem. B*, 1998, **102**, 9791.
6. O. I. Micić, B. B. Smith and A. J. Nozik, *J. Phys. Chem. B*, 2000, **104**, 12149.
7. O. I. Micić, S. Ahrenkiel and A. J. Nozik, *Appl. Phys. Lett.*, 2001, **78**, 4022.
8. O. I. Micić, J. Sprague, C. Curtis, K. Jones, J. Machol, A. Nozik, H. Giessen, B. Fluegel, G. Mohs and N. Peyghambarian, *J. Phys. Chem.*, 1995, **99**, 7754.
9. A. Guzelian, U. Banin, A. Kadavanich, X. Peng and A. Alivisatos, *Appl. Phys. Lett.*, 1996, **69**, 1432.
10. U. Banin, C. Lee, A. Guzelian, A. Kadavanich, A. Alivisatos, W. Jaskolski, G. Bryant, A. L. Efros and M. Rosen, *J. Chem. Phys.*, 1998, **109**, 2306.
11. E. K. Byrne, L. Pankanyi and K. H. Theopold, *Science*, 1998, **241**, 332.
12. M. Olshavsky, A. Goldstein and A. Alivisatos, *J. Am. Chem. Soc.*, 1990, **112**, 9438.
13. H. Uchida, C. J. Curtis and A. J. Nozik, *J. Phys. Chem.*, 1991, **95**, 5382.
14. H. Uchida, C. J. Curtis, P. V. Kamat, K. M. Jones and A. J. Nozik, *J. Phys Chem.*, 1992, **96**, 1156.
15. K. Brunner, U. Bockelmann, G. Abstreiter, M. Walther, G. Böhm, G. Tränkle and G. Weimann, *Phys. Rev. Lett.*, 1992, **69**, 3216.
16. P. C. Sercel, W. A. Saunders, H. A. Atwater, K. J. Vahala and R. C. Flagan, *Appl. Phys. Lett.*, 2009, **61**, 696.
17. Y. W. Cao and U. Banin, *Angew. Chem. Intern. Ed.*, 1999, **38**, 3692.
18. Y. W. Cao and U. Banin, *J. Am. Chem. Soc.*, 2000, **122**, 9692.
19. H. P. Maruska and J. J. Tietjen, *Appl. Phys. Lett.*, 2009, **15**, 327.
20. S. Strite and H. Morkoç, *J. Vac. Sci. Technol. B*, 1992, **10**, 1237.
21. S. Strite, M. E. Lin and H. Morkoç, *Thin Solid Films*, 1993, **231**, 197.
22. J. I. Pankove, *GaN and Related Materials (Gordon and Breach, Amsterdam, The Netherland)*, 1997, **2**.

23. C. H. Qiu, W. Melton, M. W. Leksono, J. I. Pankove, D. P. Keller and S. P. DenBaars, 1996, **69**, 1282.
24. H. Monkoc, S. Strilé, G. B. Gao, M. E. Lin, B. Sverdlov and M. Burns, *J. Appl. Phys.*, 1994, **76**, 1363.
25. J. F. Janik and R. L. Wells, *Chem. Mater.*, 1996, **8**, 2708.
26. J. L. Coffer, M. A. Johnson, L. Zhang, R. L. Wells and J. F. Janik, *Chem. Mater.*, 1997, **9**, 2671.
27. J.-W. Hwang, J. P. Campbell, J. Kozubowski, S. A. Hanson, J. F. Evans and W. L. Gladfelter, *Chem. Mater.*, 1995, **7**, 517.
28. K. E. Gonsalves, S. P. Rangarajan, G. Carlson, J. Kumar, K. Yang, M. Benaissa and M. Jose-Yacaman, *Appl. Phys. Lett.*, 2009, **71**, 2175.
29. M. Benaissa, K. E. Gonsalves and S. P. Rangarajan, *Appl. Phys. Lett.*, 1997, **71**, 3685.
30. O. I. Mićić, S. P. Ahrenkiel, D. Bertram and A. J. Nozik, *Appl. Phys. Lett.*, 1999, **75**, 478.
31. G. Pan, M. E. Kordesch and P. G. Van Patten, *Chem. Mater.*, 2006, **18**, 3915.
32. S. Koyama, Y. Sugahara and K. Kuroda, *Mat. Res. Soc. Symp. Proc.*, 1997, **468**, 93.
33. H. Noth and P. Konrad, *Z. Naturf.*, 1975, **30b**, 681.
34. *PCPDFWIN, version 2.4; Powder Diffraction File, International Center for Diffraction Data: Swarthmore, PA (U.S.A.)*, 2003.

# 7. Conclusions

The nanocrystalline nitride materials discussed in this thesis were largely prepared using solvothermal reactions. This method offers an effective alternative route to these materials in small crystallites forms. The type of reagent previously adopted in solid state metathesis reactions may be used and allow the formation of phases which are not achieved by metathesis reactions (e.g. metastable GaN). Moreover thermally unstable nitrides such as those of group 6 can be synthesised. The reactions under solvothermal conditions are highly exothermic but much of the heat generated during the synthesis is absorbed by the solvent. These relatively gentle conditions usually lead to nitrides with small particle sizes though aggregation of these small crystallites is often observed. The isolation of a phase usually made only at high pressure (e.g. rocksalt type GaN)[1] under solvothermal conditions, shows further potential of the method. Use of small amount of capping agent may improve the isolation of these small particles.
This study has enhanced the understanding of nanocrystalline nitride materials in many respects:

- Low reaction temperatures (~ 250 ºC) employed in the reaction of $GaCl_3$ with $LiNH_2$ yielded zinc blend (cubic) type GaN whereas temperatures between 300-450 ºC led to the formation of a mixture of wurtzite (hexagonal) and zinc blende (cubic) GaN. This indicated that the cubic phase is thermodynamically stable at lower temperatures.

- The particle aggregation was also less in GaN samples prepared at 250 ºC. Addition of HDA or CTAB was investigated to reduce the aggregation and to control the particle size. When HDA was used the crystallinity of the gallium nitride improved with additions of small quantities, and smaller crystallites were obtained. This is surprising and it is believed that HDA can react to some extent with $GaCl_3$ prior to heating, before the reaction with $LiNH_2$ starts as the solution is heated. The mechanism of condensation of metal primary amide invoked in chapter 3 was also found in the sol-gel preparation of TiN[1,2]. IR and TGA analysis confirmed the presence of HDA in the final product. CTAB is a cationic surfactant which cannot react with $GaCl_3$, but similar results to HDA were observed using CTAB.

- The reactions of $InCl_3$ with $LiNH_2$ yielded crystalline wurtzite type InN with In metal contamination even at low temperature (200 ºC). In metal content was reduced when

$InCl_3$ was reacted with a small excess of $LiNH_2$ (20 %), though a larger excess of $LiNH_2$ did not result in further reductions in In content. The material as-prepared resembled zinc blende-type InN. When $InI_3$ was used as indium source wurtzite type InN was formed and indium content was reduced but not completely eliminated.

- Group 5 and 6 nitrides (VN, NbN, $Ta_3N_5$, CrN, $Mo_2N$ and WN), were obtained from the reactions of $VCl_3$, $NbCl_5$, $TaCl_5$, $CrCl_3$, $MoCl_5$ and $WCl_4$ with $LiNH_2$ or $NH_3$ at temperature up to 550 ºC.

- Nanocrystalline VN and CrN were formed at relatively low temperatures (250-300 ºC) whereas higher temperatures (500-550 ºC) were required to produce the crystalline nitrides 4d or 5d metals. High reaction temperature favoured benzene decomposition and some carbon was usually found in the nitride prepared. Carbon content was found generally to be higher when ammonia was the nitrogen source. This may suggest that ammonia catalyzed benzene decomposition. For example, carbon content in $Ta_3N_5$ prepared with $NH_3$ at 550 ºC was ~16 % compared to 1.6 % when $LiNH_2$ was the nitrogen source. Highest carbon content was found in NbN prepared at 550 ºC (~27 %) and the lowest in VN (7.5 %) when ammonia was the nitrogen source. These variations by metal type suggest some catalytic effect of the metal centres. This consideration is supported by a lack of carbon found in the same autoclave when benzene was heated at 550 ºC with no ammonia or metal salts. Nitrogen content also varied depending from the nitrogen source. Group 5 nitrides prepared in $NH_3$ revealed lower nitrogen content compared with $LiNH_2$, presumably because some of the observed carbon is incorporated into lattice sites that would otherwise be occupied by nitrogen.

- Most of the samples showed partially agglomerated, isotropic crystallites. In some cases these crystallites were elonged and in two cases this resulted in a more significant change of morphology. $Ta_3N_5$ sample prepared at 550 ºC using $NH_3$ as the nitrogen consisted of single crystalline nanorods (~5 x 100 nm). A random distribution of rods or tubes was formed in molybdenum nitrides made using $LiNH_2$ at 550 ºC. Tubes of various lengths and diameter were also observed in $Mo_2N$ samples prepared in $NH_3$ at 550 ºC.

- Colloidal preparation of GaN nanocrystals was investigated throughout pyrolysis of $[Ga(NMe_2)_3]_2$ in hot coordinating solvents such as HDA-TOA, TOA or TOP. Pyrolysis of $[Ga(NMe_2)_3]_2$ in HDA/TOA at 330 ºC yielded zinc-blende type GaN.

Variations in precursor and agent capping concentration, reactions temperature and time were performed. While the addition of HDA to the reactions between $GaCl_3$ and $LiNH_2$ resulted in an improved crystallinity, here its presence seemed reduce the crystallinity of the materials. However the excess of HDA was difficult to remove from the samples. This may suggest that HDA was strongly bound to the small particles generated during pyrolysis and this did not allow the isolation of the particles due to their low mass and very high solubility in the HDA.

- The decomoposition of $[Ga(NMe_2)_3]_2$ in TOA (used only as coordinating solvent) indicated the formation of a mixture of wurtzite and zinc blend type GaN. Aggregation was observed in various areas of the samples.

- Better crystallization in these systems could be achieved using a nucleation step at higher temperature than those used in this work. Limitations in the experimental setup allowed only maximum temperature of 330 ºC.

# 7.1 References

1. B. M. Gray, S. Hassan, A. L. Hector, A. Kalaji and B. Mazumder, *Chem. Mater.*, 2009, **21**, 4210.
2. A. W. Jackson and A. L. Hector, *J. Chem. Mater.*, 2007, **17**, 1016.